# INFORMATION TO USERS

This manuscript has been reproduced from the microfilm master. UMI films the text directly from the original or copy submitted. Thus, some thesis and dissertation copies are in typewriter face, while others may be from any type of computer printer.

**The quality of this reproduction is dependent upon the quality of the copy submitted.** Broken or indistinct print, colored or poor quality illustrations and photographs, print bleedthrough, substandard margins, and improper alignment can adversely affect reproduction.

In the unlikely event that the author did not send UMI a complete manuscript and there are missing pages, these will be noted. Also, if unauthorized copyright material had to be removed, a note will indicate the deletion.

Oversize materials (e.g., maps, drawings, charts) are reproduced by sectioning the original, beginning at the upper left-hand corner and continuing from left to right in equal sections with small overlaps. Each original is also photographed in one exposure and is included in reduced form at the back of the book.

Photographs included in the original manuscript have been reproduced xerographically in this copy. Higher quality 6" x 9" black and white photographic prints are available for any photographs or illustrations appearing in this copy for an additional charge. Contact UMI directly to order.

**UMI**

A Bell & Howell Information Company
300 North Zeeb Road, Ann Arbor MI 48106-1346 USA
313/761-4700 800/521-0600

# Modeling of Fine Geometric Details and Singular Field Regions in TLM

by

**Giampaolo Tardioli**

"Laurea" degree, University of Ancona, Italy, 1993

*A Dissertation Submitted in Partial Fulfillment of the Requirements for the Degree of*

**Doctor of Philosophy**

*in the Department of Electrical & Computer Engineering*

We accept this thesis as conforming to the required standard

---

Dr. W. J. R. Hoefer, Supervisor
Professor, Department of Electrical and Computer Engineering

---

Dr. J. Bornemann, Departmental Member
Professor, Department of Electrical and Computer Engineering

---

Dr. R. Vahldieck, Departmental Member
Professor, Department of Electrical and Computer Engineering

---

Dr. R. N. Horspool, Outside Member
Professor, Department of Computer Science

---

Dr. Zhizhang Chen, External Examiner
Professor, Dalhousie University, Halifax, Nova Scotia Canada

Supervisor: Dr. W. J. R. Hoefer

# ABSTRACT

Numerical modeling of electromagnetic fields is becoming an important topic in such diverse areas as microwave and RF engineering, antenna design, bio-electromagnetics, and electromagnetic compatibility and interference (EMC/EMI). Among several techniques, time-domain schemes are of particular interest, due to their high flexibility and ease of implementation.

This thesis is focused on the Transmission Line Matrix (TLM) method, based on a space and time discrete formulation of Maxwell's equations. The objective of this thesis is to develop, implement and test a number of techniques aimed to the enhancement of the accuracy of the method without increasing the computational load.

The link between the electromagnetic theory and the TLM updating equations is first investigated, creating a solid background for the implementation of hybrid schemes characterized by better accuracy. The problem of coarseness error is in particular addressed. Two methods are proposed and analyzed. In the first approach the knowledge of the relationship between field equations and TLM equations is exploited to incorporate the static field behavior in the vicinity of singularities into the three-dimensional TLM mesh. Secondly, the field distribution around a corner is represented in terms of an equivalent circuit derived from a quasi-static approximation of the Green's functions for an infinite conductive wedge.

As a result, relatively coarse TLM meshes, in combination with hybrid schemes, can be used to obtain highly accurate results, within the dispersion error margin, across a wide frequency range.

By taking advantage of these techniques it is possible to incorporate more information of the structure under study into the TLM solution, thus creating an accurate and efficient CAD tool.

Examiners:

Dr. W. J. R. Hoefer, Supervisor
Professor, Department of Electrical and Computer Engineering

Dr. J. Bornemann, Departmental Member
Professor, Department of Electrical and Computer Engineering

Dr. R. Vahldieck, Departmental Member
Professor, Department of Electrical and Computer Engineering

Dr. R. N. Horspool, Outside Member
Professor, Department of Computer Science

Dr. Zhizhang Chen,, External Examiner
Professor, Dalhousie University, Halifax, Nova Scotia Canada

# Table of Contents

**Table of Contents** iv

**List of Tables** vii

**List of Figures** viii

**Acknowledgments** xi

**Dedication** xii

**List of symbols** xiii

**1 Introduction** 1

1.1 Motivations . . . . . 1
1.2 Accuracy of Space Discrete Methods . . . . . 4
1.3 Previous Work . . . . . 6
1.4 Original Contributions . . . . . 7
1.5 Overview of the Present Thesis . . . . . 9

**2 The Transmission Line Matrix Method** 10

2.1 Introduction . . . . . 10
2.2 The Two-Dimensional TLM Scheme . . . . . 13
2.3 The Three-Dimensional Symmetrical Condensed Node (SCN) TLM Scheme . . 16
2.4 Sources of Errors in TLM. . . . . 19

**3 Derivation of the SCN Scheme from Maxwell's Integral Equations** 23

3.1 Introduction . . . . . 23
3.2 Conditions imposed by Faraday's and Ampere's laws. . . . . 24
3.2.1 Faraday's law applied to the surface *Sxy*. . . . . 27

3.2.2 Ampere's law applied to the surface *Sxy*. . . . . 29
3.2.3 Complete set of conditions imposed by Maxwell's equations . . 31
3.2.4 Derivation of the scattering matrix . . . . . 32
3.3 Conclusion . . . . . 37

**4 Static Field Correction** **39**

4.1 Introduction . . . . . 39
4.2 Sharp corners and singular fields . . . . . 41
4.2.1 Static Expansion . . . . . 42
4.3 TLM representation of singular field regions . . . . . 43
4.4 TLM Corner Node . . . . . 45
4.4.1 TM-Polarization . . . . . 46
4.4.2 TE-Polarization . . . . . 50
4.5 Results . . . . . 52
4.6 Conclusion . . . . . 57

**5 Equivalent Circuit Derivation from the Green's Function of a Metallic Wedge** **58**

5.1 Introduction . . . . . 58
5.2 Theoretical Background . . . . . 60
5.3 Application to the TLM mesh . . . . . 63
5.3.1 Knife Edge . . . . . 63
5.3.2 Ninety-degree wedge . . . . . 67
5.3.3 Circuit topology . . . . . 69
5.4 Discretization process . . . . . 73
5.5 Generalization to knife edge septa of arbitrary length . . . . . 76
5.6 Numerical results . . . . . 79
5.6.1 Knife edge corner. . . . . 79
5.6.2 Ninety-degree corner . . . . . 83
5.6.3 Infinitely thin septa of arbitrary length . . . . . 85
5.7 Conclusions . . . . . 88

**6 Discussion and Conclusion** **89**

6.1 Need for Electromagnetic Modeling. . . . . 89
6.2 Future Work . . . . . 91

**7 Appendix A** **93**

7.1 Impedance elements: pointform evaluation . . . . . 93

**8 Appendix B** **97**

8.1 Knife edge case: linear integration . . . . . 97
8.2 Knife edge case: superficial integration . . . . . 98

**9 Appendix C** **99**

9.1 Ninety-degree wedge: superficial integration . . . . . 99

**Bibliography** **101**

# List of Tables

Table 4.1. Rectangular cavity with an asymmetric inductive iris. Resonant frequencies (GHz) 54

Table 4.2. Parallel plate waveguide with capacitive iris. Resonant frequencies (GHz) 56

# List of Figures


| | | |
|---|---|---|
| Figure 2.1 | a) Circuit topology of the 2D TLM shunt node. b) Equivalent lumped element model. | 13 |
| Figure 2.2 | Symmetrical Condensed Node (SCN) topology. | 17 |
| Figure 3.1 | Cubic TLM cell: (a) Field components tangent to the six faces of the cube, at different time-steps. (b) The three integration surfaces where the integral form of Maxwell's equations is evaluated | 25 |
| Figure 3.2 | Field at the node center as average of the surrounding fields | 26 |
| Figure 3.3 | Surface of integration $S_{xy}$ for Faraday's law | 27 |
| Figure 3.4 | Surface of integration $S_{xy}$ for Ampere's law | 29 |
| Figure 3.5 | Wave propagating along +x, (z-polarized). TLM associated voltage pulses: | 33 |
| Figure 3.6 | Six plane waves propagating through the node in three different directions. | 34 |
| Figure 4.1 | Perfectly sharp metallic edge | 41 |
| Figure 4.2 | Geometry of a knife metallic edge | 43 |
| Figure 4.3 | Three-dimensional plot of: (a) function, with singularity in the origin. (b) equivalent representation with the TLM modeling. | 44 |
| Figure 4.4 | Resonant frequency of a finned cavity, and comparison between dispersion and coarseness error. | 45 |
| Figure 4.5 | Knife edge in a TLM mesh; the edge is placed on TLM nodes | 46 |
| Figure 4.6 | Location of the electric field at surrounding nodes used for the evaluation of the expansion coefficients | 49 |
| Figure 4.7 | Location of the magnetic field at surrounding modes used for the evaluation of the expansion coefficients | 51 |

| | | |
|---|---|---|
| Figure 4.8 | Rectangular cavity with an asymmetric inductive iris | 52 |
| Figure 4.9 | Time domain waveform ($\Delta l$ = 1 mm) | 53 |
| Figure 4.10 | First resonant frequency of the finned cavity. Different discretizations, with and without corner correction. | 53 |
| Figure 4.11 | Resonant cavity in parallel plate waveguide with capacitive coupling | 54 |
| Figure 4.12 | First resonant frequency of the parallel plate waveguide cavity, loaded with a capacitive iris. Different discretizations, with and without corner correction. | 55 |
| Figure 5.1 | Infinitive conducting wedge geometry. | 60 |
| Figure 5.2 | Wedge position in the TLM mesh. Knife edge case. | 63 |
| Figure 5.3 | Domains of integration for $Z_{ij}$ | 66 |
| Figure 5.4 | Wedge position in the TLM mesh. 90 case. | 67 |
| Figure 5.5 | Domain of integration for the determination of Zij, 90 corner | 69 |
| Figure 5.6 | Topologies for each of the elementary admittance matrices | 71 |
| Figure 5.7 | Shunt connection of the four building blocks. Only the connection for the port three is shown. | 72 |
| Figure 5.8 | Equivalent corner-node circuit for the knife edge case | 73 |
| Figure 5.9 | Embedding of the equivalent corner-node circuit in the TLM mesh | 74 |
| Figure 5.10 | Corner node modeled with an impedance matrix. (a) Knife edge case, three-port circuit. (b) ninety-degree wedge, two-port circuit 75 | |
| Figure 5.11 | Position of the knife edge septum of arbitrary length in the TLM mesh and domain of integration for the evaluation of Zij | 77 |
| Figure 5.12 | Septum-coupled cavity | 79 |
| Figure 5.13 | Comparison between the first resonant frequencies obtained with the standard TLMand different corner corrections | 80 |
| Figure 5.14 | Inductive irises in WR(28) waveguide: a) Top view b) Front view 81 | |
| Figure 5.15 | S-parameters for the thin iris in WR(28) waveguide: a) TLM with | |

| | | |
|---|---|---|
| | corner correction, b) TLM without corner correction | 81 |
| Figure 5.16 | Top view of the iris coupled bandpass filter in WR(28) waveguide | 82 |
| Figure 5.17 | Iris coupled bandpass filter in WR(28) waveguide: TLM with corner correction | 82 |
| Figure 5.18 | Iris coupled bandpass filter in WR(28) waveguide: TLM without corner correction | 83 |
| Figure 5.19 | Thick inductive irises in WR(28) waveguide: a) Top view b) Front view | 84 |
| Figure 5.20 | S-parameters for the thick iris in WR(28) waveguide: TLM With corner correction | 84 |
| Figure 5.21 | S-parameters for the thick iris in WR(28) waveguide: TLM without corner correction, | 85 |
| Figure 5.22 | Top view of the thin inductive iris in WR(28) waveguide with septa of arbitrary length l | 86 |
| Figure 5.23 | S-parameters of a thin inductive iris in WR(28) waveguide for different lengths of the septa. Discretization: Dl=a/12. w=+ 0.19Dl, + 0.23Dl | 87 |
| Figure 5.24 | S-parameters of a thin inductive iris in WR(28) waveguide for different lengths of the septa. Discretization: Dl=a/12. w=+ 0.19Dl, + 0.23Dl | 87 |
| Figure 7.1 | Wedge position in the TLM mesh. Knife edge case. | 93 |

# Acknowledgments

I would like to thank the many persons who helped me in this most interesting experience.

I wish to express my gratitude to my supervisor, Prof. Hoefer. Without his help and advice none of this would have been possible. He has been a constant guide and a supportive presence throughout all these years. Working with him has been an exciting learning experience.

I wish to thank my former supervisor, Prof. Rozzi, for introducing me to the fascinating electromagnetic world.

Thanks to the many, past and present, members of the NSERC/MPR Teltech Research Group: Lucia Cascio, Dr. Eswarappa Channabasappa, Sherri Cole, Leonardo DeMenezes, Cristof Fuchs, Masafumi Fujii, Dr. Jonathan Herring, Christa Rossner, Poman So, and Qi Zhang. I thank you all for the useful discussions and helpful suggestions.

The financial support provided by Natural Sciences and Engineering Research Council of Canada, the Science Council of British Columbia, MPR Teltech Inc. of Burnaby, B.C., and the University of Victoria, is gratefully acknowledged.

My last acknowledgments are to my parents and my aunt Leandra, for loving me so much, and to my wife Lucia, for being always there, together.

# Dedication

*To my wife*

# List of symbols

The following symbols are used throughout this thesis:

| | |
|---|---|
| c | speed of light |
| f | frequency |
| i | index in the x-direction ($x=i\,\Delta x$) |
| j | index in the y-direction ($y=j\,\Delta y$) |
| j | $\sqrt{-1}$ |
| k | timestep (iteration) number |
| p | mode order |
| **r** | position vector |
| t | time |
| v | phase velocity |
| **B** | magnetic flux density |
| C | capacitance |
| **D** | electric displacement |
| **E** | electric field |
| G | conductance |
| G | Green's function |
| **H** | magnetic field |
| I | current |
| [I] | identity matrix |
| L | inductance |
| [M] | mapping matrix |
| $N_x$ | number of cells in the x-direction |
| $N_y$ | number of cells in the y-direction |
| $N_z$ | number of cells in the y-direction |
| P | mode considered |
| [P] | connection matrix |
| R | resistance |
| [S] | scattering matrix |
| V | voltage |
| Y | admittance |
| $Y_o$ | characteristic admittance |
| Z | impedance |
| $Z_o$ | characteristic impedance |
| $Z_l$ | link-line impedance |
| $\beta$ | propagation constant |
| $\varepsilon$ | absolute permittivity |
| $\varepsilon_o$ | permittivity of free space |
| $\varepsilon_r$ | relative permittivity |

| | |
|---|---|
| $\lambda$ | wavelength |
| $\lambda_o$ | wavelength in free space |
| $\mu$ | absolute permeability |
| $\mu_o$ | permeability of free space |
| $\mu_r$ | relative permeability |
| $\omega$ | angular frequency |
| $\Gamma_l$ | link-line reflection coefficient |
| $\Gamma_w$ | wave reflection coefficient |
| $\Delta f$ | frequency step |
| $\Delta l$ | space discretization step |
| $\Delta t$ | temporal discretization step |
| $\Delta x$ | node spacing in x-direction |
| $\Delta y$ | node spacing in y-direction |
| $\Delta z$ | node spacing in z-direction |
| $L_{ij}$ | Elements of an inductance matrix |
| $Z_{ij}$ | Elements of an impedance matrix |
| $\rho,\phi$ | field point in a cylindrical coordinate system |
| $\rho',\phi'$ | source point in a cylindrical coordinate system |
| $H_\nu^{(2)}$ | Hankel function order $\nu$ |
| $J_\nu$ | Bessel function order $\nu$ |
| [A] | matrix composed of elements $[a_{ij}]$ |
| [A] | array composed of elements $[a_i]$ |
| $[A]^T$ | transposed array or matrix |

**Prefixes**

A subscript prefix is used to denote the timestep (iteration) number.

**Suffixes**

The following superscript suffixes are used:

| | |
|---|---|
| i | pulse incident upon a node |
| r | pulse reflected from a node |
| s | stub parameter (as distinct from a link-line parameter) |

The following subscript suffixes are used:

| | |
|---|---|
| 1..18 | pulse on link lines 1 to 18 |
| *inj* | pulse polarized in the *j* direction, negative direction *i*. |

*ipj* pulse polarized in the *j* direction, positive direction *i*.

l link-line parameters

n network parameters

**Common abbreviations**

TLM Transmission Line Matrix

FEM Finite Element Method

MoM Method of Moments

MM Mode Matching Method

FDFD Finite Differences in the Frequency Domain

FDTD Finite Differences in the Time Domain

MRTD Multi Resolution Time Domain

ABC Absorbing Boundary Condition

TE Transverse Electric

TM Transverse Magnetic

2D Two-dimensional

3D Three-dimensional

# Chapter 1

# Introduction

## 1.1 Motivations

Any related problem involving electromagnetics has its ultimate solution in the application of Maxwell's equations. Unfortunately these equations can be solved analytically only for very few special cases. The problems are usually so complex that strong approximations must be introduced, and simplified models must be developed. Very often a combination of analytical and numerical techniques must be applied to approximate a solution with the desired accuracy. Over the years, electrical engineers have developed powerful models that allow solutions of electromagnetic problems without solving Maxwell's equations directly. A general classification can be based on the frequency spectrum of the problem considered. In particular three ranges for the wavelength $\lambda$, and the approximate dimension $l$ of the structure under investigation can be distinguished.

- $\lambda >> l$

  Problems in this frequency range are solved by using *circuit theory*. Propagation effects are neglected and substituted with lumped models. Electromagnetic fields are replaced by global parameters such as voltages and currents. [1]

- $\lambda << l$

  When the dimensions of the radiating or scattering structure are many times the wavelength, high-frequency asymptotic techniques are used. The wave nature of the signal is neglected, and simple concepts such as direct, reflected and refracted rays are used. The theory behind this approach is referred to as *geometrical optics*. More sophisticated methods, such as the *geometrical theory of diffraction* (GTD) and the *physical theory of diffraction* (PTD) can also be used to overcome some of

the limitations of geometrical optics, by introducing a diffraction mechanism.

- $\lambda \approx l$

  When the wavelength of the electromagnetic field and the dimension of the apparatus are comparable, neither the propagation effects nor the wave nature of the signal can be neglected. Global parameters, such as voltages and currents, are more difficult to define, and problems such as mode coupling, propagation of hybrid modes, non-ideal material etc. must be taken into consideration. A *full-wave* solution of the problem has to be provided. Hence, Maxwell's equations, in differential or integral form, must be approximately solved with a certain degree of accuracy at any point inside the space of interest, including material properties and surrounding boundary conditions.

Due to the increase in clock rate and integration density in modern IC technology, the latter case ($\lambda \approx l$) is becoming a common situation that design engineers must deal with. Traditional lumped circuit design methodology fails to accurately account for the complex interactions between different parts of the circuit. Problems such as dispersion, crosstalk and package effects must be taken into account, in order to predict their impact on the final configuration.

Moreover, the explosion of wireless technology and personal communication systems (PCS), is creating a large demand for transmitting channels of increasingly wider capability, thus increasing the frequency at which the radio signals are transmitted. Digital cellular phones working at 900 and 1800 MHz are already established [2], and standards for wireless data transmission operating at 2400 MHz have already been defined [3]. The foreseen convergence of audio, video and data signals in a single digital stream will further increase the demand for larger bandwidths.

For all these reasons, numerical modeling of electromagnetic fields is becoming an important topic in such diverse areas as microwave and RF engineering, antenna design, bio-electromagnetics, and electromagnetic compatibility and interference (EMC/EMI). The underlying problem in all these areas is the need to characterize, control, or eliminate the effects of electromagnetic fields.

A classification of the different numerical methods for electromagnetic modeling can be based on the type of formulation used (integral or differential), and the domain in which the procedure is applied (time or frequency).

*Integral-Differential Formulation*

In the integral formulations [4] initial and boundary conditions are embedded in the algorithm at a very early stage. Analytical pre-processing is very often required, and the resulting scheme is usually structure oriented. A change in the geometry of the problem leads to the re-formulation of the algorithm, since the new boundary conditions must be re-imposed. In differential schemes [5], on the contrary, initial and boundary conditions enter at a very late stage. Negligible analytical pre-processing is necessary, and a change in the geometry of the problem is easily implemented.

*Frequency-Time Domain*

In frequency domain methods the steady-state solution of the electromagnetic fields is determined. Linear materials, and sinusoidal excitations at a given frequency, are assumed. Time domain methods, on the contrary, provide the natural evolution of the field as it propagates in time, including transient phenomena. It is important to point out that both domains of representation contain the same information. It is in fact always possible, *in principle*, to transform a time domain response into the frequency domain or vice versa, by applying a direct or inverse Fourier transform. In reality, while the transformation from time to frequency domain is particularly straightforward, the opposite presents several pitfalls.

The main features of time domain differential methods are summarized in the following:

- Flexibility. General geometries can be simulated without any change in the algorithm. The boundary conditions become one of the input parameters.
- Capability to analyze transients.
- Capability to analyze non-linear phenomena, time varying structures. (For example the change of material property in an electromagnetic heating process).
- Ease of implementation of anisotropic material.
- Ease of parallel implementation with consequent reduction of the simulation time.
- Possibility of deriving frequency domain results over a wide frequency range with a single time domain simulation.
- Possibility of hybridization with other numerical techniques.

- Integration with SPICE type circuit solvers for the modeling of circuits containing active and non linear lumped devices.
- Reverse time simulation. Performing simulation with a negative time can be used for the image reconstruction of arbitrary shaped scatterers [6-7].

In particular, when both the capabilities of analyzing arbitrary geometries and handling non-linear effects are required, several other numerical methods are ruled out. Other methods, in fact, are either geometry specific, and therefore computationally more efficient (integral formulation), or they use the principle of superposition in their formulation, thus implying linearity (frequency domain methods).

The most widely used time domain differential techniques are the Finite Difference Time Domain Method (FDTD) [8] and the Transmission Line Matrix (TLM) method [9]. Recently, a new technique, based on the expansion of the electromagnetic fields using wavelets as basis functions, has been proposed [10-13]. Such a technique, called Multi-Resolution Time Domain (MRTD) method, is at a very early development stage, and does not represent, at the moment, a mature alternative for the two previously mentioned methods.

This thesis is focused on the Transmission Line Matrix (TLM) technique. The TLM method is based on a space and time discrete formulation of Maxwell's equations. The partial differential equations arising for field problems are solved with the aid of equivalent electrical networks, exploiting the analogy between field theory and transmission line theory. The analysis is performed in the time domain and the entire computational domain is discretized with a grid of TLM nodes. All the nodes are interconnected by virtual transmission lines. Excitations at the source nodes propagate to adjacent nodes through these transmission lines at each time step.

Like other numerical techniques, the TLM method is affected by several sources of inaccuracy. One of the disadvantages of TLM (and other space discrete methods) is the computational overhead incurred in analyzing electrically small details, in particular when highly non-uniform fields are involved. A detailed description of the method, together with different sources of error, will be given in the following chapter.

## 1.2 Accuracy of Space Discrete Methods

Space discrete methods, such as Finite Element Method (FEM), Finite Difference

Frequency Domain (FDFD), FDTD, and TLM, are currently used for solving a wide variety of field problems. The computational domain is discretized into a finite number of elementary cells where the electromagnetic field is assumed to have a simple space dependence, very often linear. This assumption fails to accurately model sharp features, where highly nonuniform fields are present. This is typically the case at corners and edges, where the electromagnetic fields are singular. This source of inaccuracy is referred to as *coarseness error.*

For FDTD and TLM, the space discrete nature of the methods leads also to the presence of other errors, such as the velocity and the discretization error. The velocity error is caused by the fact that the electromagnetic waves propagate in the discrete medium with different velocities in different directions. The discrete medium is therefore no longer isotropic. The discretization error is related to the difficulty of fitting exactly all the dimensions of the structure under investigation, because of the finite discretization step. Mesh grading and special nodes [14] can overcome this latter problem.

A comparison between velocity error and the coarseness error reveals that the latter is the dominant source of inaccuracy in most practical cases, and represents the most severe limitation to the maximum admissible cell size [15-16].

A direct solution to reduce the coarseness error is to use an extremely fine mesh, but this quickly leads to unacceptable memory and time requirements. A better approach is to use a variable [17] or multigrid mesh [18], so that a higher resolution can be obtained in that region. In this case the resources would still be larger than those of a uniform coarser mesh with a mesh parameter based on the dispersion error only.

It is known that in the vicinity of sharp edges the electromagnetic field is essentially independent of the external conditions, and it is ruled mainly by the static, singular behavior. It is therefore conceivable to create a hybrid scheme, where the field in the vicinity of edges is imposed from the *a priori* knowledge of the static solution, whereas the surrounding space and boundary conditions are modeled with the standard numerical method. In view of this approach, it is evident that a clear understanding of the relationship between field quantities and numerical method parameters is required, together with the degree of approximation involved.

The objective of this thesis is to understand and describe the link between the field equations and the TLM technique, and to increase the accuracy and efficiency of the method. This goal will be pursued by exploring novel schemes for implementing, into

the standard TLM algorithm, existing *a priori* knowledge of the electromagnetic field behavior.

## 1.3 Previous Work

The extremely large computational effort required for the analysis of electrically small details has been, since the very first stage of development, a common problem for time domain, space discrete methods. Studies on how to minimize this problem have been performed over the years, and several different approaches have been proposed.

A common technique consists in using mesh refinements in the regions of the computational domain where highly nonuniform fields are expected. Such a refinement can be achieved by means of a graded mesh, where the cell dimensions are maintained constant in each coordinate direction [19] or by means of a multigrid scheme, where a finer mesh is locally embedded in a coarser one [20]. Each of these techniques presents advantages and disadvantages, and the use of one or the other is largely left to the modeling engineer. A drawback of these methods lies in the fact that the required computing resources are still much larger than those required by a uniform coarser mesh, thus not very often providing a feasible and efficient solution.

For this reason research work has been focused recently on solutions based on *local* modifications of the time marching algorithms. This approach was first used for the modeling of boundaries which are not parallel to the coordinate axes. A vast literature is available on this subject for the FDTD method [21-24].

Static field solutions have then been used in a variety of ways in order to introduce a local modification of finite difference algorithms, (FDTD, FDFD) [25-29]. Very often the static field solution is pre-computed by using a finer discretization, or is derived from analytical formulations.

Research work related to the TLM method has also been done. In [30] extra stubs are added to the TLM node circuit topology. The values of the new added elements is empirically determined. An approach based on the local modification of the energy stored around the edge has been proposed in [31]. The link lines surrounding the corner node are directly connected, thus simulating a faster propagation of the wave in the region. Correction factors are then introduced by surrounding the corner with loaded stubs with optimized characteristics. All these techniques are not systematic and require

an optimization process to determine the values of the correcting elements.

## 1.4 Original Contributions

The following original contributions to the advancement of the TLM method are described in this thesis:

- *Novel Derivation of TLM Symmetrical Condensed Node scheme from Maxwell's integral equations.*

  The link between the electromagnetic theory and the TLM updating equations is explored. A novel derivation of the TLM SCN scheme from Maxwell's integral equations is presented. It is shown that the standard TLM scheme not only satisfies Faraday's and Ampere's laws, but also implies a linear behavior for the electromagnetic waves traveling through the TLM node. Such a derivation clarifies the relationship between electromagnetic fields and circuit parameters and provides an insight into the approximations introduced by the discrete algorithm.

- *New special SCN scattering algorithm for singular regions*

  The problem of coarseness error is then addressed. The knowledge of the relationship between field equations and TLM equations is exploited to incorporate the static field behavior in the vicinity of singularities into the three-dimensional TLM mesh. The proposed procedure is systematic and does not require optimization of the correcting elements. As a result, relatively coarse TLM meshes can be used to obtain highly accurate results, within the dispersion error margin, across a wide frequency range. The accuracy is improved without an increase in the computational effort.

- *New TLM corner node based on a quasi-static approximation of the Green's functions for an infinite conductive wedge*

  The presence of long term instabilities, arising from altering the standard TLM update equations, is investigated, and a new approach based on the derivation of an equivalent circuit is considered. With this new technique, the field distribution around a corner is represented in terms of an equivalent circuit derived from a quasi-static approximation of the Green's functions for an infinite conductive wedge. A discretization procedure for embedding the equivalent circuit in the TLM network, thus creating a hybrid scheme, is explored. The resulting hybrid algorithm is guaranteed to be unconditionally stable, since the modification of the TLM scheme is performed

on the basis of a passive linear circuit. Different types of wedge geometries are investigated. The method is then extended to knife edge septa of arbitrary length. Again this contribution leads to a pronounced improvement in accuracy when analyzing structures with sharp edges.

## 1.5 Overview of the Present Thesis

After this introduction, Chapter Two will give a brief description of the Transmission Line Matrix (TLM) method, both for the two-dimensional and three-dimensional case, with a general overview of the main sources of inaccuracy.

Chapter Three will describe a novel approach for deriving the scattering algorithm of the TLM symmetrical condensed node directly from Maxwell's equations. Maxwell's equations in their integral formulation will be applied, together with extra conditions based on physical considerations.

Chapter Four will derive a new TLM scattering algorithm for edge nodes based on a static approximation of the electromagnetic field in the proximity of singular points. The standard algorithm is only locally modified, thus maintaining the same computational load of a coarse mesh, without altering the algorithm throughout the entire computational domain.

Chapter Five will explore a new method to model the singular field regions based on a quasi-static approximation of the Green's function for a perfectly conducting metallic wedge. An equivalent circuit is derived and embedded in the TLM mesh via a discretization procedure. The stability of the hybrid scheme is guaranteed by circuit theory.

Finally, in Chapter Six, the conclusions of this thesis are presented, and future research directions opened up by this work are delineated.

# Chapter 2

# The Transmission Line Matrix Method

## 2.1 Introduction

The Transmission line matrix method is a space and time discrete technique. It belongs to the category of time domain, differential numerical techniques. The method is based upon transmission line theory. In the same manner as a uniform electromagnetic plane wave can be associated with a single transmission line having a specific characteristic impedance and phase velocity, more complex electromagnetic phenomena can be modeled with a mesh of transmission lines. Such a network represents the equivalent circuit of the structure under investigation, and classic circuit theory can be used for its analysis.

The points at which these transmission lines are interconnected are referred to as TLM nodes. The finite space that contains the node and short sections of transmission lines is called a cell. At each timestep the voltage pulses incident upon the node are scattered to produce a new set of pulses, referred to as reflected or scattered pulses. The values of the scattered voltage pulses are determined as linear combinations of the incident pulses, by means of a so-called scattering matrix [S]. In matrix notation, the entire process is described as:

$$_{k}[V^{r}] = [S]_{k}[V^{i}] \tag{2.1}$$

where the array of incident voltages $[V^{i}]$ is scattered at the time step k according to the scattering matrix [S]. We assume the entire process to be instantaneous.

The reflected pulses propagate to the neighboring nodes and become incident on them at the next time step. In matrix notation the propagation algorithm can be written as:

$$_{k+1}[V^i] = [P]_k[V^r] \tag{2.2}$$

where [P] represents the connection matrix. The combined effect of scattering and propagation, repeated at each time-step, creates the propagation of the pulses through the network. Voltage pulses travel through the mesh just like electromagnetic fields travel through space.

Depending on the type of circuit topology used to model the junction of the lines, several TLM nodes have been developed. For each of them a mapping between voltages and currents and the electromagnetic field components is available. Thus, by solving the TLM network, we can simulate what happens in arbitrary electromagnetic structures.

Due to the discrete nature of the method, the field values are available in a TLM simulation only at periodic time intervals $\Delta t$. The field values are only defined at specific points in space, that is at node center. If $v_l$ is the speed of propagation in the link lines, the value of $\Delta t$ becomes:

$$\Delta t_l = \frac{\Delta l}{v_l} \tag{2.3}$$

So far a relation between the propagation of electromagnetic waves in free unbound space and the propagation of voltage and current pulses in a transmission line network has been established, such a connection representing the core of the transmission line matrix technique. In order to simulate complex structures, containing materials other than free space, we need to define how to model the constitutive parameters of the media, how to insert boundary conditions and proper excitation sources.

A given value of permeability and permittivity for a defined portion of space is modeled by altering the energy content of each of the cells contained in that region. For example, when a higher value of permittivity is required, an open stub is added to each node so that, at each iteration, extra reactive energy is stored. As a result the wave propagating in that region slows down, thus simulating a medium with a higher dielectric constant. Similarly, a short-circuited stub is used for the modeling of arbitrary permeability values. More complex cases, such as lossy, anisotropic, and nonlinear media can still be handled, with the use of circuits more complex than simple stubs, where storage of several time-steps, presence of controlled sources, and presence of non linear devices might be required [32].

Boundaries are described by terminating each transmission line that intersects the boundary with appropriate loads obtained through circuit theory. For example, electric walls are described by the reflection coefficient of a transmission line terminated by a short circuit (reflection coefficient $\Gamma_l$= -1). They are usually placed half way between cells, at a distance $\Delta l/2$ from the node center, or on the nodes themselves, so that synchronism of impulses reflected at boundaries is ensured. Particular attention must be drawn to the case of the so called Absorbing Boundary Conditions (ABCs). They represent a particular class of boundaries, developed for proper termination of the computational domain. They do not correspond to any physical model, but they are necessary to ensure that the computational domain is finite. A vast literature [33-40] is available on this topic.

Sources and probes are placed in the desired positions to excite and sample the field. The time domain evolution of the field is recorded, yielding the transient response of the problem, and is processed to obtain further information (frequency domain data, scattering parameters, impedance of the structure, etc.). Since the entire process is simulated as it evolves in time, field animations can also be performed.

From the above description of the method it should be clear that the advantages of the Transmission Line Matrix technique reside in its flexibility, its capability of modeling a large class of media, and the possibility to handle complex, geometrically irregular structures.

As with other numerical techniques, the TLM method is affected by several sources of inaccuracy. Their presence must be well known to the modeling engineer in order to yield reliable and accurate results. In particular it is important to understand what is the relative weight of each of these sources of error, and how to minimize their impact on the result. The following typical sources of error affect a TLM simulation:

- The impulse response must be truncated in time.
- The propagation velocity in the TLM mesh depends on the direction of propagation and on the frequency.
- The spatial resolution is limited by the finite mesh size.

In the following sections a review of the two- and three-dimensional free space TLM schemes will be given, together with a more detailed analysis of the common sources of inaccuracy. For an extensive review of the method and its applications the reader is referred to references [41-50].

## 2.2 The Two-Dimensional TLM Scheme

Many electromagnetic problems are, due to the presence of either geometrical or electrical symmetries, two-dimensional (2D) problems. A typical example is the propagation of $TE_{n0}$ modes in homogeneous parallel and rectangular waveguides, in the presence of inductive irises, T-junctions, and bends having constant dimensions in the direction of the E-field. Furthermore, important characteristics of intrinsically three-dimensional structures can be determined with a 2D simulation. For example, the determination of the propagation constant of a inhomogeneously filled cylindrical waveguide of arbitrary cross section requires a 3D analysis, but the cutoff frequencies of all modes can be determined with a simple 2D simulation.

Considering also the useful insight into the method that can be obtained, a brief description of the 2D TLM scheme is therefore of interest.

Depending on the circuit topology that is chosen for two intersecting transmission lines, two different 2D TLM schemes can be derived: the so called TLM Shunt Node and the TLM Series Node. It will be shown later that by applying the principle of duality only one type of node, either series or shunt, is needed to model both TE and TM fields, by establishing a different analogy between circuit and field quantities. For this reason the description of just one of the two schemes is of interest. In the following an analysis of the 2D TLM Shunt node is given.

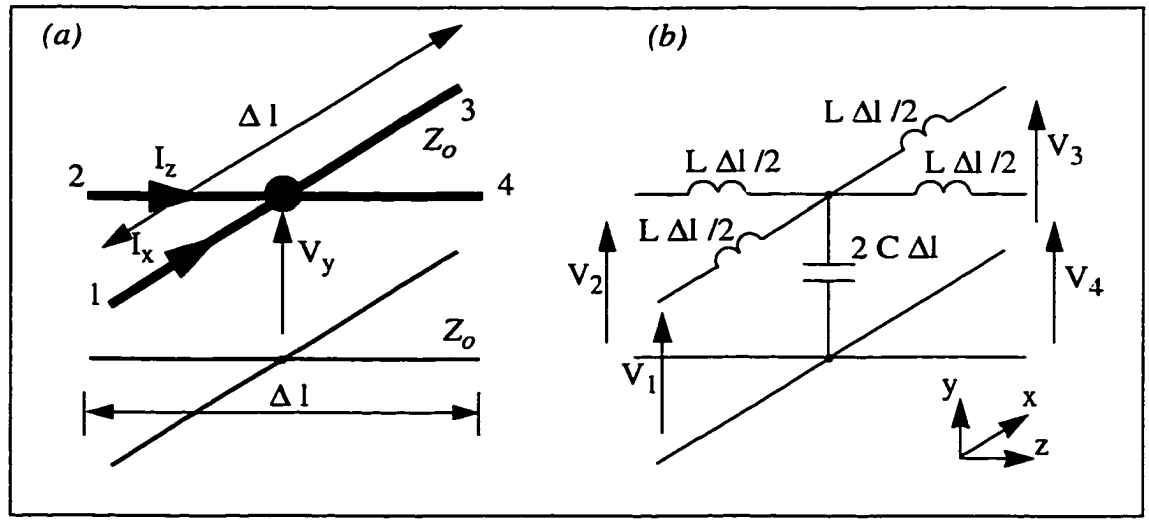


*Figure 2.1 a) Circuit topology of the 2D TLM shunt node. b) Equivalent lumped element model.*

The circuit shown in Figure 2.1 (a) represents the building block of the 2D-TLM Shunt node. Two transmission lines having the same characteristic impedance $Z_0$ intersect in a parallel connection.

Considering the node as a four-port circuit, its scattering matrix [S] can be easily derived by applying circuit theory rules. Consider an impulse traveling toward a shunt node. It will see a local reflection coefficient $\Gamma_i$ imposed by the parallel combination of the other three outgoing lines. That is:

$$\frac{V_i^r}{V_i^i} = \Gamma_i = \frac{Z_0/3 - Z_0}{Z_0/3 + Z_0} = -\frac{1}{2} \tag{2.4}$$

The transmission coefficient for each outgoing line is therefore given by:

$$T_i = 1 + \Gamma_i = \frac{1}{2} \tag{2.5}$$

The more general case of four impulses being incident on the four branches of a node can be obtained by superposition from the previous case, taking advantage of the linearity of the problem. Denoting with $v_1^i, v_2^i, v_3^i, v_4^i$ the voltage impulses incident on lines 1-4, the total voltage impulse reflected into the *n*-th line will be:

$$V_n^r = \frac{1}{2}\left(\sum_{m=1}^{4} V_m^i\right) - V_n^i \qquad n = 1, \ldots, 4 \tag{2.6}$$

In matrix notation (2.6) becomes:

$$\begin{bmatrix} V^r_1 \\ V^r_2 \\ V^r_3 \\ V^r_4 \end{bmatrix}_k = \frac{1}{2}\begin{bmatrix} -1 & 1 & 1 & 1 \\ 1 & -1 & 1 & 1 \\ 1 & 1 & -1 & 1 \\ 1 & 1 & 1 & -1 \end{bmatrix}_k \begin{bmatrix} V^i_1 \\ V^i_2 \\ V^i_3 \\ V^i_4 \end{bmatrix}_k \tag{2.7}$$

The scattering matrix is therefore:

$$[S] = \frac{1}{2}\begin{bmatrix} -1 & 1 & 1 & 1 \\ 1 & -1 & 1 & 1 \\ 1 & 1 & -1 & 1 \\ 1 & 1 & 1 & -1 \end{bmatrix} \tag{2.8}$$

The mapping between voltages and currents propagating through the mesh and the electromagnetic field quantities is established by carrying out a comparison between the differential equations governing the propagation through the mesh and Maxwell's equations. Figure 2.1(b) depicts the lumped element model of the TLM shunt node. L and C are the inductance and capacitance per unit length of an individual line. Due to the parallel connection at the node, the node capacitance is twice that of an individual line section. As long as $\Delta l$ is very small with respect to the shortest wavelength of interest, the change in the x and z directions from one node to the next can be obtained by approximating finite difference expressions with partial derivatives. In the following equation the changes in the x and z directions from one node to the next are shown, together with the two-dimensional[1] field equations in a virtual medium with constitutive parameters $\mu_n, \varepsilon_n$.

$$\begin{aligned} \frac{\partial V_y}{\partial x} &= -L\frac{\partial I_x}{\partial t} & \qquad \frac{\partial E_y}{\partial x} &= -\mu_n\frac{\partial H_z}{\partial t} \\ \frac{\partial V_y}{\partial z} &= -L\frac{\partial I_z}{\partial t} & \qquad \frac{\partial E_y}{\partial z} &= \mu_n\frac{\partial H_x}{\partial t} \\ \frac{\partial I_z}{\partial z} + \frac{\partial I_x}{\partial x} &= -2C\frac{\partial V_y}{\partial t} & \qquad -\frac{\partial H_x}{\partial z} + \frac{\partial H_z}{\partial x} &= -\varepsilon_n\frac{\partial E_y}{\partial t} \end{aligned} \tag{2.9}$$

From visual inspection it appears that the following equivalences between field and TLM mesh parameters exist:

$$E_y = V_y \qquad H_z = I_x \qquad H_x = -I_z \qquad \mu_n = L \qquad \varepsilon_n = 2C \tag{2.10}$$

It is important to notice that if we assume the velocity of propagation on each link line to be equal to the velocity of light in free space $c$, then the propagation velocity $v$ in the TLM mesh is $1/\sqrt{2}$ times the velocity of light:

$$c = \frac{1}{\sqrt{LC}} \qquad v = \frac{1}{\sqrt{\mu_n \varepsilon_n}} = \frac{1}{\sqrt{2LC}} = \frac{c}{\sqrt{2}}. \tag{2.11}$$

In fact, due to the shunt connection, the complete network of intersecting transmission lines represents a medium of relative permittivity twice that of free space.

---

1. $\partial/\partial y = 0 \qquad E_x = E_z = H_y = 0$, describing the $TE_{no}$ modes in a rectangular waveguide, z being the longitudinal direction

As anticipated, the same wave properties can be modeled by a series-connected mesh of transmission lines or, conversely, the other polarization[1] can be modeled as well by using the shunt node. According to Babinet's principle, based on the dual nature of the electric and magnetic fields, one case can be transformed into the other by simply replacing $E_y$ with $H_y$, $\varepsilon$ with $\mu$, and the impedances with the admittances. Particular attention must be paid to the implementation of material interfaces involving partial representation by dual quantities. In such a case the introduction of a corrective interface transformer might be required [48].

Linear isotropic media are implemented in the shunt node by loading the center of the node with a shunt open-ended stub. The length of the stub is $\Delta l/2$ so that the synchronism of the scattering is maintained. At low frequencies the stub adds a lumped capacitance at each node, altering the total shunt capacitance of the node, and therefore increasing the dielectric constant of the simulated medium. The resulting scattering matrix becomes a 5x5 matrix.

## 2.3 The Three-Dimensional Symmetrical Condensed Node (SCN) TLM Scheme

From the description of the two-dimensional schemes, it is intuitive that a combination of series and shunt nodes may be used to model all six electromagnetic components in three-dimensional space. Such a node, consisting of three shunt nodes in conjunction with three series nodes, is known as the expanded node [51]. The disadvantages of this structure lie in the fact that different field components and polarizations are physically separated in space and time. This causes difficulties in applying boundary conditions simply and correctly. In order to overcome this problem several node topologies have been proposed in the last years. Among them we can mention the punctual or asymmetrical condensed node [52], where the advantage of having all field components available at the same point is counterbalanced by the fact that the node structure depends upon the spatial direction.

A scheme capable of combining the best features of the previous node topologies,

---

1. $\partial/\partial y = 0 \qquad H_x = H_z = E_y = 0$, describing the $TM_{no}$ modes in a rectangular waveguide, $z$ being the longitudinal direction

without retaining any of their drawbacks, has been proposed by Johns in 1987 [45]. This node, which is referred to as symmetrical condensed node (SCN), has become the formulation of three-dimensional TLM modeling and the most widely used type of TLM scheme.

The topology of the SCN is shown in Figure 2.2. It consists of 12 ports to represent 2 polarizations in each coordinate direction. The voltage pulses corresponding to the two polarizations are carried on pairs of uncoupled transmission lines. All the transmission lines have same characteristic impedance $Z_0$.

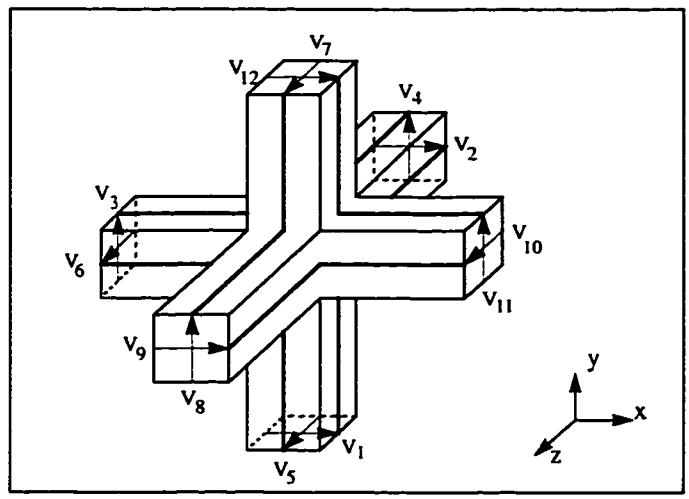


*Figure 2.2 Symmetrical Condensed Node (SCN) topology.*

The derivation of the scattering properties for the SCN using an equivalent circuit approach is not as straightforward as in the 2D case. The SCN scattering matrix is derived by first establishing which of the 12 ports are coupled, on the basis of symmetry considerations. The values of the coupling coefficients are then determined by imposing general energy and charge conservation principles [42].

The resulting scattering matrix is [45]:

$$[S] = \frac{1}{2}\begin{bmatrix} 0 & 1 & 1 & 0 & 0 & 0 & 0 & 0 & 1 & 0 & -1 & 0 \\ 1 & 0 & 0 & 0 & 0 & 1 & 0 & 0 & 0 & -1 & 0 & 1 \\ 1 & 0 & 0 & 1 & 0 & 0 & 0 & 1 & 0 & 0 & 0 & -1 \\ 0 & 0 & 1 & 0 & 1 & 0 & -1 & 0 & 0 & 0 & 1 & 0 \\ 0 & 0 & 0 & 1 & 0 & 1 & 0 & -1 & 0 & 1 & 0 & 0 \\ 0 & 1 & 0 & 0 & 1 & 0 & 1 & 0 & -1 & 0 & 0 & 0 \\ 0 & 0 & 0 & -1 & 0 & 1 & 0 & 1 & 0 & 1 & 0 & 0 \\ 0 & 0 & 1 & 0 & -1 & 0 & 1 & 0 & 0 & 0 & 1 & 0 \\ 1 & 0 & 0 & 0 & 0 & -1 & 0 & 0 & 0 & 1 & 0 & 1 \\ 0 & -1 & 0 & 0 & 1 & 0 & 1 & 0 & 1 & 0 & 0 & 0 \\ -1 & 0 & 0 & 1 & 0 & 0 & 0 & 1 & 0 & 0 & 0 & 1 \\ 0 & 1 & -1 & 0 & 0 & 0 & 0 & 0 & 1 & 0 & 1 & 0 \end{bmatrix} \tag{2.12}$$

Given the voltages on the link lines, the fields in the node center are available by applying a mapping matrix [M], as described in (2.13)

$$\Delta l \cdot \begin{bmatrix} \mathbf{E} \\ Z_0\mathbf{H} \end{bmatrix}_k = [M] \cdot_k [V^i] \tag{2.13}$$

where $Z_0$ is the free space characteristic impedance, **E** and **H** are the electric and magnetic field components, and $[V^i]$ is the array containing the twelve voltages incident upon the node. The mapping matrix [M] is therefore a 6 by 12 matrix .

$$[M] = \frac{1}{2}\begin{bmatrix} 1 & 1 & 0 & 0 & 0 & 0 & 0 & 0 & 1 & 0 & 0 & 1 \\ 0 & 0 & 1 & 1 & 0 & 0 & 0 & 1 & 0 & 0 & 1 & 0 \\ 0 & 0 & 0 & 0 & 1 & 1 & 1 & 0 & 0 & 1 & 0 & 0 \\ 0 & 0 & 0 & 1 & -1 & 0 & 1 & -1 & 0 & 0 & 0 & 0 \\ 0 & -1 & 0 & 0 & 0 & 1 & 0 & 0 & 1 & -1 & 0 & 0 \\ 1 & 0 & -1 & 0 & 0 & 0 & 0 & 0 & 0 & 0 & 1 & -1 \end{bmatrix} \tag{2.14}$$

A relationship between incident and reflected voltages and the electromagnetic fields parallel to the node boundaries is also available, as described in detail in Chapter 3.

The mapping between voltages pulses in the SCN and electromagnetic fields was until recently based upon the analogy between transmission line theory and wave propagation, and in general upon the analogy between circuit and field parameters. Direct derivations from Maxwell's equations of 3D SCN TLM through the method of moments [53], and through the finite difference approximation of Maxwell's equations [54] have been recently proposed. The following chapter of this thesis will focus on a novel approach for the derivation of the SCN scattering scheme, founded upon the discretization of the inte-

gral formulation of Maxwell's equations.

Since its first appearance, several contributions have been made to improve and extend the capabilities of the basic SCN formulation. To allow for the modeling of general lossless materials and non-uniform grading of the mesh cells, three open- and three short- circuit stubs have been added to the basic 12-port SCN [45]. In the so-called hybrid symmetrical condensed node (HSCN) only three open-circuit stubs are present, while the characteristic impedances of the lines are varied to account for mesh grading and to model the magnetic properties of the medium [55]. In a more recent development, the stubs are removed altogether and all medium properties are modeled by varying the characteristic impedances of the link lines [56-58]. Finally a general scheme, the so-called general symmetrical condensed node (GSCN) has been proposed very recently, unifying all the available condensed nodes into a single comprehensive formulation [59].

## 2.4 Sources of Errors in TLM

Like other numerical techniques, TLM is subject to several sources of error. The accuracy of each TLM simulation is affected by these errors, and each of them can be more or less predominant, depending upon several factors such as the type of structure under investigation, mesh size, frequency range of interest, etc.

An overview of the errors affecting the TLM method, together with a description of possible techniques for their reduction will be considered in the following.

- *Velocity or dispersion error*

The TLM mesh, due to its discrete nature, is inherently an anisotropic, periodic structure. The analogy between field and mesh parameters holds as long as the mesh is extremely fine compared with the wavelength. If the cell size is increased and approaches the order of a wavelength, the TLM mesh can no longer be considered as a continuum. While in free space an electromagnetic wave would travel isotropically in all directions and all frequencies, the velocity of propagation in a TLM mesh changes with the direction and the frequency of the wave. The error so introduced is referred to as velocity or dispersion error. From the analysis of the dispersion error both for the 2D and 3D TLM schemes [60-61] it appears that a discretization of twenty cells per wavelength is, in most of the cases, more than sufficient to keep the dispersion error smaller than 1%

- *Roundoff error*

Every method requiring implementation on a computer is affected by the roundoff error. This error, due to the finite precision of digital computers, is negligible compared to the other sources of error. For this reason TLM is usually implemented using single precision floating point variables.

- *Truncation error*

Each TLM simulation must be necessarily carried out for a finite number of time steps. The truncation in time of the simulation affects the accuracy of the frequency domain response of the structure. In fact, due to the finite duration of the impulse response, its Fourier transform is not a line spectrum but rather a superposition of $\frac{\sin(x)}{x}$ functions (Gibbs's phenomenon) that may interfere with each other such that their maxima are slightly shifted. This undesired effect decreases as the number of iterations increases. Most of the methods adopted for reducing the truncation error are directly borrowed from Digital Signal Processing (DSP) techniques. Among them we can mention the windowing of the time domain waveform [62], and spectral estimation methods [63]. Furthermore, is always desirable to suppress all unwanted modes close to the desired mode by choosing an appropriate excitation waveform, with the right spatial distribution and frequency content.

- *Spurious modes*

In TLM, the solution of an electromagnetic problem is reduced to the solution of an equivalent circuit problem. The continuum free space is replaced by a discrete mesh of transmission lines, and a mapping between the propagation of voltage and current pulses through the mesh and electromagnetic waves through space is established.

The TLM model, due to its discrete nature, also supports solutions that are not solutions of the continuous model. These non-physical solutions are referred to as spurious solutions or spurious modes. They are characterized by a very high spatial frequency and are strongly excited only at high frequencies. Several studies have investigated them [64-65]

The mathematical foundation for the presence of spurious modes lies in the mapping between the voltages on the link lines and the electromagnetic field quantities. Considering for example the symmetrical condensed node, twelve voltages are mapped into

six field components. The space of solutions for the TLM model has therefore dimension twelve, while the continuous system supports only six dimensional solutions. Consequently, there is a six dimensional set of voltage configurations that gives a null electromagnetic field that is solution of the numerical method itself, but not of the real physical model. A similar situation happens also in the 2D schemes, since 4 voltages are mapped into three field components.

Unless they are excited on purpose, physical and non-physical solutions are uncoupled in free space, all of them being orthogonal solutions of a discrete model. This is no longer true when sources, either primary or secondary, are present in the structure. When exciting a given structure, particular care should be taken in the spatial configuration of the exciting waveform. Whenever possible a template with the spatial distribution of the desired modes should be used.

In the presence of secondary sources, energy is exchanged between physical and spurious modes. This is particularly critical in the vicinity of sharp features such as corners and wedges, where field singularities arise.

The question of how critical the theoretical presence of these spurious solutions is as to the accuracy of the TLM simulations is still matter of strong investigation [66]. Nevertheless, the practical experience derived from the application of the TLM method to a large variety of electromagnetic problems, tends to relegate the presence of spurious solutions to a marginal role in the list of error sources.

- *Coarseness error*

The coarseness error originates in regions of the structure under study where the field is highly non uniform, and the TLM mesh is too coarse to resolve such steep variations. This is particularly the case in the vicinity of corners and wedges where some components of the electromagnetic field are singular. The following methods can be adopted to minimize the coarseness error:

- Use of a fine mesh around regions with a highly nonuniform field. The fine mesh can be extended throughout the computational domain, or more efficiently, it can just be confined to a local sub-section [67].

- Use nodes with special properties in the vicinity of sharp features of the structure. Such nodes would account for the overall energy stored by the field in that area leading to a global characterization of the effect introduced by the edge.

- Use the Richardson extrapolation. A sequence of simulations is performed with increasingly smaller $\Delta l$, and the sought quantities are then extrapolated for an infinitesimally small cell [68-69].

Both velocity and coarseness errors appear in the results as a shift in the frequency characteristics of the structures under study. This shift is usually towards lower frequencies (negative shift), although particular combinations of dielectric and magnetic materials may lead to a positive shift.

# Chapter 3

# Derivation of the SCN Scheme from Maxwell's Integral Equations

## 3.1 Introduction

Traditionally 3D SCN characteristics have always been derived by means of equivalent circuit approaches and by energy and charge conservation considerations [42]. Only recently several contributions have been made to establish a field theoretical foundation of the TLM method. A direct derivation of the TLM scheme from Maxwell's equations is not only of theoretical importance in establishing a connection with other finite difference methods such as Finite Difference Time Domain (FDTD), but can also provide a better understanding of the physical model behind the algorithm.

A direct derivation between the TLM and Maxwell's equations has been established first by Hang Jin et al. [54] by using differencing and averaging. Maxwell's two curl equations are discretized in both space and time, and a new coordinate system of mixed time and space is created. An averaging of the field values in this new coordinate system is performed so that a mapping between TLM parameters and field values can be established.

A second approach, based upon the application of the method of moments (MoM) to Maxwell's equations, has recently been proposed by Krumpolz [53]. Discretized field equations for the electric and magnetic field components are obtained by using, as subdomain, basis functions, triangle functions in time, and a product of two-dimensional triangle functions and rectangular pulse functions with respect to space. The propagation from the mesh nodes to the neighboring nodes, and the scattering in the mesh nodes, are expressed by Hilbert space operators. A new cell boundary mapping provides a bijective

mapping between the twenty-four electric and magnetic field components and the twenty-four incident and scattered wave amplitude at one symmetrical condensed node. A general formulation based on Maxwell's integral equations has also been proposed recently, both for two-dimensional and three dimensional cases [71-72].

The two approaches mentioned before are extremely valuable, and the results are of absolute importance in assessing the basic characteristics of the TLM method, from the evaluation of its accuracy to the dispersion analysis.

The main drawback of those approaches lies in their complexity. Concepts such as mixed space and time coordinate systems and Hilbert space are powerful and compact, but they can hide the physical understanding of the entire algorithm.

The purpose of this chapter is to describe a novel derivation of the TLM SCN scheme from the integral formulation of Maxwell's equations. The extra conditions required for the mapping between TLM parameters and field values are obtained by imposing a certain behavior of the physical model. In particular, a linear behavior for all the electromagnetic waves traveling through the TLM node is assumed.

## 3.2 Conditions imposed by Faraday's and Ampere's laws

Maxwell's two curl equations in their integral formulation are known as Faraday's and Ampere's laws respectively.

$$\oint_C \mathbf{E} \cdot d\mathbf{l} = -\mu \frac{\partial}{\partial t} \int_S \mathbf{H} \cdot d\mathbf{s} \quad ; \quad \oint_C \mathbf{H} \cdot d\mathbf{l} = \varepsilon \frac{\partial}{\partial t} \int_S \mathbf{E} \cdot d\mathbf{s} \tag{3.1}$$

$S$ represents any arbitrary regular surface bounded by the curve $C$, $\mathbf{E}$ and $\mathbf{H}$ are respectively the three-dimensional electric and magnetic fields, $\varepsilon$ and $\mu$ are the absolute medium permittivity and permeability.

In the following the general geometry for modeling a TLM node is described, together with the surfaces of integration to be chosen for equations (3.1). Consider the geometry depicted in Figure 3.1(a). The cubic space of dimension $\Delta l$ represents the unit cell of a discrete TLM mesh. The cell is assumed filled with an isotropic medium of permittivity and permeability $\varepsilon$ and $\mu$, respectively. Electric and magnetic fields tangent at the cube faces are sampled at discrete time steps.

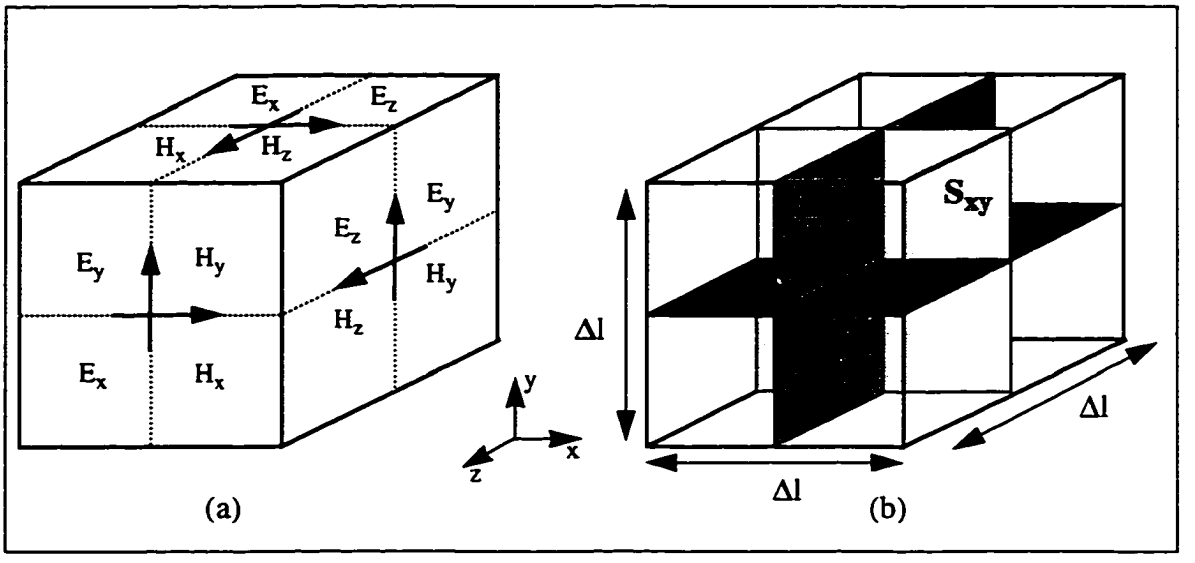


*Figure 3.1 Cubic TLM cell: (a) Field components tangent to the six faces of the cube, at different time-steps. (b) The three integration surfaces where the integral form of Maxwell's equations is evaluated*

A total of twenty-four field components, located at the six square surfaces, is therefore given. Each of them is assumed to be constant over the entire surface. Consider now Figure 3.1(b). Three mutually orthogonal planes, within the unit cell, are depicted. They form the domains of integration $S$ and $C$ for eq. (3.1).

The integration of the equations (3.1) for the three surfaces shown in Figure 3.1 are carried out according to the following basic rules:

- The value of the field components at the node center is calculated as the spatial average of the values the same field component assumes on the four surrounding cube sides. Consider for example Figure 3.2.

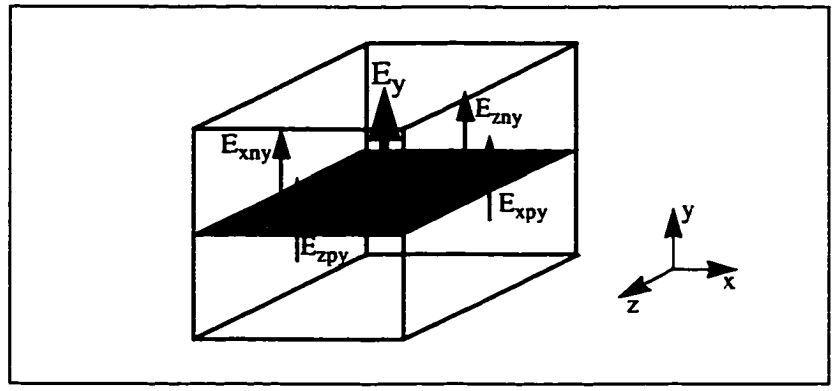


*Figure 3.2 Field at the node center as average of the surrounding fields*

The value of the electric field component directed along the $y$ direction at the node center is given by:

$$E_y = \frac{E_{xny} + E_{xpy} + E_{zny} + E_{zpy}}{4} \tag{3.2}$$

where, assuming the origin of coordinates at the center of the cube, $P_{inj}$ denotes a field component directed along the direction $j$, lying on the negative side of the cube with respect to the direction $i$, and $P_{ipj}$ denotes a field component directed along the direction $j$, lying on the positive side of the cube with respect to the direction $i$. The indices $i, j$ can be replaced by $x$, $y$, $z$, with $i, j \in \{x,y,z\}$ and $i \neq j$.

- Field values at a certain time step are given as temporal averages of the values of the same field component in the same point at a previous and successive point in time. For example:

$$E_{xpy}^{n} = \frac{E_{xpy}^{n+1/2} + E_{xpy}^{n-1/2}}{2}$$
$$E_y^n(c) = \frac{(E_y^{n+1/2}(c) + E_y^{n-1/2}(c))}{2} \tag{3.3}$$

- Time derivatives are approximated with a central difference scheme:

$$\left.\frac{\partial F}{\partial t}\right|_{t = n\Delta t} = \frac{F^{(n+1/2)\Delta t} - F^{(n-1/2)\Delta t}}{\Delta t} \tag{3.4}$$

where $\Delta t$ denotes the discrete time step.

In the following two sections the application of Faraday's and Ampere's laws to only one of the integration surfaces is shown. The final results for the other two planes are obtained in a similar manner, but only the final result will be given.

### 3.2.1 Faraday's law applied to the surface $S_{xy}$

The surface of integration $S_{xy}$, together with the normal magnetic field component, and tangent electric field components, is shown in Figure 3.3.

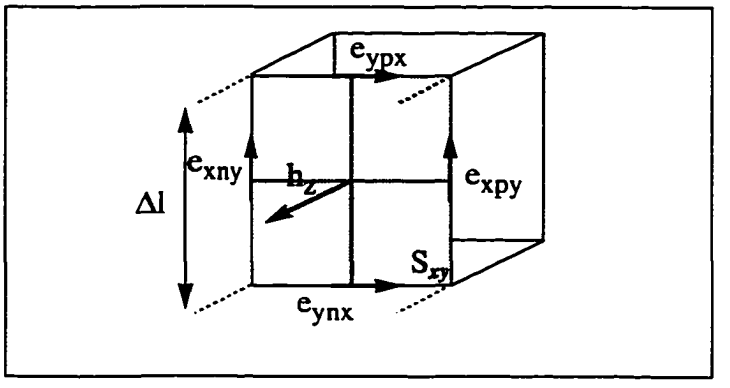


*Figure 3.3 Surface of integration $S_{xy}$ for Faraday's law*

Assuming a constant value of the field components over the domain of integration, we can write:

$$\begin{aligned} \oint_{C_{xy}} \mathbf{E}\cdot d\mathbf{l} &\approx \Delta l\,(e^n_{xpy} - e^n_{ypx} - e^n_{xny} + e^n_{ynx}) \\ -\mu\frac{\partial}{\partial t}\int_{S_{xy}} \mathbf{H}\cdot d\mathbf{s} &\approx -\frac{\mu}{\Delta t}(\Delta l)^2\left(h_z^{n+\frac{1}{2}} - h_z^{n-\frac{1}{2}}\right) \end{aligned} \tag{3.5}$$

Each of the terms contained in the equation can be expanded by performing a time averaging for the electric components, and a spatial averaging for the magnetic components, as described in the previous section.

$$\frac{1}{2}\Delta l\left[\left(e_{xpy}^{n+\frac{1}{2}}+e_{xpy}^{n-\frac{1}{2}}\right)-\left(e_{ypx}^{n+\frac{1}{2}}+e_{ypx}^{n-\frac{1}{2}}\right)-\left(e_{xny}^{n+\frac{1}{2}}+e_{xny}^{n-\frac{1}{2}}\right)+\left(e_{ynx}^{n+\frac{1}{2}}+e_{ynx}^{n-\frac{1}{2}}\right)\right]=$$
$$-\frac{\mu}{\Delta t}\frac{(\Delta l)^2}{4}\cdot\left[\left(h_{xpz}^{n+\frac{1}{2}}+h_{xnz}^{n+\frac{1}{2}}+h_{ypz}^{n+\frac{1}{2}}+h_{ynz}^{n+\frac{1}{2}}\right)-\left(h_{xpz}^{n-\frac{1}{2}}+h_{xnz}^{n-\frac{1}{2}}+h_{ypz}^{n-\frac{1}{2}}+h_{ynz}^{n-\frac{1}{2}}\right)\right] \tag{3.6}$$

Grouping together the **E** and **H** components relative to the **same cell side** and **time step**, and after defining the transformations (3.7), we obtain the equation (3.8). Note that, due to the transformations (3.7), both the quntities E and H have the dimensions of Volts, and can therefore be linearly combined as shown in (3.8).

$$\begin{aligned} E_{xpy}^{n\pm1/2} &= \Delta l e_{xpy}^{n\pm1/2} & E_{ypx}^{n\pm1/2} &= \Delta l e_{ypx}^{n\pm1/2} \\ E_{xny}^{n\pm1/2} &= \Delta l e_{xny}^{n\pm1/2} & E_{ynx}^{n\pm1/2} &= \Delta l e_{ynx}^{n\pm1/2} \\ H_{xpz}^{n\pm1/2} &= Z_0\Delta l h_{xpz}^{n\pm1/2} & H_{ypz}^{n\pm1/2} &= Z_0\Delta l h_{ypz}^{n\pm1/2} \\ H_{xnz}^{n\pm1/2} &= Z_0\Delta l h_{xnz}^{n\pm1/2} & H_{ynz}^{n\pm1/2} &= Z_0\Delta l h_{ynz}^{n\pm1/2} \end{aligned} \tag{3.7}$$

$$\text{where} \qquad Z_0 = \frac{\mu}{\Delta t}\frac{\Delta l}{2}$$

$$[E_{xpy}+H_{xpz}]^{n+1/2}-[E_{ypx}-H_{ypz}]^{n+1/2}-[E_{xny}-H_{xnz}]^{n+1/2}+$$
$$[E_{ynx}+H_{ynz}]^{n+1/2}=-[E_{xpy}-H_{xpz}]^{n-1/2}+[E_{ypx}+H_{ypz}]^{n-1/2}+ \tag{3.8}$$
$$[E_{xny}+H_{xnz}]^{n-1/2}-[E_{ynx}-H_{ynz}]^{n-1/2}$$

Equ. (3.8) can be written in a more compact form introducing the quantities ${}_nV^r$, ${}_nV^i$, reported in (3.9), that represent a combination of normalized electric and magnetic fields. They have the dimension of a voltage, and we refer to them as incident and reflected voltages at the instant $n$ [1]. An incident voltage, indicated with a letter *i* as a superscript, is associated with electromagnetic waves *entering* the TLM cell at time *(n-1/2)*$\Delta t$, while a reflected voltage, indicated with a letter *r* as a superscript, is associated with electromagnetic waves *leaving* the TLM cell at time *(n+1/2)*$\Delta t$. The polarization of each traveling voltage is described, following the traditional SCN notation adopted by Johns

[45], with a subscript number ranging between 1 and 12. The resulting equation is reported in (3.10).

$$
\begin{aligned}
{}_{2n}V^{r}_{11} &= [E_{xpy} + H_{xpz}]^{n+1/2} & {}_{2n}V^{i}_{11} &= [E_{xpy} - H_{xpz}]^{n-1/2} \\
{}_{2n}V^{r}_{12} &= [E_{ypx} - H_{ypz}]^{n+1/2} & {}_{2n}V^{i}_{12} &= [E_{ypx} + H_{ypz}]^{n-1/2} \\
{}_{2n}V^{r}_{3} &= [E_{xny} - H_{xnz}]^{n+1/2} & {}_{2n}V^{i}_{3} &= [E_{xny} - H_{xnz}]^{n-1/2} \\
{}_{2n}V^{r}_{1} &= [E_{ynx} + H_{ynz}]^{n+1/2} & {}_{2n}V^{i}_{1} &= [E_{ynx} - H_{ynz}]^{n-1/2}
\end{aligned}
\tag{3.9}
$$

$$
{}_{n}V^{r}_{11} - {}_{n}V^{r}_{12} - {}_{n}V^{r}_{3} + {}_{n}V^{r}_{1} = -({}_{n}V^{i}_{11} - {}_{n}V^{i}_{12} - {}_{n}V^{i}_{3} + {}_{n}V^{i}_{1}) \tag{3.10}
$$

## 3.2.2 Ampere's law applied to the surface $S_{xy}$

The surface of integration $S_{xy}$, together with the normal electric field component, and tangent magnetic field components, are shown in Figure 3.3.

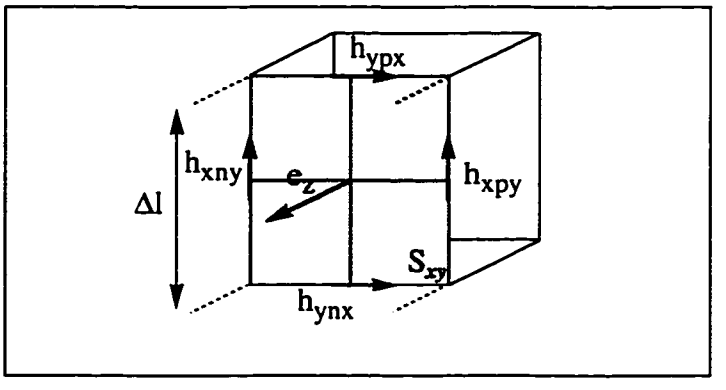


*Figure 3.4 Surface of integration $S_{xy}$ for Ampere's law*

Assuming a constant value of the field components over the domain of integration, we can write:

1. A more logical choice would appear to be $V^{i}_{n+1/2}$, $V^{r}_{n-1/2}$, thus associating the scattering process with a time delay whereas the propagation is instantaneous. In terms of implementation of the TLM algorithm it is irrelevant whether the time delay is associated with the scattering or the propagation. Since the scattering process is traditionally considered instantaneous, we define both $V^{i}$ and $V^{r}$ at the same instant $n$ at which the scattering is performed.

$$\oint_{C_{xy}} \mathbf{H}\cdot d\mathbf{l} = \Delta l\,(h^n_{xpy} - h^n_{ypx} - h^n_{xny} + h^n_{ynx})$$
$$\varepsilon\frac{\partial}{\partial t}\int_S \mathbf{E}\cdot d\mathbf{s} = \frac{\varepsilon}{\Delta t}(\Delta l)^2\left(e_z^{n+\frac{1}{2}} - e_z^{n-\frac{1}{2}}\right) \tag{3.11}$$

Each of the terms contained in the equation can be expanded by performing a time averaging at the electric components, and a spatial averaging for the magnetic components.

$$\frac{1}{2}\Delta l\left[\left(h_{xpy}^{n+\frac{1}{2}} + h_{xpy}^{n-\frac{1}{2}}\right) - \left(h_{ypx}^{n+\frac{1}{2}} + h_{ypx}^{n-\frac{1}{2}}\right) - \left(h_{xny}^{n+\frac{1}{2}} + h_{xny}^{n-\frac{1}{2}}\right) + \left(h_{ynx}^{n+\frac{1}{2}} + h_{ynx}^{n-\frac{1}{2}}\right)\right] =$$
$$\frac{\varepsilon}{\Delta t}\frac{(\Delta l)^2}{4}\cdot\left[\left(e_{xpz}^{n+\frac{1}{2}} + e_{xnz}^{n+\frac{1}{2}} + e_{ypz}^{n+\frac{1}{2}} + e_{ynz}^{n+\frac{1}{2}}\right) - \left(e_{xpz}^{n-\frac{1}{2}} + e_{xnz}^{n-\frac{1}{2}} + e_{ypz}^{n-\frac{1}{2}} + e_{ynz}^{n-\frac{1}{2}}\right)\right] \tag{3.12}$$

Grouping together the E and H components relative to the **same cell side** and **time step**, and after defining the transformation (3.13), we obtained the equation (3.14).

$$\begin{aligned} E_{xpy}^{n\pm 1/2} &= \Delta l e_{xpy}^{n\pm 1/2} & E_{ypx}^{n\pm 1/2} &= \Delta l e_{ypx}^{n\pm 1/2} \\ E_{xny}^{n\pm 1/2} &= \Delta l e_{xny}^{n\pm 1/2} & E_{ynx}^{n\pm 1/2} &= \Delta l e_{ynx}^{n\pm 1/2} \\ H_{xpz}^{n\pm 1/2} &= Z_0\Delta l h_{xpz}^{n\pm 1/2} & H_{ypz}^{n\pm 1/2} &= Z_0\Delta l h_{ypz}^{n\pm 1/2} \\ H_{xnz}^{n\pm 1/2} &= Z_0\Delta l h_{xnz}^{n\pm 1/2} & H_{ynz}^{n\pm 1/2} &= Z_0\Delta l h_{ynz}^{n\pm 1/2} \end{aligned} \tag{3.13}$$
$$Y_0 = \frac{\varepsilon}{\Delta t}\frac{\Delta l}{2} = \left(\frac{\mu}{\Delta t}\frac{\Delta l}{2}\right)^{-1} = \frac{1}{Z_0} \qquad \left(v = \frac{\Delta l}{\Delta t} = 2c\right) \Rightarrow \frac{\Delta l}{2\Delta t} = \frac{1}{\sqrt{\varepsilon_0\mu_0}}$$

$$[E_{xpz} - H_{xpy}]^{n+1/2} + [E_{xnz} + H_{xny}]^{n+1/2} + [E_{ypz} + H_{ypx}]^{n+1/2} +$$
$$[E_{ynz} - H_{ynx}]^{n+1/2} = [E_{xpz} - H_{xpy}]^{n-1/2} + [E_{xnz} - H_{xny}]^{n-1/2} + \tag{3.14}$$
$$[E_{ypz} - H_{ypx}]^{n-1/2} + [E_{ynz} + H_{ynx}]^{n-1/2}$$

Introducing the normalized incident and reflected voltages as reported in (3.15), the equation (3.14) can be written in a more compact notation than in (3.10).

$$
\begin{aligned}
2_nV^r_{10} &= [E_{xpz} - H_{xpy}]^{n+1/2} & 2_nV^i_{20} &= [E_{xpz} + H_{xpy}]^{n-1/2} \\
2_nV^r_{6} &= [E_{xnz} + H_{xny}]^{n+1/2} & 2_nV^i_{6} &= [E_{xnz} - H_{xny}]^{n-1/2} \\
2_nV^r_{7} &= [E_{ypz} + H_{ypx}]^{n+1/2} & 2_nV^i_{7} &= [E_{ypz} - H_{ypx}]^{n-1/2} \\
2_nV^r_{5} &= [E_{ynz} - H_{ynx}]^{n+1/2} & 2_nV^i_{5} &= [E_{ynz} + H_{ynx}]^{n-1/2}
\end{aligned}
\tag{3.15}
$$

$$
{}_nV^r_{10} + {}_nV^r_6 + {}_nV^r_7 + {}_nV^r_5 = ({}_nV^i_{10} + {}_nV^i_6 + {}_nV^i_7 + {}_nV^i_5) \tag{3.16}
$$

### 3.2.3 Complete set of conditions imposed by Maxwell's equations

The derivations described above can be carried out for the other two surfaces of integration, namely $S_{zy}$ and $S_{zx}$ (see Figure 3.1-b). In the following, the six equations derived from Maxwell's equations, together with the definition of the twelve incident and reflected voltages, are summarized.

$$
\begin{aligned}
{}_nV^r_{11} - {}_nV^r_{12} - {}_nV^r_3 + {}_nV^r_1 &= -({}_nV^i_{11} - {}_nV^i_{12} - {}_nV^i_3 + {}_nV^i_1) && \text{(a)} \\
{}_nV^r_6 - {}_nV^r_2 - {}_nV^r_{10} + {}_nV^r_9 &= -({}_nV^i_6 - {}_nV^i_2 - {}_nV^i_{10} + {}_nV^i_9) && \text{(b)} \\
{}_nV^r_7 + {}_nV^r_4 - {}_nV^r_8 - {}_nV^r_5 &= -({}_nV^i_7 + {}_nV^i_4 - {}_nV^i_8 - {}_nV^i_5) && \text{(c)} \\
{}_nV^r_{10} + {}_nV^r_7 + {}_nV^r_7 + {}_nV^r_5 &= ({}_nV^i_{10} + {}_nV^i_6 + {}_nV^i_7 + {}_nV^i_5) && \text{(d)} \\
{}_nV^r_{11} + {}_nV^r_3 + {}_nV^r_4 + {}_nV^r_8 &= ({}_nV^i_{11} + {}_nV^i_3 + {}_nV^i_4 + {}_nV^i_8) && \text{(e)} \\
{}_nV^r_{12} + {}_nV^r_1 + {}_nV^r_9 + {}_nV^r_2 &= ({}_nV^i_{12} + {}_nV^i_1 + {}_nV^i_9 + {}_nV^i_2) && \text{(f)}
\end{aligned}
\tag{3.17}
$$

$$
\begin{aligned}
{}_2{}_n V_1^r &= [E_{ynx} + H_{ynz}]^{n+1/2} & {}_2{}_n V_1^i &= [E_{ynx} - H_{ynz}]^{n-1/2} \\
{}_2{}_n V_2^r &= [E_{znx} - H_{zny}]^{n-1/2} & {}_2{}_n V_2^i &= [E_{znx} + H_{zny}]^{n+1/2} \\
{}_2{}_n V_3^r &= [E_{xny} - H_{xnz}]^{n+1/2} & {}_2{}_n V_3^i &= [E_{xny} - H_{xnz}]^{n-1/2} \\
{}_2{}_n V_4^r &= [E_{zny} + H_{znx}]^{n+1/2} & {}_2{}_n V_4^i &= [E_{zny} - H_{znx}]^{n-1/2} \\
{}_2{}_n V_5^r &= [E_{ynz} - H_{ynx}]^{n+1/2} & {}_2{}_n V_5^i &= [E_{ynz} + H_{ynx}]^{n-1/2} \\
{}_2{}_n V_6^r &= [E_{xnz} + H_{xny}]^{n+1/2} & {}_2{}_n V_6^i &= [E_{xnz} - H_{xny}]^{n-1/2} \\
{}_2{}_n V_7^r &= [E_{ypz} + H_{ypx}]^{n+1/2} & {}_2{}_n V_7^i &= [E_{ypz} - H_{ypx}]^{n-1/2} \\
{}_2{}_n V_8^r &= [E_{zpy} - H_{zpx}]^{n+1/2} & {}_2{}_n V_8^i &= [E_{zpy} + H_{zpx}]^{n-1/2} \\
{}_2{}_n V_9^r &= [E_{zpx} + H_{zpy}]^{n+1/2} & {}_2{}_n V_9^i &= [E_{zpx} - H_{zpy}]^{n-1/2} \\
{}_2{}_n V_{10}^r &= [E_{xpz} - H_{xpy}]^{n+1/2} & {}_2{}_n V_{10}^i &= [E_{xpz} + H_{xpy}]^{n-1/2} \\
{}_2{}_n V_{11}^r &= [E_{xpy} + H_{xpz}]^{n+1/2} & {}_2{}_n V_{11}^i &= [E_{xpy} - H_{xpz}]^{n-1/2} \\
{}_2{}_n V_{12}^r &= [E_{ypx} - H_{ypz}]^{n+1/2} & {}_2{}_n V_{12}^i &= [E_{ypx} + H_{ypz}]^{n-1/2}
\end{aligned}
\tag{3.18}
$$

Applying (3.2) and (3.3) to all the field components yields an expression for fields at the node center at time step $n$, in terms of incident or reflected voltages:

$$
\begin{aligned}
E_x^n &= \frac{({}_n V_1^i + {}_n V_{12}^i + {}_n V_2^i + {}_n V_9^i)}{2} & H_x^n &= \frac{({}_n V_8^i - {}_n V_4^i + {}_n V_5^i - {}_n V_7^i)}{2} \\
E_y^n &= \frac{({}_n V_3^i + {}_n V_4^i + {}_n V_8^i + {}_n V_{11}^i)}{2} & H_y^n &= \frac{({}_n V_{10}^i - {}_n V_6^i + {}_n V_2^i - {}_n V_9^i)}{2} \\
E_z^n &= \frac{({}_n V_5^i + {}_n V_6^i + {}_n V_7^i + {}_n V_{10}^i)}{2} & H_z^n &= \frac{({}_n V_{12}^i - {}_n V_1^i + {}_n V_3^i - {}_n V_{11}^i)}{2}
\end{aligned}
\tag{3.19}
$$

### 3.2.4 Derivation of the scattering matrix

From the direct application of Faraday's and Ampere's laws, six equations for twenty-four variables - twelve incident and twelve reflected voltages - have been derived (3.17). In order to define a scattering matrix [S] that provides a bijective mapping between reflected and incident voltages, six extra equations have still to be imposed. The

choice of these extra conditions is, to a certain extent, arbitrary, the lossless condition for the matrix [S] being the only condition to be satisfied:

$$[S]\,[S]^T = [I] \tag{3.20}$$

Incident and reflected voltages, as defined in (3.18), represent wave planes traveling along the three coordinate axes, sampled at the cell boundaries. Each plane wave entering the node (incident wave $V^i$) propagates through it and, after a time-step $\Delta t$, leaves the cell at the opposite face (reflected wave $V^r$). $V^i$ is incident on the node at the time $n$-1/2 while $V^r$ leaves the node at the time $n+1/2$. The propagation of six wave planes in three different directions is depicted in Figure 3.6. For each direction of propagation the two polarizations normal to the direction of propagation have been considered.

The value of the plane waves is defined only at the cell boundaries, but no condition has been so far imposed on the values they assume at the node center. Consider, for example, the picture shown in Figure 3.5. The plane wave associated with the voltage $V_6$ enters as incident wave into the TLM cell at the instant $n-1/2$, travels through the node until it reaches the node center at the instant $n$, and then leaves the node as reflected voltage $V_{10}$ at the time step $n+1/2$.

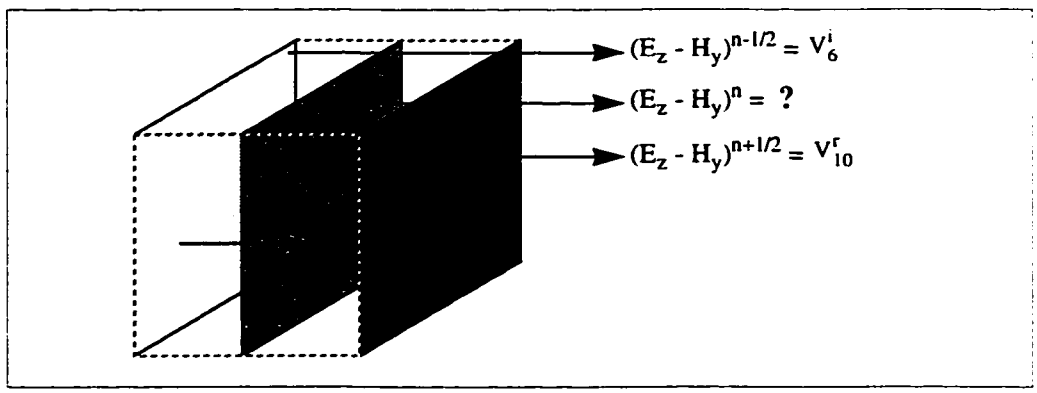


*Figure 3.5 Wave propagating along +x, (z-polarized). TLM associated voltage pulses:* $V_6^i$, $V_{10}^r$

The value assumed by the plane wave at the node center is not determined. Constraints regarding this value can be added, thus giving the six extra conditions needed for the determination of the [S] matrix. We assume a linear behavior of plane wave propagat-

ing through the node. That is the value of the waves at the node center, at the instant $n$, is equal to the average of the incident and reflected waves. For example, considering the case shown in Figure 3.5, we have:

$$(E_z - H_y)^n = \frac{(E_z - H_y)^{n-1/2} + (E_z - H_y)^{n+1/2}}{2} = V_6^i + V_{10}^r \qquad (3.21)$$

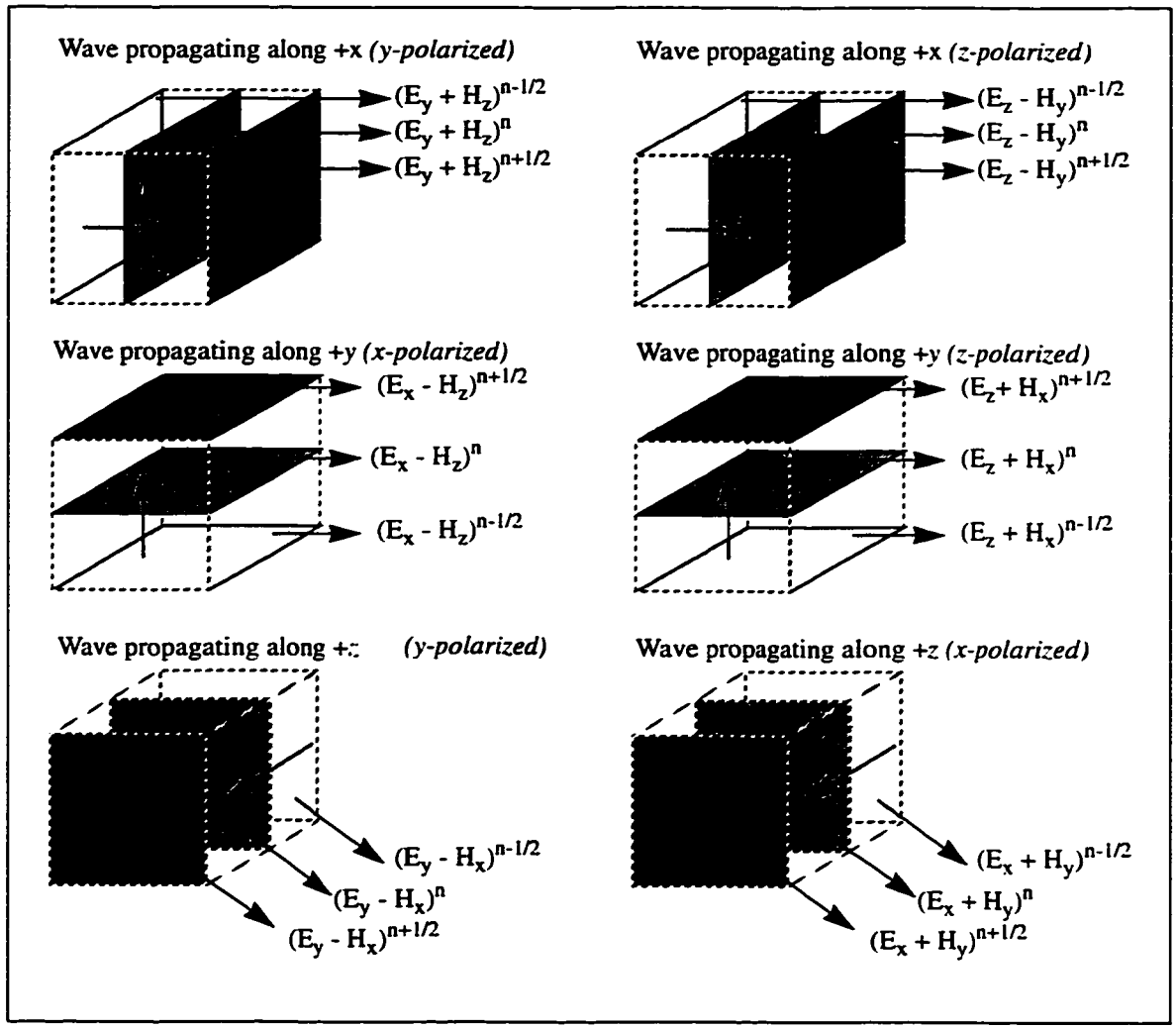


*Figure 3.6 Six plane waves propagating through the node in three different directions.*

The first term of (3.21) is then expanded by using (3.19).

Applying this averaging procedure for each direction of propagation and polarization (see Figure 3.6), yields the following six equations:

$$
\begin{aligned}
E_y^n + H_z^n &= \frac{(E_y^{n-1/2} + H_z^{n-1/2}) + (E_y^{n+1/2} + H_z^{n+1/2})}{2} = {}_nV_3^i + {}_nV_{11}^r \\
E_z^n - H_y^n &= \frac{(E_z^{n-1/2} - H_y^{n-1/2}) + (E_z^{n+1/2} - H_y^{n+1/2})}{2} = {}_nV_6^i + {}_nV_{10}^r \\
E_x^n - H_z^n &= \frac{(E_x^{n-1/2} - H_z^{n-1/2}) + (E_x^{n+1/2} - H_z^{n+1/2})}{2} = {}_nV_1^i + {}_nV_{12}^r \\
E_z^n + H_x^n &= \frac{(E_z^{n-1/2} + H_x^{n-1/2}) + (E_z^{n+1/2} + H_x^{n+1/2})}{2} = {}_nV_5^i + {}_nV_7^r \\
E_y^n - H_x^n &= \frac{(E_y^{n-1/2} - H_x^{n-1/2}) + (E_y^{n+1/2} - H_x^{n+1/2})}{2} = {}_nV_4^i + {}_nV_8^r \\
E_y^n + H_x^n &= \frac{(E_y^{n-1/2} + H_x^{n-1/2}) + (E_y^{n+1/2} + H_x^{n+1/2})}{2} = {}_nV_2^i + {}_nV_9^r
\end{aligned}
\tag{3.22}
$$

Substituting the equations (3.19) in (3.22) the following six equations are finally determined:

$$
\begin{aligned}
{}_nV_7^r &= \frac{1}{2}({}_nV_6^i + {}_nV_{10}^i + {}_nV_8^i - {}_nV_4^i) \\
{}_nV_8^r &= \frac{1}{2}({}_nV_3^i + {}_nV_7^i + {}_nV_{11}^i - {}_nV_5^i) \\
{}_nV_9^r &= \frac{1}{2}({}_nV_1^i + {}_nV_{12}^i + {}_nV_{10}^i - {}_nV_6^i) \\
{}_nV_{10}^r &= \frac{1}{2}({}_nV_9^i + {}_nV_5^i + {}_nV_7^i - {}_nV_2^i) \\
{}_nV_{11}^r &= \frac{1}{2}({}_nV_4^i + {}_nV_8^i + {}_nV_{12}^i - {}_nV_1^i) \\
{}_nV_{12}^r &= \frac{1}{2}({}_nV_2^i + {}_nV_9^i + {}_nV_{11}^i - {}_nV_3^i)
\end{aligned}
\tag{3.23}
$$

Equations (3.17) and (3.23) can be expressed in a very compact manner with a matrix

notation:

$$\begin{aligned} \mathbf{V}^{\mathbf{r}} &= \left[ {}_{n}V^{r}_{1} \cdots {}_{n}V^{r}_{12} \right]^{T} \\ \mathbf{V}^{\mathbf{i}} &= \left[ {}_{n}V^{i}_{1} \cdots {}_{n}V^{i}_{12} \right]^{T} \\ [\mathbf{P}_{r}] \cdot \mathbf{V}^{\mathbf{r}} &= [\mathbf{P}_{i}] \cdot \mathbf{V}^{\mathbf{i}} \\ \mathbf{V}^{\mathbf{r}} &= [\mathbf{S}] \cdot \mathbf{V}^{\mathbf{i}} \\ [\mathbf{S}] &= [\mathbf{P}_{r}]^{-1} \cdot [\mathbf{P}_{i}] \end{aligned} \tag{3.24}$$

where:

$$[\mathbf{P}_{i}] = \begin{bmatrix} 1 & 1 & 0 & 0 & 0 & 0 & 0 & 0 & 1 & 0 & 0 & 1 \\ 0 & 0 & 1 & 1 & 0 & 0 & 0 & 1 & 0 & 0 & 1 & 0 \\ 0 & 0 & 0 & 0 & 1 & 1 & 1 & 0 & 0 & 1 & 0 & 0 \\ 0 & 0 & 0 & 1 & -1 & 0 & 1 & -1 & 0 & 0 & 0 & 0 \\ 0 & -1 & 0 & 0 & 0 & 1 & 0 & 0 & 1 & -1 & 0 & 0 \\ 1 & 0 & -1 & 0 & 0 & 0 & 0 & 0 & 0 & 0 & 1 & -1 \\ 0 & 0 & 0 & 0 & 0 & 0 & 0 & 0 & 0 & 0 & 0 & 1 \\ 0 & 0 & 0 & 0 & 0 & 0 & 0 & 0 & 1 & 0 & 0 & 0 \\ 0 & 0 & 0 & 0 & 0 & 0 & 0 & 1 & 0 & 0 & 0 & 0 \\ 0 & 0 & 0 & 0 & 0 & 0 & 0 & 0 & 0 & 0 & 1 & 0 \\ 0 & 0 & 0 & 0 & 0 & 0 & 0 & 0 & 0 & 1 & 0 & 0 \\ 0 & 0 & 0 & 0 & 0 & 0 & 1 & 0 & 0 & 0 & 0 & 0 \end{bmatrix} \tag{3.25}$$

$$[\mathbf{P}_{r}] = \frac{1}{2} \begin{bmatrix} 2 & 2 & 0 & 0 & 0 & 0 & 0 & 0 & 2 & 0 & 0 & 2 \\ 0 & 0 & 2 & 2 & 0 & 0 & 0 & 2 & 0 & 0 & 2 & 0 \\ 0 & 0 & 0 & 0 & 2 & 2 & 2 & 0 & 0 & 2 & 0 & 0 \\ 0 & 0 & 0 & -2 & 2 & 0 & -2 & 2 & 0 & 0 & 0 & 0 \\ 0 & 2 & 0 & 0 & 0 & -2 & 0 & 0 & -2 & 2 & 0 & 0 \\ -2 & 0 & 2 & 0 & 0 & 0 & 0 & 0 & 0 & 0 & -2 & 2 \\ 0 & 1 & -1 & 0 & 0 & 0 & 0 & 0 & 1 & 0 & 1 & 0 \\ 1 & 0 & 0 & 0 & 0 & -1 & 0 & 0 & 0 & 1 & 0 & 1 \\ 0 & 0 & 1 & 0 & -1 & 0 & 1 & 0 & 0 & 0 & 1 & 0 \\ -1 & 0 & 0 & 1 & 0 & 0 & 0 & 1 & 0 & 0 & 0 & 1 \\ 0 & -1 & 0 & 0 & 1 & 0 & 1 & 0 & 1 & 0 & 0 & 0 \\ 0 & 0 & 0 & -1 & 0 & 1 & 0 & 1 & 0 & 1 & 0 & 0 \end{bmatrix} \tag{3.26}$$

$$[S] = \frac{1}{2}\begin{bmatrix} 0 & 1 & 1 & 0 & 0 & 0 & 0 & 0 & 1 & 0 & -1 & 0 \\ 1 & 0 & 0 & 0 & 0 & 1 & 0 & 0 & 0 & -1 & 0 & 1 \\ 1 & 0 & 0 & 1 & 0 & 0 & 0 & 1 & 0 & 0 & 0 & -1 \\ 0 & 0 & 1 & 0 & 1 & 0 & -1 & 0 & 0 & 0 & 1 & 0 \\ 0 & 0 & 0 & 1 & 0 & 1 & 0 & -1 & 0 & 1 & 0 & 0 \\ 0 & 1 & 0 & 0 & 1 & 0 & 1 & 0 & -1 & 0 & 0 & 0 \\ 0 & 0 & 0 & -1 & 0 & 1 & 0 & 1 & 0 & 1 & 0 & 0 \\ 0 & 0 & 1 & 0 & -1 & 0 & 1 & 0 & 0 & 0 & 1 & 0 \\ 1 & 0 & 0 & 0 & 0 & -1 & 0 & 0 & 0 & 1 & 0 & 1 \\ 0 & -1 & 0 & 0 & 1 & 0 & 1 & 0 & 1 & 0 & 0 & 0 \\ -1 & 0 & 0 & 1 & 0 & 0 & 0 & 1 & 0 & 0 & 0 & 1 \\ 0 & 1 & -1 & 0 & 0 & 0 & 0 & 0 & 1 & 0 & 1 & 0 \end{bmatrix} \tag{3.27}$$

The obtained scattering matrix is identical to the SCN scattering matrix (1.12) derived by Johns [45] using only energy and charge conservation principles.

# 3.3 Conclusion

In this chapter the symmetrical condensed node scattering scheme has been derived directly from the application of the integral formulation of Maxwell's equations, namely Faraday's and Ampere's laws.

A cubic portion of space bounded by six reference planes has been chosen as model for a TLM cell. Transverse electromagnetic field components were sampled at each boundary plane. Traveling wave amplitudes have been associated with linear combinations of the transverse field components, and pulses incident upon the cell and reflected from it have been defined. Plane waves entering as incident waves in the TLM cell at the instant $n-1/2$, travel through the node, reach the node center at the instant $n$, and then leave the node as reflected waves at the time step $n+1/2$. Six equations linking incident and reflected waves were directly given by Faraday's and Ampere laws applied upon surfaces of integration within the TLM cell. The other six equations were determined by imposing a linear behavior for each of the waves propagating through the node. Thus, the value for a given plane wave at the node center was set equal to the average of the value of the same wave when entering and leaving the node.

The scattering matrix relating reflected and incident waves amplitudes has then been determined with simple matrix operations, and found to be equal to the scattering matrix for the SCN derived with a different approach in [45], thus proving that the

assumption of linear behavior for wave propagating within the TLM cell respects the requirement of energy and charge conservation.

It is important to note that in the application of the Faraday's and Ampere's laws we have assumed the same cell dimensions of $\Delta l$ in all directions (cubic cell) and isotropic medium. These characteristics made it possible to find a linear combination of transverse electromagnetic fields defining incident and reflected waves consistently throughout the corresponding six equations. If one of these conditions is not met - either a non-cubic cell or a diagonal anisotropic medium is considered - then it is no longer possible to define incident and reflected pulses as in (3.18), valid for all the surfaces of integration. It is still possible to define twelve incident and reflected waves, but extra terms must be artificially added in order to compensate for the asymmetry of the problem and to satisfy Faraday's and Ampere's laws. These extra terms lead to the introduction of open and short circuited stubs. A physical interpretation in terms of plane wave averaging is however meaningless and the scattering matrix for the stub loaded SCN can not be carried out following the same approach as described in this chapter.

The derivation of the fundamental equations of the three-dimensional TLM method from the integral formulation of Maxwell's equations is most valuable not only for its importance in assessing the basic characteristics of the TLM method, but also, and above all, for the light it sheds on the physical nature of the algorithm. The relationship between electromagnetic fields and circuit parameters is clarified, and the approximations introduced by the discrete algorithm are emphasized.

Even though the subject of coarseness error has not been explicitly mentioned, the material presented in this chapter provides the background for a deep comprehension of the nature of the problem, for understanding which sources of error are introduced, and what needs to be done to minimize them. It provides therefore a solid knowledge-base upon which to build the remaining chapters of this thesis.

# Chapter 4

# Static Field Correction

## 4.1 Introduction

As outlined in the second chapter of this thesis, the TLM method belongs to the category of space discrete methods. The computational domain is discretized into a finite number of elementary cells where the electromagnetic field is assumed to have a simple behavior, very often linear.

A common drawback of space discrete techniques is the difficulty to accurately model sharp features, where highly nonuniform fields are produced. This is typically the case with corners and edges, where the electromagnetic fields are singular. This problem, which we have already referred to as coarseness error, is not accounted for in the standard TLM algorithm, and it represents very often the most serious source of inaccuracy.

In the presence of a field singularity, the assumption of linear space dependence of the electromagnetic field over a single cell is no longer acceptable, unless a very fine mesh is used. As a result the energy and the field distribution in the proximity of corners and edges are poorly represented. The coarseness error causes in general a frequency shift in the frequency domain characteristics that is unacceptable when dealing with narrow-band structures.

Another source of error related to the space discrete nature of TLM is the dispersion or velocity error. The discrete computational domain is an anisotropic, periodic structure. The mesh can be considered approximately continuous only if it is extremely fine compared with the smallest wavelength of interest. As a result the maximum cell size $\Delta l$ must be much less than $\lambda_{min}$. Typically a value of $\Delta l=\lambda_{min}/20$ yields a dispersion error of less than one percent.

A comparison between the dispersion and the coarseness error reveals that the coarseness error is the dominant source of inaccuracies in most of the practical cases and represents the most severe limitation to the maximum admissible $\Delta l$. In particular, it is known that, in the presence of certain discontinuities such as sharp knife edges, the convergence of the discrete solutions decays from a quadratic to a linear behavior [16]. The decline of FDTD and TLM methods from second order to first order accurate algorithms has been recently proved by De Menezes et al., who solved analytically the difference equations for structures containing knife edge discontinuities [74].

One way to reduce the coarseness error is to use an extremely fine mesh, but this quickly leads to unacceptable memory and time requirements. A better approach is to use a variable or multigrid mesh, so that a higher resolution can be obtained in the discontinuity region [75]. In this case the resources would be still larger than those required by a uniform coarser mesh fixed by the dispersion error only.

A solution based on a local modification of the standard time domain algorithm would have the advantage of requiring the same computational load as a coarse mesh, but introducing the necessary correction only in the region of interest, and without altering the algorithm throughout the remaining computational domain. Such a modification has to be based on the *a-priori* knowledge of the field behavior within the singular region, so that one or more coarse *smart* cells surrounding the corner embed the edge properties.

In this chapter a novel approach to incorporate knowledge of the static field behavior in the vicinity of singularities in a three-dimensional TLM mesh is described. A TLM corner node, containing the information on the presence of the singular field, will be derived. The procedure is systematic and does not require optimization of the correcting elements. As a result, relatively coarse TLM meshes may be used to obtain highly accurate results, within the dispersion error margin, across a wide frequency range. The new scheme will be validated via simulation of canonical problems.

In section 4.2 a general overview of field singularities, with particular emphasis on the static expansion of singular fields, will be given. Section 4.3 will focus on the description of singular field regions by TLM, and will provide an intuitive description of the causes of the coarseness error. In section 4.4 a new scattering scheme for a so-called *corner node*, based on a static expansion of the electromagnetic field, will be presented and validated via simulations of canonical problems. Final conclusions will then be drawn and discussed.

## 4.2 Sharp corners and singular fields

Wedges in real structures are often quite sharp; their model is usually assumed to be infinitely sharp. This idealization is valid only when the radius of curvature of the edge is negligible with respect to other relevant lengths, and it leads to the presence of singularities of the fields. The singular behavior at an edge follows from the requirement that the energy density near the edge must remain integrable, that is, the energy must be finite [76-77]. Consider the perfectly sharp metallic edge shown in Figure 4.1. In the vicinity of the edge the field can be expressed as a power series in r. It is assumed that this series has a dominant term $r^{\nu}$, where $\nu$ can be negative. However, the value of $\nu$ must be restricted such that the energy stored in any region surrounding the edge remains finite. To impose a finite energy is equivalent to imposing the condition:

$$\int_0^a \iint (\varepsilon|\mathbf{E}|^2 + \mu|\mathbf{H}|^2)\, r\,dr\,d\phi\,dy < \infty \tag{4.1}$$

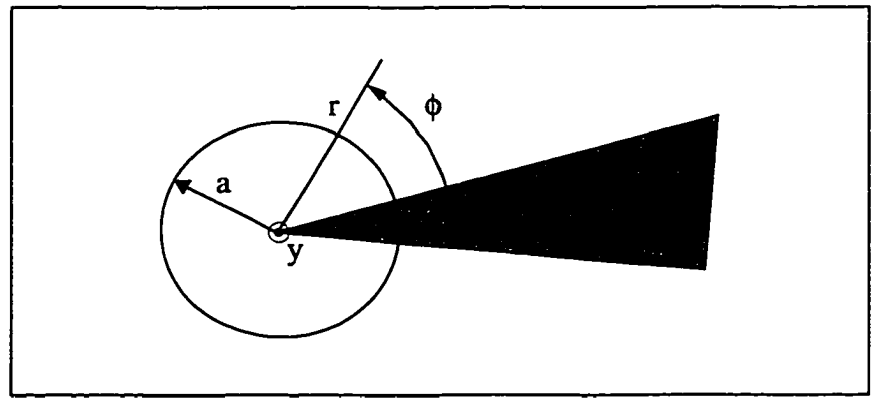


*Figure 4.1 Perfectly sharp metallic edge*

It can be proved [77] that the finite energy condition (4.1) imposes the following asymptotic behavior of the electromagnetic field:

$$\nu = \frac{\pi}{(2\pi - \alpha)}$$

$$\begin{aligned} E_y &\sim r^{\nu} & H_y &\sim \text{const} \\ H_\phi &\sim r^{\nu-1} & E_\phi &\sim r^{\nu-1} \\ H_r &\sim r^{\nu-1} & E_r &\sim r^{\nu-1} \end{aligned} \tag{4.2}$$

By virtue of (4.2) we can state that near the edge of a perfectly conducting wedge of internal angle $\alpha$ less than $\pi$, the normal components of **E** and **H** become singular, but the components of **E** and **H** tangential to the edge remain finite. In particular the tangential electric field vanishes on the edge while the tangential magnetic field assumes a finite value. The charge density $\rho_s$ on the surface, proportional to the normal component of **E**, also exhibits a singular behavior, as well as the current tangential to the edge, which is proportional to $H_\phi$.

### 4.2.1 Static Expansion

The singular behavior of the electromagnetic field near an edge is essentially static or quasi-static. In fact, close to the edge, the spatial derivatives of the fields are much larger than the time derivatives, so that the latter may be neglected in Maxwell's equations. Therefore, when *r* is very small, propagation effects are not important since the singular behavior is a local phenomenon.

The static expansion given in the following will be the basis for the derivation of a TLM corner node, as described in the next sections of this chapter. Considering the geometry of Figure 4.1, the electric and magnetic field components parallel to the wedge can be expanded as [78], where the variable t indicates a time dependance:

$$E_y(r,\phi,t) = \alpha(t)\, r^{\nu_1} \sin(\nu_1\phi) + \beta(t) \cdot r^{\nu_2} \cdot \sin(\nu_2\phi) + \gamma(t)\, r^{\nu_3} \sin(\nu_3\phi) + \ldots \tag{4.3}$$

$$H_y(r,\phi,t) = c_0(t) + c_1(t) \cdot r^{\nu_1} \cdot \sin(\nu_1\phi) + c_2(t)\, r^{\nu_2} \sin(\nu_2\phi) + \ldots \tag{4.4}$$

where $\nu_n = \frac{n\pi}{(2\pi - \alpha)}$.

The case of a knife edge ($\alpha$=0) will be considered in particular (Figure 4.2). The expressions (4.3) and (4.4) are therefore rewritten as in (4.5) and (4.6), considering this specific case.

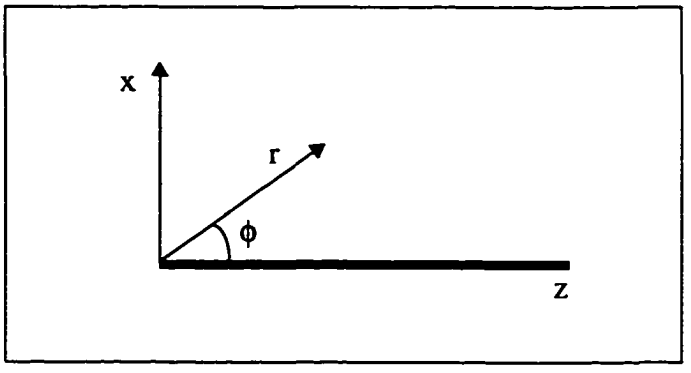


*Figure 4.2 Geometry of a knife metallic edge*

$$E_y(r,\phi,t) = \alpha(t)\, r^{\frac{1}{2}} \sin\left(\frac{\phi}{2}\right) + \beta(t) \cdot r \cdot \sin(\phi) + \gamma(t)\, r^{\frac{3}{2}} \sin\left(\frac{3}{2}\phi\right) + \ldots \qquad (4.5)$$

$$H_y(r,\phi,t) = c_0(t) + c_1(t) \cdot r^{\frac{1}{2}} \cdot \sin\left(\frac{\phi}{2}\right) + c_2(t)\, r \sin(\phi) + \ldots \qquad (4.6)$$

# 4.3 TLM representation of singular field regions

In this section the modeling of a singular field region with the TLM method will be described. Particular emphasis will be given to the limitations of the model.

As we have seen previously, the electromagnetic field distribution is discretized in the TLM method into a finite number of cells, each of which is assumed to contain a field of constant value. While this approximation is valid when the field has a smooth distribution, it becomes very inaccurate when the field is highly nonuniform, such as in the presence of a singularity.

Consider for example the common case of a knife edge singularity (Figure 4.2) where the normal field components are known to have a singularity of the type $1/(\sqrt{r})$,

according to the expression (4.2), where $\alpha=0$, and $\nu=1/2$.

Figure 4.3 (a)-(b) depicts a three-dimensional plot of the $1/(\sqrt{r})$ function in the vicinity of the origin (similar to the field at the tip of the metallic wedge) and the equivalent TLM representation, with the continuous field spatially sampled with rectangular pulse functions. It is clear that TLM gives a good description of the field only far away from the corner, where the field behaves smoothly, whereas in the vicinity of the singular region the model is obviously inadequate.

As a consequence, the energy stored in a volume containing the singularity, proportional to the integral of $|E|^2$ and $|H|^2$, is also misrepresented. Hence, the reactive load associated with the energy storage is poorly modeled, and therefore a frequency shift error is introduced in the TLM simulation results.

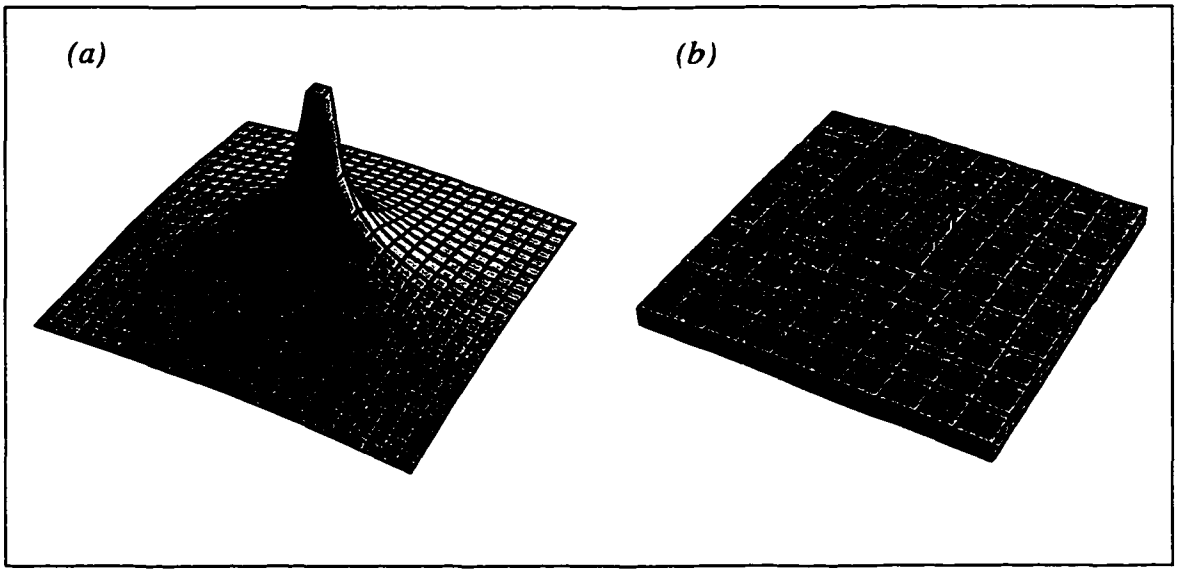


*Figure 4.3 Three-dimensional plot of: (a) $1/(\sqrt{r})$ function, with singularity in the origin. (b) equivalent representation with the TLM modeling.*

The impact of the coarseness error appears clearly when we analyze even a simple problem such as the calculation of the resonant frequency of a finned cavity. In Figure 4.4 we have drawn the geometry of the cavity and the plot of the first resonant frequency for three different discretizations. Assuming that the value of the resonant frequency obtained with the finest mesh is the most accurate, we can determine the relative error for

each discretization, and compare it with the dispersion error. The dispersion error is the only error present in the analysis of the resonant frequency of the empty cavity. Even though this is an approximation, it gives nevertheless a clear picture of the magnitude of the two different phenomena. Unless only free wave propagation is considered, the coarseness error represents the most serious cause of inaccuracy.

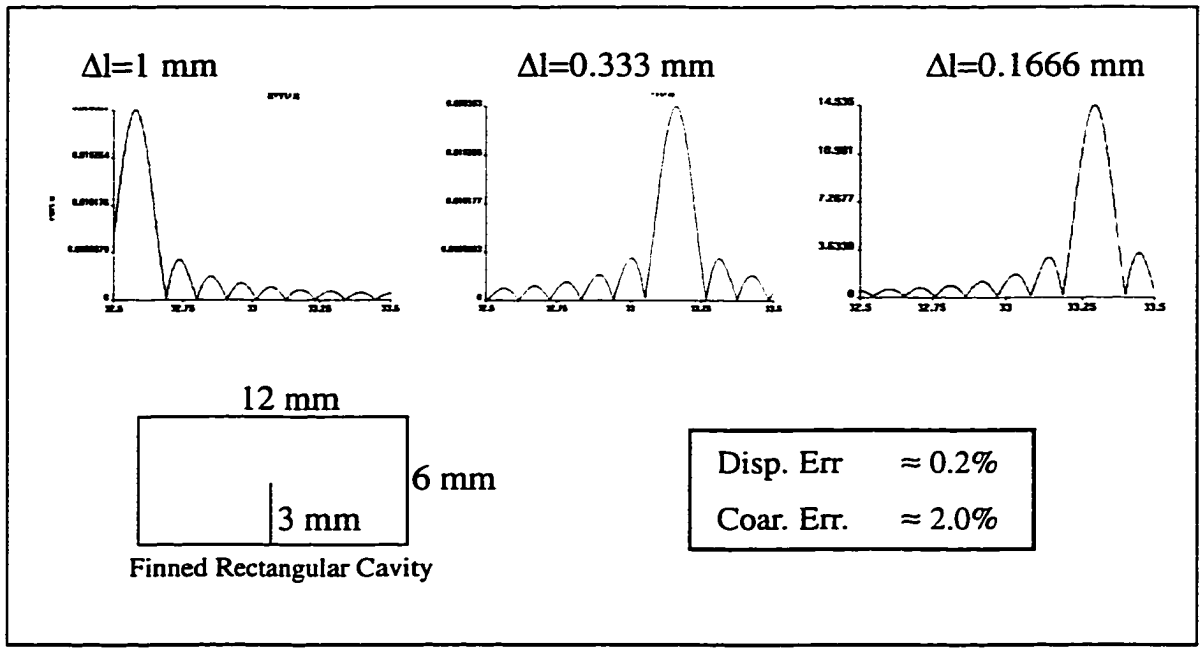


*Figure 4.4 Resonant frequency of a finned cavity, and comparison between dispersion and coarseness error.*

One possible way to reduce this error is to locally modify the amount of energy stored around the edge. Even though the field remains poorly described, the error in the resonant frequency decreases. Since a singular field is essentially a static field, this *a priori* knowledge can be introduced in the method, thus yielding an improvement in accuracy.

In the next section the static expansions (4.5) -(4.6) will be used to derive a local modification of the algorithm in the vicinity of a knife edge. A new scattering scheme for a so-called *corner node* will be determined.

# 4.4 TLM Corner Node

Consider Maxwell's equations in cylindrical coordinates $y$-r-$\phi$:

$$\frac{\partial E_r}{\partial y} - \frac{\partial E_y}{\partial r} = -\mu \frac{\partial H_\phi}{\partial t} \quad \text{(a)}$$
$$\frac{\partial H_r}{\partial y} - \frac{\partial H_y}{\partial r} = \varepsilon \frac{\partial E_\phi}{\partial t} \quad \text{(b)} \qquad (4.7)$$

Equations (4.7) (a) and (b) will be approximated in the vicinity of a knife edge by making use of equations(4.5) -(4.6) for the $E_y$ and $H_y$ components, and by substituting a central difference scheme for the time derivative.

### 4.4.1 TM-Polarization

Consider the case of the knife edge embedded in a TLM mesh shown in Figure 4.5.

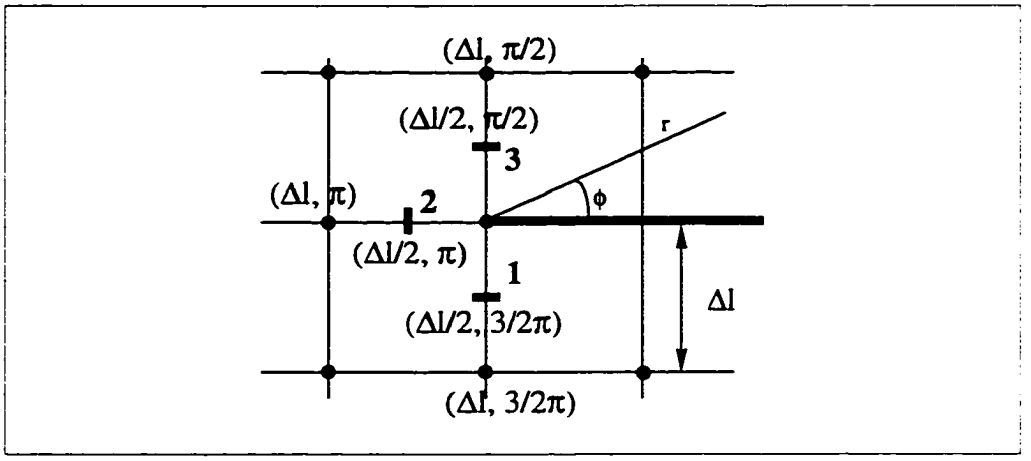


*Figure 4.5 Knife edge in a TLM mesh; the edge is placed on TLM nodes*

We want to implement the equation (4.7)-(a) including the edge condition (4.3) at the three TLM link lines. At three middle points we have:

$$\mu_0 \frac{\partial H_\phi(\frac{\Delta}{2}, \phi, t)}{\partial t} = \frac{\partial E_y(\frac{\Delta}{2}, \phi, t)}{\partial r} - \frac{\partial E_r(\frac{\Delta}{2}, \phi, t)}{\partial y} \qquad (4.8)$$

Replacing the time derivative with the central difference scheme, and recalling the mapping between voltages and fields between link lines in the 3D-SCN node (see equations (3.18)), the following relationship for the voltage pulses incident at the points 1,2,3

can be determined:

$$({}_kV^r - {}_kV^i) - ({}_{k-1}V^r - {}_{k-1}V^i) = Z_0 \frac{\Delta l \Delta t}{\mu_0} \cdot \left(\frac{\partial E_y}{\partial r} - \frac{\partial E_r}{\partial y}\right) \tag{4.9}$$

where $Z_0$ is link line characteristic impedance, ${}_kV^r$ are the voltage pulses incident on the points 1,2,3 from *the corner node* and ${}_kV^i$ are the voltage pulses incident on the points 1,2,3 from *the external nodes* at the $k^{th}$ iteration. Note that the correction algorithm exploits the reflected and incident voltages at the corner node during the previous time step, thus increasing the information contained in that cell. The polarization of the voltage pulses has not been explicitly defined since it depends on the actual direction of the metallic wedge in the structure under investigation, and it is therefore a information that must be provided only during the implementation of the algorithm.

The second term of equation (4.9) can be evaluated using the static expansion (4.3). Considering only the first term of the expansion, we have:

$$\frac{\partial E_y\left(\frac{\Delta l}{2}, \phi, t\right)}{\partial r} = \frac{1}{2}\alpha(t)\left(\frac{\Delta l}{2}\right)^{-\frac{1}{2}} \sin\left(\frac{\phi}{2}\right) = \frac{1}{\sqrt{2}} \frac{E_y(\Delta l, \phi)}{\Delta l} \tag{4.10}$$

Thus, the value of the derivative is expressed as a function of the value of the electric field at the adjacent node. Note that in a standard central difference scheme, such as that used in the FDTD method, the expression (4.10) would be written as:

$$\left.\frac{\partial E_y\left(\frac{\Delta l}{2}, \phi, t\right)}{\partial r}\right|_{TLM} = \frac{E_y(\Delta l, \phi) - E_y(0, \phi)}{\Delta l} = \frac{E_y(\Delta l, \phi)}{\Delta l} \tag{4.11}$$

where $E_y$ has been considered null on the corner.

The difference between the standard central difference scheme and the expression derived from the static expansion resides in the multiplying term $1/(\sqrt{2})$. This extra fac-

tor can be interpreted as a local modification of the permeability in equation (4.7)(a). By increasing the permeability of the cells surrounding the corner we increase the magnetic energy stored in that region, compensating in this way for the poor representation of the energy in that area.

The modified scattering procedure for the first-order approximation is obtained by solving equation (4.9) with respect to ${}_kV^r$, and is given by:

$$ {}_kV^r = {}_kV^i + {}_{k-1}V^r - {}_{k-1}V^i - Z_0 \frac{\Delta l \Delta t}{\mu_0} \cdot \left[ \frac{{}_{k-1/2}E_y(\Delta l, \phi)}{\sqrt{2}\Delta l} - \frac{\partial E_r}{\partial y} \right] \tag{4.12} $$

A higher order approximation can be performed considering the first three terms of the expansion (4.3). The derivative of $E_y$ at the three middle points is then:

$$ \begin{aligned} \frac{\partial E_y(\frac{\Delta l}{2}, \phi, t)}{\partial r} = \frac{1}{2}\alpha(t)\,(\frac{\Delta l}{2})^{-\frac{1}{2}} \sin(\frac{\phi}{2}) + \beta(t)\sin(\phi) + \\ \frac{3}{2}\gamma(t)\,(\frac{\Delta l}{2})^{\frac{1}{2}} \sin(\frac{3}{2}\phi) + \ldots \end{aligned} \tag{4.13} $$

where the coefficients $\alpha(t)$, $\beta(t)$, $\gamma(t)$ are unknown and have to be found at each iteration. Their value can be determined by evaluating the electric field $E_y$ at the three nodes surrounding the corner node (see Figure 4.6) at each time step and solving a linear system.

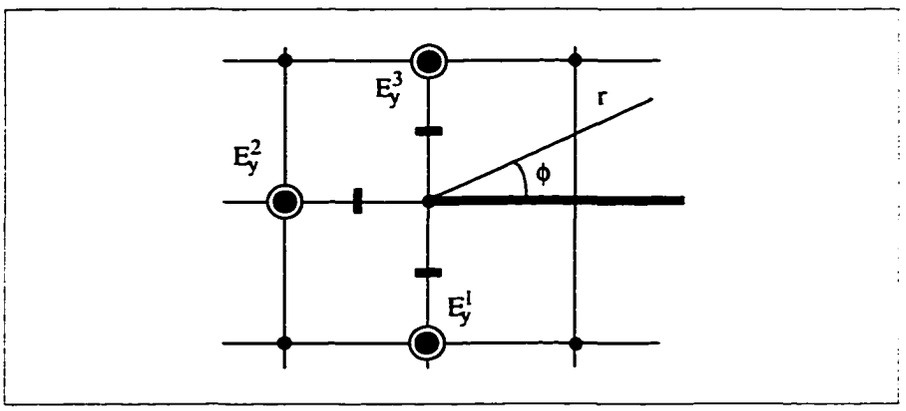


*Figure 4.6 Location of the electric field at surrounding nodes used for the evaluation of the expansion coefficients*

The solution gives values of $\alpha$, $\beta$, $\gamma$, as a function of the voltages $E^1_y$, $E^2_y$, $E^3_y$:

$$\alpha = \frac{(\sqrt{2}E_y^1 + 2E_y^2 + \sqrt{2}E_y^3)}{4r_0} \qquad \beta = \frac{(E_y^3 - E_y^1)}{2r_0^2}$$
$$\gamma = -\frac{(E_y^1 - \sqrt{2}E_y^2 + E_y^3)}{2\sqrt{2}r_0^3} \qquad r_0 = \sqrt{\Delta l} \tag{4.14}$$

The modified scattering procedure for higher-order approximation is obtained by solving (4.9) with respect to ${}_kV^r$ and using (4.14):

$$G(\phi, k) = \frac{1}{2}\alpha(k\Delta t)\left(\frac{\Delta l}{2}\right)^{-\frac{1}{2}} \sin\left(\frac{\phi}{2}\right) + \beta(k\Delta t)\sin(\phi) +$$
$$+ \left(\frac{3}{2}\gamma(k\Delta t)\left(\frac{\Delta l}{2}\right)^{\frac{1}{2}} \sin\left(\frac{3}{2}\phi\right)\right) \tag{4.15}$$
$$V_k^r = V_k^i + V_{k-1}^r - V_{k-1}^i + \frac{\Delta l^2}{2} \cdot \left(G(\phi, k) - \frac{\partial E_r}{\partial y}\right)$$

The spatial derivative $\partial E_r/\partial y$, present in (4.12) and (4.15), is evaluated with a central difference scheme.

### 4.4.2 TE-Polarization

The calculations for the TE polarization (equation 4.7(b)) are carried out in a similar manner as for the TM polarization. Considering the first of the equations (4.7)(b), and the edge condition (4.3), together with the mapping between voltages and fields between link lines in the SCN node, the following scattering process is obtained:

$$\begin{gathered}(\text{Port}-3)\\ (V_k^r + V_k^i) - (V_{k-1}^r + V_{k-1}^i) = -\frac{\Delta l \Delta t}{\varepsilon} \cdot \left(\frac{\partial H_y}{\partial r} - \frac{\partial H_r}{\partial y}\right)\\ (\text{Port}-1,2)\\ (V_k^r + V_k^i) - (V_{k-1}^r + V_{k-1}^i) = \frac{\Delta l \Delta t}{\varepsilon} \cdot \left(\frac{\partial H_y}{\partial r} - \frac{\partial H_r}{\partial y}\right)\end{gathered} \tag{4.16}$$

where the derivative of $H_y$ can be approximated as:

$$\frac{\partial H_y}{\partial r} = \frac{1}{2} c_1(t) \left(\frac{\Delta l}{2}\right)^{-\frac{1}{2}} \cos(\phi) + c_2(t) \cos\left(\frac{3}{2}\phi\right) + \ldots \tag{4.17}$$

Note that a first order approximation for the $H_y$ component would lead to the trivial condition $\frac{\partial H_y}{\partial r} = 0$. The values of the constant $c_1$ and $c_2$ can be determined by evaluating the magnetic field $H_y$ at the three nodes surrounding the corner node (see Figure 4.6) at each time step and solving a linear system as a function of the magnetic fields $H_y^1$, $H_y^2$, $H_y^3$. The solution of the linear system is reported in (4.18).

$$c_1 = \frac{(H_y^3 - H_y^1)}{\sqrt{2\Delta l}} \qquad c_2 = -\frac{(H_y^1 - 2H_y^2 + H_y^3)}{2\Delta l} \tag{4.18}$$

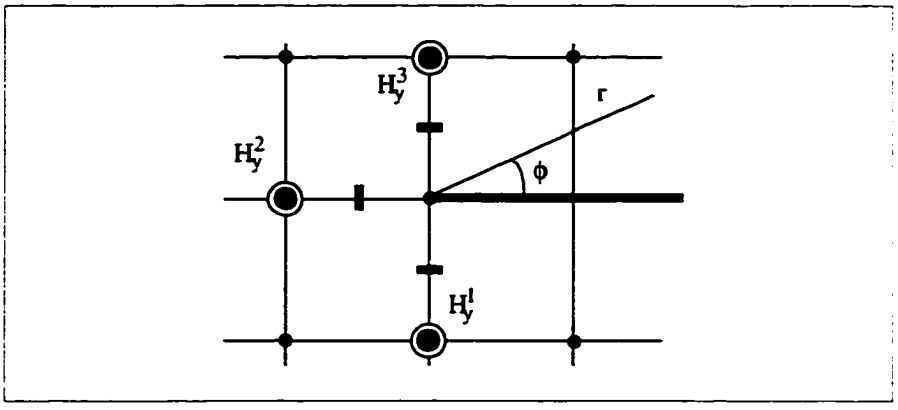


*Figure 4.7 Location of the magnetic field at surrounding modes used for the evaluation of the expansion coefficients*

Finally, the modified scattering procedure for the TE polarization is obtained by solving (4.16) with respect to ${}_kV^r$ and using (4.18):

$$G_{TE}(\phi, k) = \frac{1}{2} c_1 (k\Delta t) \left(\frac{\Delta l}{2}\right)^{-\frac{1}{2}} \cos(\phi) + c_2 (k\Delta t) \cos\left(\frac{3}{2}\phi\right)$$

$$\begin{pmatrix} \text{(Port-3)} \\ V_k^r = V_{k-1}^r + V_{k-1}^i - V_k^i - \frac{\Delta l \Delta t}{\varepsilon} \cdot \left(G_{TE}(\phi, k) - \frac{\partial H_r}{\partial y}\right) \\ \text{(Port-1, 2)} \\ V_k^r = V_{k-1}^r + V_{k-1}^i - V_k^i + \frac{\Delta l \Delta t}{\varepsilon} \cdot \left(G_{TE}(\phi, k) - \frac{\partial H_r}{\partial y}\right) \end{pmatrix} \tag{4.19}$$

The spatial derivative $\partial E_r / \partial y$ is evaluated with a central difference scheme.

A little note regarding the fact that now there are different scattering algorithms for port 3 and ports 1-2. The reason for this difference with respect to the previous case lies in the mapping between electromagnetic fields and voltage pulses sampled on the TLM cell boundaries. This mapping has been derived in chapter 3, and summarized in equation (3.18). According to this mapping the magnetic field component $H_y$ at port 3 is pro-

portional to $V^r$-$V^i$, while at the ports two and one a minus sign is present, that is $H_y$ is proportional to $V^i$-$V^r$. This difference of sign is then maintained also in (4.19).

# 4.5 Results

In order to validate the described approach, the scattering procedures (4.15)-(4.19), derived from the static field expansion, have been implemented into the TLM 3D-SCN, and used for the analysis of canonical problems. The first structure taken into consideration is a rectangular cavity with an asymmetric inductive iris in the center.

The first resonant frequency of the finned cavity have been calculated. The cavity walls have been placed between nodes and the inner fin has been placed on the nodes. The cavity has been analyzed first using the standard TLM algorithm with three different discretizations. First and higher order static corrections have been then implemented, considering only the coarsest of the three meshes.

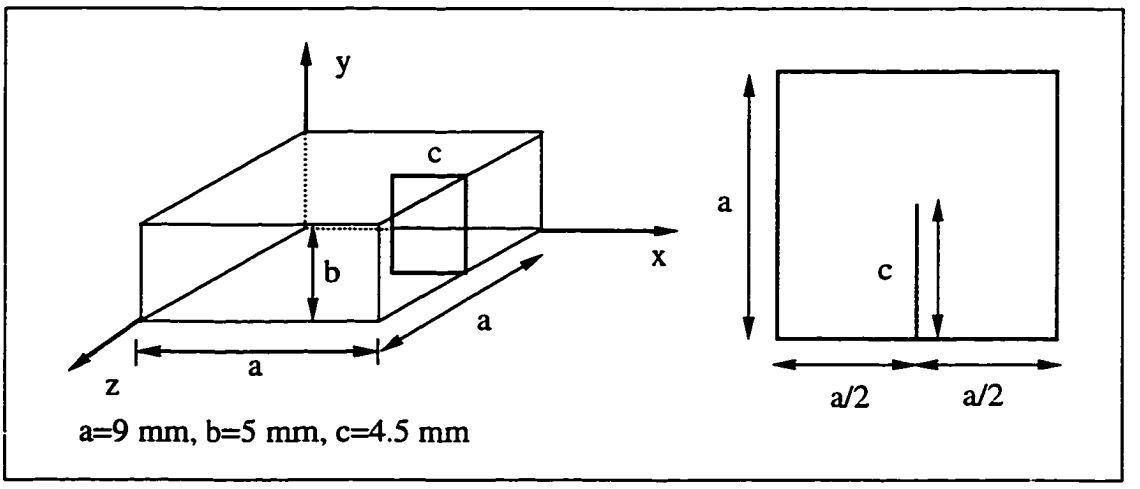


*Figure 4.8 Rectangular cavity with an asymmetric inductive iris*

The time domain waveform as well as the frequency domain results are shown in Fig. 4.9 and Fig. 4.10.

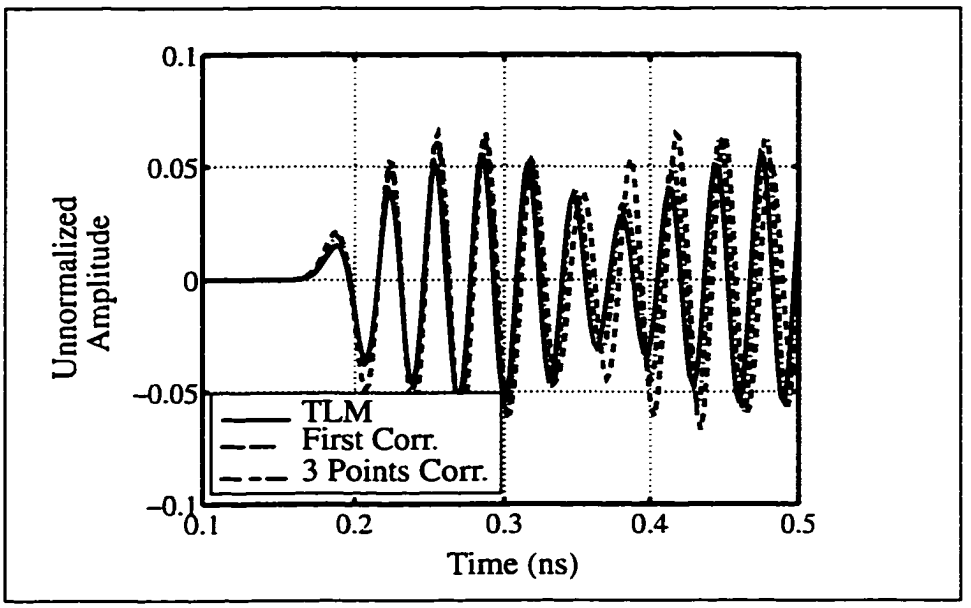


*Figure 4.9 Time domain waveform ($\Delta l$ = 1 mm)*

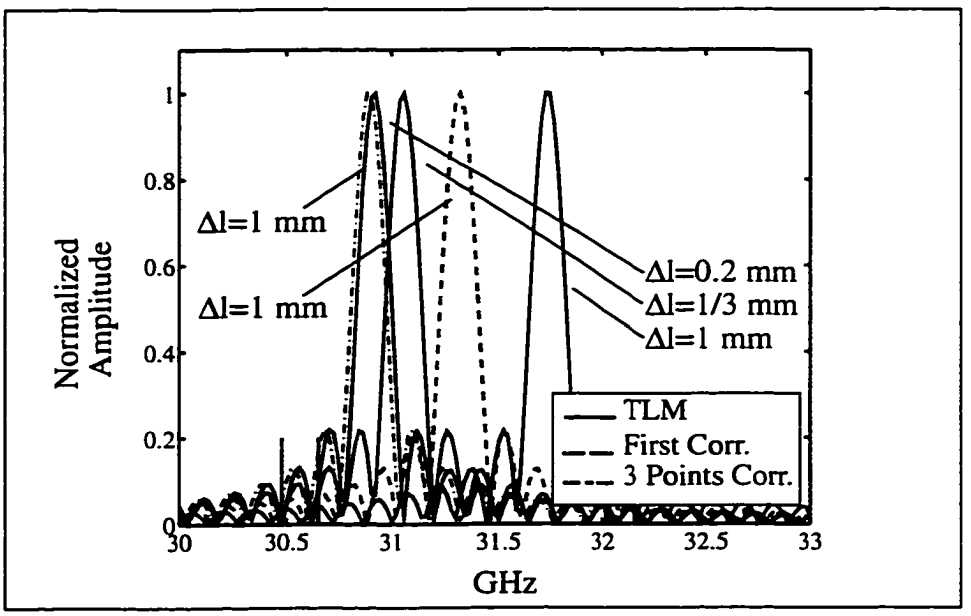


*Figure 4.10 First resonant frequency of the finned cavity. Different discretizations, with and without corner correction.*

The frequency domain results show that the coarseness error which affects the stan-

dard TLM simulations is strongly reduced by the introduction of the static correction. A reference value for the resonant frequency can be derived from the three pure TLM simulations by using a Richardson's extrapolation for Δl -> 0 [69]. It is interesting to note that the correction introduced by approximating the static field with just one term of the static expansion is already sufficient to reduce the coarseness error considerably. As expected, the higher order approximation provides a more effective correction. The results for a rectangular cavity with an asymmetric inductive iris are summarized in Table 4.1

*Table 4.1. Rectangular cavity with an asymmetric inductive iris. Resonant frequencies (GHz)*

| Δl | 1 mm | 0.333 mm | 0.2 mm | Δl -> 0 | Err. (%) |
|---|---|---|---|---|---|
| **TLM** | 31.732 | 31.062 | 30.922 | 30.708 | 3.3% |
| **1 Point Corr.** | 31.323 | - | - | | 2.0% |
| **3 Point Corr.** | 30.889 | - | - | | 0.59% |

A second structure that was examined is a parallel plate waveguide resonator with an asymmetric capacitive iris in the middle. The waveguide is terminated with a metallic wall at the two extremities, so that a resonant cavity is created.

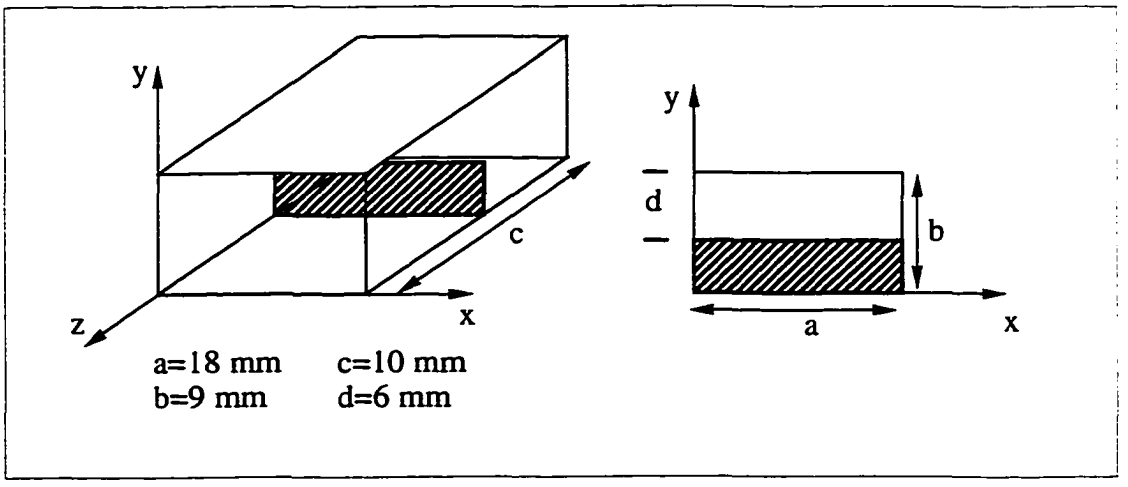


*Figure 4.11 Resonant cavity in parallel plate waveguide with capacitive coupling*

As for the previous structure, the first resonant frequency of the cavity has been cal-

culated. The cavity has been analyzed first using the standard TLM algorithm with three different discretizations. The higher order static corrections have then been implemented, considering only the coarsest of the three meshes. TLM simulations of such an elementary configuration (simple waveguide loaded with a capacitive discontinuity), are known to be affected by a large error, with results considerably shifted in the frequency domain. Moreover, a very coarse mesh has intentionally been considered in order to highlight the coarseness error and its correction. A reference value for the resonant frequency can be derived from the four pure TLM simulations by using a Richardson's extrapolation for $\Delta l \rightarrow 0$. The resonant frequencies for different discretizations are depicted in Figure 4.12 and summarized in Table 4.2.

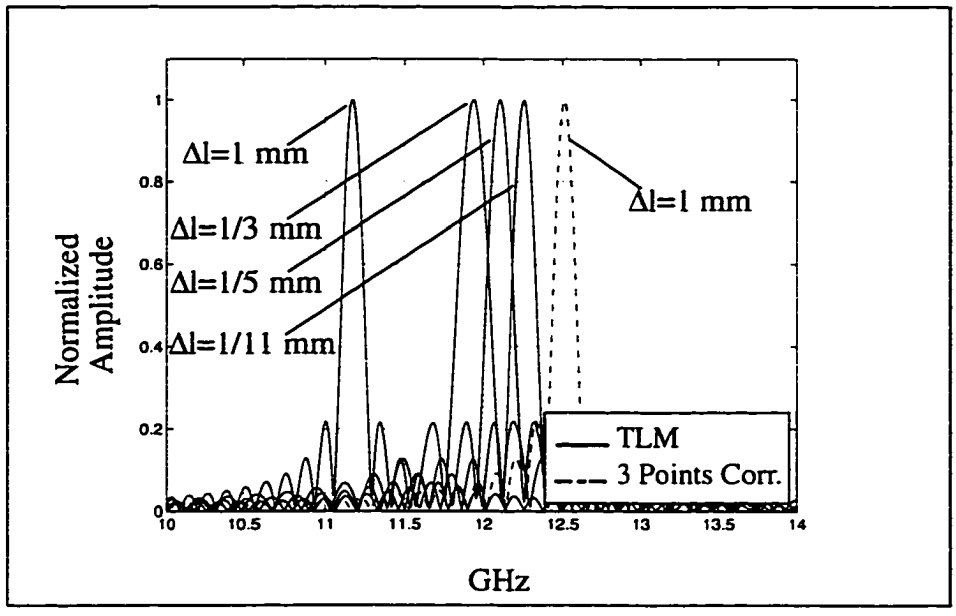


*Figure 4.12 First resonant frequency of the parallel plate waveguide cavity, loaded with a capacitive iris. Different discretizations, with and without corner correction.*

*Table 4.2. Parallel plate waveguide with capacitive iris. Resonant frequencies (GHz)*

| Δl | 1 mm | 1/3 mm | 1/5 mm | 1/11 mm | Δl->0 | Err. (%) |
|---|---|---|---|---|---|---|
| **TLM** | 11.175 | 11.935 | 12.105 | 12.260 | 12.508 | 10.6% |
| **Static Correction** | 12.510 | | - | - | | 0.02% |

Even when a very coarse mesh is used, the previous simulations show that the introduction of the static-field correction yields an improvement in the accuracy with negligible impact on the computational time[1]. These results are consistent with those obtained with a standard TLM algorithm with cell sizes five to six times smaller, but are obtained with a significant saving in computational effort.

Long term instabilities have been observed in the simulation of structures where a strong coupling between TE and TM polarizations is present. This is an undesirable characteristic common to those techniques where time marching algorithms are modified by locally altering the update equations, as in the method proposed in this chapter [79-80]. The effect of changing any individual term in an update equation on the stability of a complex time domain algorithm such as TLM is extremely difficult to predict [81]. A possible explanation could be associated with the presence of spurious solutions in the discrete TLM solutions. Physical and non-physical solutions, usually uncoupled in a free space propagation, are strongly coupled in the presence of sharp discontinuities. The modified algorithm, based upon a physical assumption of static field, could therefore disrupt the energy conservation of the discrete TLM scheme.

In order to avoid such a problem, it is necessary to derive correction techniques for which stability is an intrinsic characteristic. Circuit-based techniques have, for example, such an appealing feature. Given any complex passive circuit topology, it is known, from circuit theory theorems, that the system is unconditionally stable. Besides the guarantee

1. The computational time can vary according to many factors, such as the desired frequency resolution, whether the structure under study is highly resonant, and type of excitation waveform used. In the particular case of the resonator of Fig. 4.11, the simulation time for the finest discretization (Δl = 1/11 mm) is approximately 7.5 hours, running on a HP Apollo 9000 workstation. The same structured, simulated using the corner correction and the coarsest discretization (Δl = 1 mm) takes less than 5 minutes.

of stability, the derivation of an equivalent circuit, as a description of a singular field region, would also have the advantage of merging very easily with the standard TLM algorithm.

## 4.6 Conclusion

A novel systematic procedure to reduce the coarseness error present in 3D-TLM simulations has been described in this chapter. The method introduces the correct field singularity by exploiting the previous incident and reflected link-line voltages surrounding the corner node. The procedure requires negligible additional operations and leads to a saving in computational time and memory that is up to two orders of magnitude better.

The described technique achieves a highly accurate characterization of structure containing sharp edges by including *a priori* knowledge of the static field behavior in the singular field region. The inclusion of this extra information in the algorithm however is achieved by altering the standard TLM update equations, and these alterations can result in long term instabilities.

In the next chapter a different technique for the minimization of the coarseness error, based on the derivation of an equivalent circuit from the Green's function of a uniform metallic wedge, will be explored.

# Chapter 5

# Equivalent Circuit Derivation from the Green's Function of a Metallic Wedge

## 5.1 Introduction

In the previous chapter a special scattering algorithm, based upon the approximation of singular fields with a static field distribution, has been introduced. The introduction of such a corner node into the TLM scheme has proved to be very effective for the reduction of the coarseness error associated with the presence of sharp metallic edges. However, the inclusion in the algorithm of *a priori* information of a static field configuration is achieved by altering the standard scattering TLM process. The hybrid scheme (standard TLM plus corner node) does not retain the TLM property of unconditional stability, and long term instabilities have been experienced in the simulation of some structures.

The analysis of stability of complex time marching algorithms is a cumbersome task, and the effect of any change in the update equations very difficult to predict. A much more efficient and secure way to proceed is to introduce modifications for which stability is intrinsically guaranteed. This is the case for example with circuit based techniques. Any alteration of the TLM algorithm, based on passive linear circuit models, is guaranteed to produce an unconditionally stable scheme.

A circuit-based approach is attractive for three reasons. Firstly, the stability of the resulting hybrid scheme is intrinsically guaranteed. Secondly, due to the nature of the TLM method, a corner-node equivalent circuit lends itself to a natural and straightforward implementation within a TLM mesh. Finally, the information derived from the knowledge of a complex field distribution is condensed in a compact model for which

powerful tools of analysis and simplification techniques are largely available.

In this chapter a new approach for the reduction of the coarseness error, based on the quasi-static approximation of Green's functions for an infinite conductive wedge, is explored. The field distribution around a corner is represented in terms of an equivalent circuit which can be implemented easily and efficiently in a TLM mesh. The accuracy of the proposed method is compared to that of the standard TLM algorithm by means of test structures for which the results are also available in the literature.

In section 5.2 the general description of the electric field near a conducting wedge in terms of a Green's function will be given. In section 5.3, Green's function will be simplified with a quasi-static approximation, and used to derive an equivalent circuit for the corner node. Section 5.4 will deal with the embedding of the equivalent circuit into the TLM mesh, and it will concentrate on the derivation of a scattering algorithm for the edge node. Finally, after extension of the procedure to knife edge septa of arbitrary length, in section 5.5, numerical results will be provided in section 5.6. Conclusive considerations and comments will then be presented in section 5.7.

## 5.2 Theoretical Background

Consider an infinite electric line source of electric current I, placed near a conducting wedge with a total inner wedge angle of $2\alpha$, as shown in Figure 5.1. Coordinates $(\rho',\phi')$ indicate the source point, and $(\rho,\phi)$ the point at which the electromagnetic field is calculated. The metallic wedge is uniform along the $z$-direction.

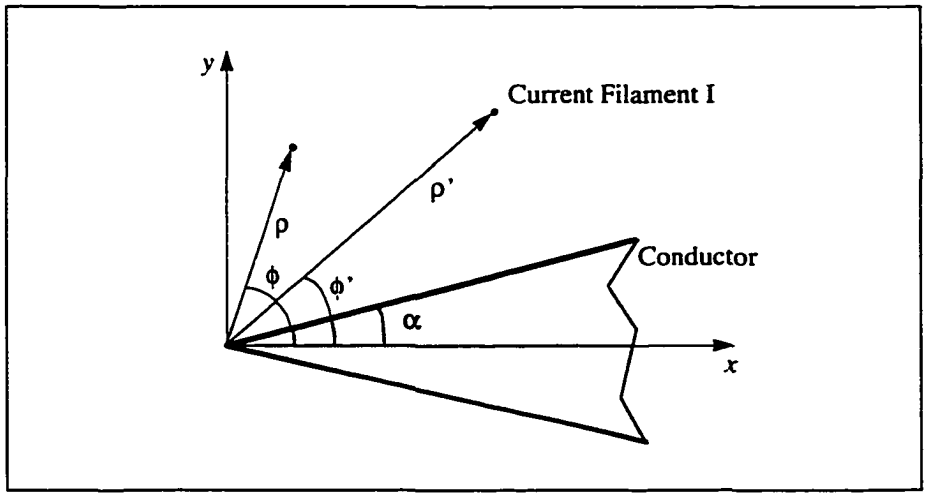


*Figure 5.1 Infinitive conducting wedge geometry.*

The electric field component along the $z$-direction $E_z^t$, can be expressed as the sum of the incident field $E_z^i$, produced everywhere by the source in the absence of the wedge, and the scattered field $E_z^s$. The scattered field must be chosen so that the total field vanishes on the wedge faces, and satisfies reciprocity[1]. The $\phi$ variations must be represented by sinusoidal functions, since in the $\phi$ direction the waves bounce back and forth between the plates forming the wedge. The incident field is the field radiated by an infinite electric line source in free space, evaluated in a cylindrical coordinate system [82]. It can be shown [83] that the total electric field can be written in the following form:

1. The expression must remain the same when source and observation are interchanged.

$$E_z^t = E_z^i + E_z^s = \begin{cases} \sum_{\nu=1}^{\infty} a_\nu H_\nu^{(2)}(k\rho') J_\nu(k\rho) \sin(\nu(\phi-\alpha)) \sin(\nu(\phi'-\alpha)) \\ \qquad \rho < \rho' \\ \sum_{\nu=1}^{\infty} a_\nu H_\nu^{(2)}(k\rho) J_\nu(k\rho') \sin(\nu(\phi-\alpha)) \sin(\nu(\phi'-\alpha)) \\ \qquad \rho > \rho' \end{cases} \tag{5.1}$$

The value of the index $\nu$ is determined by the condition that the electric field must be null at $\phi=2\pi-\alpha$. That is

$$\sin[\nu(\phi-\alpha)]\,|_{\Phi=2\pi-\alpha} = \sin[2\nu(\pi-\alpha)] = 0$$
$$\nu = \frac{n\pi}{2(\pi-\alpha)} \tag{5.2}$$

The coefficient $a_\nu$ depends on the type of source. It can be shown [82] that for an infinite electric line source of electric current I, $a_\nu$ is:

$$a_\nu = \frac{\pi\omega\mu I}{2(\pi-\alpha)} \tag{5.3}$$

Combining (5.1) and (5.3), and isolating the source amplitude, the electric field component $E_z$ in cylindrical coordinates can be expressed in terms of a product of the Green's function of the problem and the source amplitude:

$$E_z(\rho,\phi) = G(\rho,\phi;\rho',\phi')\, I \tag{5.4}$$

$$G(\rho,\phi;\rho',\phi') = -\frac{\omega\mu\pi}{2(\pi-\alpha)} \cdot \begin{cases} \sum_{\nu=1}^{\infty} H_\nu^{(2)}(k\rho') J_\nu(k\rho) \sin(\nu(\phi-\alpha)) \sin(\nu(\phi'-\alpha)) \\ \qquad \rho < \rho' \\ \sum_{\nu=1}^{\infty} H_\nu^{(2)}(k\rho) J_\nu(k\rho') \sin(\nu(\phi-\alpha)) \sin(\nu(\phi'-\alpha)) \\ \qquad \rho > \rho' \end{cases} \tag{5.5}$$

In particular, when the angle $\alpha$ is equal to zero we have a so-called knife edge. In this case the expression for the Green's function $G(\rho,\phi;\rho',\phi')$ is given by:

$$G(\rho,\phi;\rho',\phi') = -\frac{\omega\mu}{2}\begin{cases}\sum_{n=1}^{\infty} H_{n/2}^{(2)}(k\rho')\,J_{n/2}(k\rho)\sin(\frac{n}{2}\phi)\sin(\frac{n}{2}\phi') & \rho<\rho' \\ \sum_{n=1}^{\infty} H_{n/2}^{(2)}(k\rho)\,J_{n/2}(k\rho')\sin(\frac{n}{2}\phi)\sin(\frac{n}{2}\phi') & \rho>\rho'\end{cases} \tag{5.6}$$

The expressions (5.5) and (5.6) present a complex frequency dependence, the variable *k* being a function of $\omega$. As seen in the previous chapter, the singular field in the vicinity of the metallic corner is essentially static. It is therefore conceivable to perform a quasi-static approximation (k -> 0) of Green's function. Using approximations for the Bessel and Hankel functions for small values of the argument [84], the following expression can be derived for the factor $J(k\rho')\,H^{(2)}(k\rho)$ present in Green's function:

$$H_{\nu}^{(2)}(k\rho')\,J_{\nu}(k\rho) \rightarrow j\frac{1}{\nu\pi}\left(\frac{\rho}{\rho'}\right)^{\nu} \qquad (k\rightarrow 0) \tag{5.7}$$

Hence, (5.6) can be considerably simplified leading to a quasi-static solution given by:

$$G(\rho,\phi;\rho',\phi') = -j\frac{\omega\mu}{2(\pi-\alpha)}\cdot\begin{cases}\sum_{\nu}\frac{1}{\nu}\left(\frac{\rho}{\rho'}\right)^{\nu}\sin\nu(\phi-\alpha)\sin\nu(\phi'-\alpha) & \\ \qquad\qquad \rho<\rho' & \\ \sum_{\nu}\frac{1}{\nu}\left(\frac{\rho'}{\rho}\right)^{\nu}\sin\nu(\phi-\alpha)\sin\nu(\phi'-\alpha) & \\ \qquad\qquad \rho>\rho' & \end{cases} \tag{5.8}$$

The special case of a knife edge will be considered in the rest of this chapter. For this reason equation (5.8) is reported in the following for this special case ($\alpha = 0$):

$$G(\rho,\phi;\rho',\phi') = -j\frac{\omega\mu}{\pi}\begin{cases}\sum_{n=1}^{\infty}\frac{1}{n}\left(\frac{\rho}{\rho'}\right)^{\frac{n}{2}}\sin\left(\frac{n}{2}\phi\right)\sin\left(\frac{n}{2}\phi'\right) & \rho<\rho' \\ \sum_{n=1}^{\infty}\frac{1}{n}\left(\frac{\rho'}{\rho}\right)^{\frac{n}{2}}\sin\left(\frac{n}{2}\phi\right)\sin\left(\frac{n}{2}\phi'\right) & \rho>\rho'\end{cases} \tag{5.9}$$

# 5.3 Application to the TLM mesh

The quasi-static expression for the electric field described in (5.8) represents the basis for the determination of an equivalent circuit describing the field around the edge. In the following, two different geometries will be taken into consideration: a knife edge ($\alpha = 0°$), and a 90° wedge ($\alpha = 45°$). These are the two most common types of metallic corners encountered in practice.

## 5.3.1 Knife Edge

In order to reduce the number of ports surrounding the edge, the conducting boundaries have been placed on the nodes of the TLM mesh. In this way, only a three-port equivalent circuit is required to characterize the edge behavior for a knife edge, as depicted in Fig. 5.2

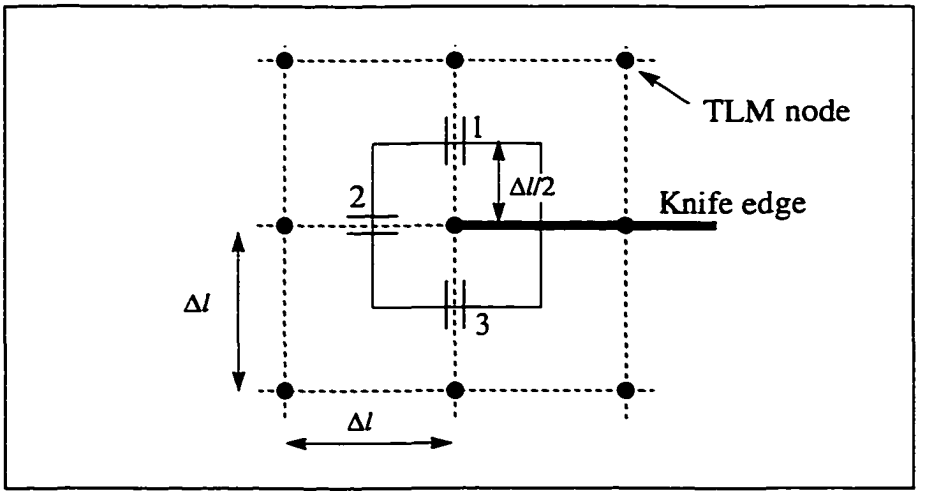


*Figure 5.2 Wedge position in the TLM mesh. Knife edge case.*

Since the voltages and currents at the ports are related to the electric field $E_z$ and to the current density $J_z$, the three-port equivalent circuit can be described by a Z matrix representation. For each port of the circuit we may define[1]:

$$V_i \rightarrow E_z(\rho_i, \phi_i)$$
$$I_i \rightarrow -J_z(\rho_i, \phi_i) = -\frac{I(\rho_i, \phi_i)}{2\pi\rho_i} = -\frac{I(\rho_i, \phi_i)}{\pi\Delta l} \quad ; \qquad \rho_i = \frac{\Delta l}{2} \quad ; \quad \phi_i = i\frac{\pi}{2} \tag{5.10}$$

where *i* indicates the number of the port in the circuit. Each element of the impedance matrix is defined as:

$$Z_{ij} = \left.\frac{V_i}{I_j}\right|_{I_{k\neq j}=0} \tag{5.11}$$

It is clear that the elements of the matrix depend only on the Green's function (5.9). A new Green's function $\overline{G}(\rho, \phi; \rho', \phi')$, proportional to $G(\rho, \phi; \rho', \phi')$ is defined:

$$Z_{ij} = -\pi\Delta l G(\rho_i, \phi_i; \rho'_j, \phi'_j) = \overline{G}(\rho_i, \phi_i; \rho'_j, \phi'_j) \tag{5.12}$$

Due to the reciprocity property of Green's function, the three-port circuit will have a symmetric impedance matrix. Moreover, because of the geometrical symmetries, the number of independent elements is reduced to only four, with the impedance matrix having the following general form:

$$[Z] = \begin{bmatrix} z_{11} & z_{12} & z_{13} \\ z_{12} & z_{22} & z_{12} \\ z_{13} & z_{12} & z_{11} \end{bmatrix} \tag{5.13}$$

---

1. $J_z$ has the dimension of [A/m]. It is the current density of a current source of amplitude I distributed over a circumference of radius $\rho$ [82].

The non-diagonal elements are easily determined after some manipulations and the use of tables for the sums of series containing trigonometrical functions as argument. The value of the diagonal terms $Z_{ii}$, corresponding to the evaluation of Green's function when source and field points are coincident, are singular. To determine a finite value for these impedances, a first rough, approximation may be constructed by considering the source point and the field point in slightly different positions. In particular, it can be assumed that the radii $\rho$ and $\rho'$ are not equal. Defining a parameter $x$ indicating the ratio between $\rho'$ and $\rho$, an expression for the diagonal elements can be obtained as a function of $x$. These expressions must lead to a singular function when evaluated for $x = 1$. A detailed derivation of the impedance elements is reported in Appendix A. The matrix Z obtained with this pointform evaluation of Green's function becomes:

$$[Z] = j\frac{\omega\mu}{\pi}\begin{bmatrix} L_{11} & L_{12} & L_{13} \\ L_{12} & L_{22} & L_{12} \\ L_{13} & L_{12} & L_{11} \end{bmatrix} = j\omega[L] \tag{5.14}$$

where the value of the inductive elements is given by:

$$L_{11} = \frac{\pi\Delta l}{4}\log\left[\frac{1+x^2}{(1-x)^2}\right] \qquad L_{12} = \frac{\pi\Delta l}{2}\log\left[\frac{\sin\frac{3\pi}{8}}{\sin\frac{\pi}{8}}\right]$$
$$L_{13} = \frac{\pi\Delta l}{4}\log(2) \qquad L_{22} = \frac{\pi\Delta l}{2}\log\left[\frac{1+x}{1-x}\right] \tag{5.15}$$

As anticipated, when source and field points are coincident ($\rho=\rho'$ and therefore $x=1$), the diagonal terms $L_{ii}$ become infinite.

The pulses traveling along the TLM lines represent the field distribution over the entire cell, and the electric port associated with the TLM link line is distributed over the cell as well. It is therefore misleading to look at the three ports of Fig. 5.2 as single points in which to evaluate Green's function (5.9). The distributed nature of the ports should therefore be represented by taking into consideration an average value of the Green's function over an appropriate domain of integration. This averaging will also

eliminate the convergence problem for the diagonal terms. A more general definition for the impedances would then be:

$$Z_{ij} = \frac{1}{W_i W_j} \int_{W_i} \int_{W_j} \overline{G}(s;s_0)\, ds ds_0 \tag{5.16}$$

where $\overline{G}(s;s_0)$ represents Green's function determined in (5.12), and $W_i,W_j$ are the domains of integration for the source variables and for the field variables [85-86]. Three distinct domains of integration have been taken in account, leading to different formulations for the impedance elements. The case of pointform integration - Figure 5.3(a) - has been already analyzed and the resulting impedance matrix has been reported in the expressions (5.14) - (5.15).

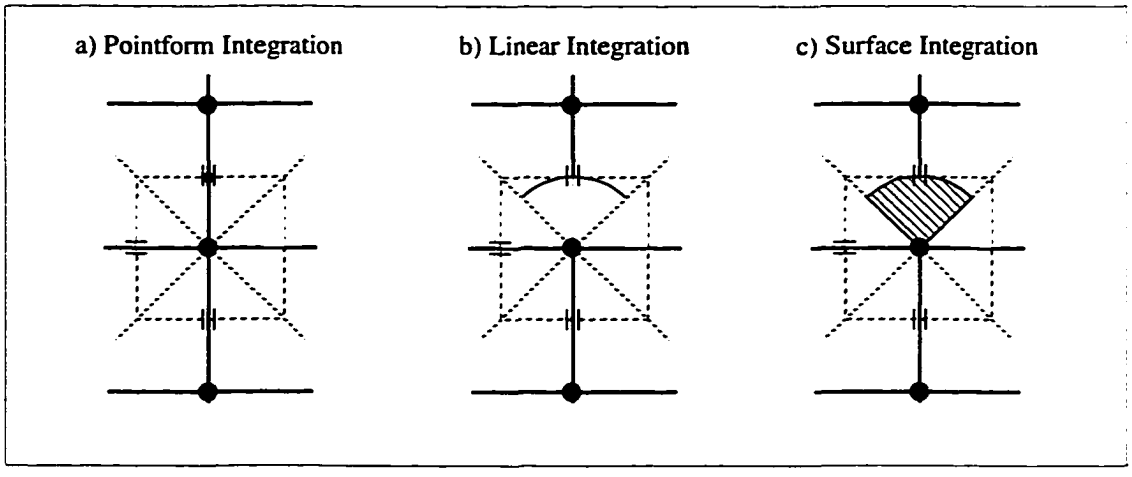


*Figure 5.3 Domains of integration for $Z_{ij}$*

The linear integration of Figure 5.3 (b) performs an average of the impedance Green's function over a curve of a quarter of circumference tangent to the TLM cubic face. The surface integration of Figure 5.3 (c) performs an average of the impedance Green's function over a surface of a circular sector approximating the surface quarter of a TLM cell. We expect that the surface integration will yield the best results in terms of reduction of coarseness error, since it accounts best for the energy stored around the corner.

Expression (5.16) has been evaluated for both the linear and surface integrations,

and has given rapidly convergent results for all the elements of the matrix. The expressions for the linear and surface case are shown respectively in (5.17) and (5.18).

$$L_{ij} = \frac{64\Delta l}{\pi} \sum_{n=1}^{\infty} \frac{1}{n^3} \sin\left(\frac{n}{2}\varphi_i\right) \sin\left(\frac{n}{2}\varphi_j\right) \left[\sin\left(\frac{n\pi}{8}\right)\right]^2 \tag{5.17}$$

$$L_{ij} = \frac{16^2\Delta l}{\pi} \sum_{n=1}^{\infty} \frac{1}{n^3(4+n)} \sin\left(\frac{n}{2}\varphi_i\right) \sin\left(\frac{n}{2}\varphi_j\right) \left[\sin\left(\frac{n\pi}{8}\right)\right]^2 \tag{5.18}$$

The detailed derivation of the previous expressions is reported in Appendix B.

## 5.3.2 Ninety-degree wedge

The same derivation can be repeated, *mutatis mutandis*, for a ninety-degree corner ($\alpha=\pi/4$). The geometry of the wedge, and its position in a TLM mesh are shown in Figure 5.4. In this case only a two-port circuit is necessary to model the corner node. The Green's function (5.8), reduced to the case of a ninety-degree corner, is reported in (5.19). Due to the reciprocity of the function, and by virtue of the geometrical symmetry of the problem, only two distinct matrix elements $z_{ij}$ need to be determined.

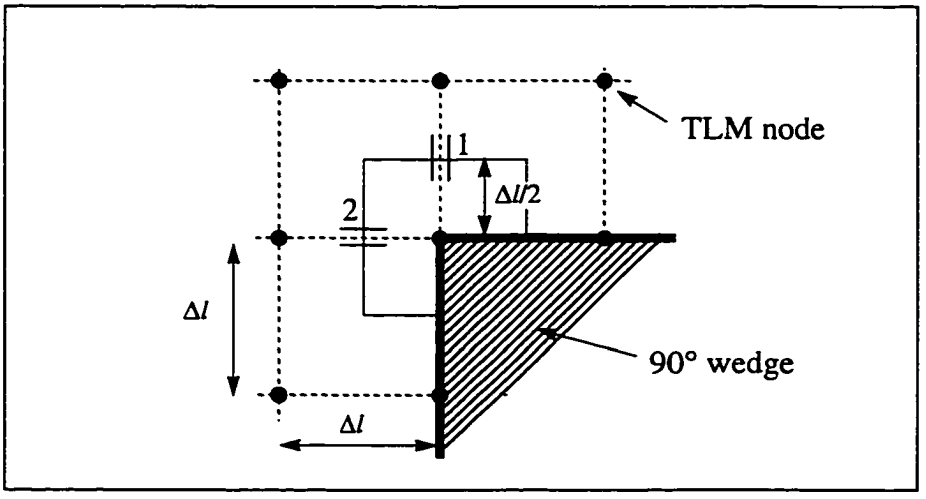


*Figure 5.4 Wedge position in the TLM mesh. 90° case.*

$$G(\rho,\phi;\rho',\phi') = -j\frac{\omega\mu}{\pi}\cdot\begin{cases}\displaystyle\sum_{n=1}^{\infty}\frac{1}{n}\left(\frac{\rho}{\rho'}\right)^{\frac{2n}{3}}\sin\left[\frac{2n}{3}\left(\phi-\frac{\pi}{4}\right)\right]\sin\left[\frac{2n}{3}\left(\phi'-\frac{\pi}{4}\right)\right] & \rho<\rho' \\ \displaystyle\sum_{n=1}^{\infty}\frac{1}{n}\left(\frac{\rho'}{\rho}\right)^{\frac{2n}{3}}\sin\left[\frac{2n}{3}\left(\phi-\frac{\pi}{4}\right)\right]\sin\left[\frac{2n}{3}\left(\phi'-\frac{\pi}{4}\right)\right] & \rho>\rho'\end{cases} \tag{5.19}$$

The impedance matrix will therefore have the following general form:

$$[Z] = \begin{bmatrix} z_{11} & z_{12} \\ z_{12} & z_{11} \end{bmatrix} \tag{5.20}$$

The non-diagonal elements are easily determined after some manipulations and the use of tables for the sum of series containing trigonometrical functions as argument. The value of the diagonal term $Z_{ii}$, corresponding to the evaluation of Green's function when source and field points are coincident, is singular. In order to remove this singularity, the averaging (5.16), with a domain of integration as shown in Figure 5.5, has been considered. The matrix Z becomes:

$$[Z] = j\frac{\omega\mu}{\pi}\begin{bmatrix} L_{11} & L_{12} \\ L_{12} & L_{11} \end{bmatrix} = j\omega[L] \tag{5.21}$$

where the value of the inductive elements is given by:

$$L_{ij} = \frac{108\Delta l}{\pi}\sum_{n=1}^{\infty}\frac{1}{n^3(3+n)}\sin\left(\frac{2n}{3}\varphi_i\right)\sin\left(\frac{2n}{3}\varphi_j\right)\left[\sin\left(\frac{n\pi}{6}\right)\right]^2 \qquad i,j=1,2 \tag{5.22}$$

The detailed derivation of the previous expression is reported in Appendix C.

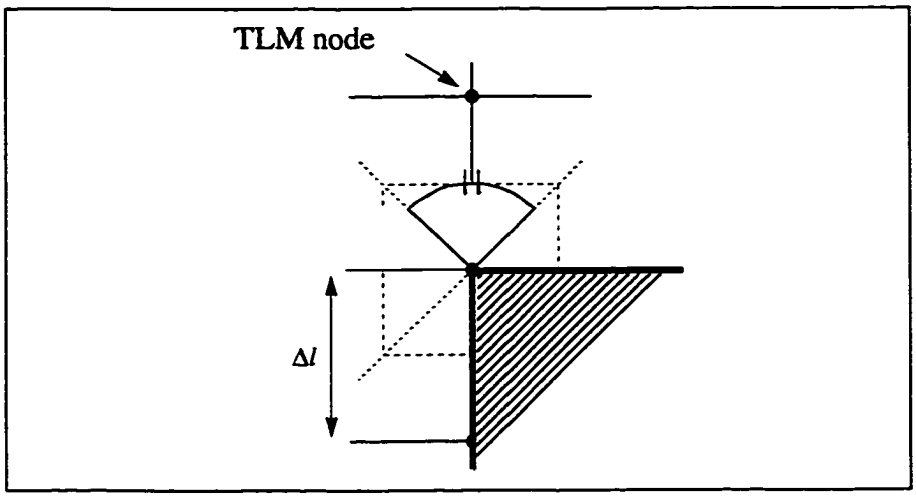


*Figure 5.5 Domain of integration for the determination of $Z_{ij}$, 90° corner*

### 5.3.3 Circuit topology

A circuit topology can be derived from the impedance matrices (5.14) and (5.21), using canonical realization techniques [87]. The procedure is described in the following only for the most complex case of a three-port circuit. The simpler case of the ninety-degree corner can be derived similarly.

$$[Y] = \begin{bmatrix} y_{11} & y_{12} & y_{13} \\ y_{12} & y_{22} & y_{12} \\ y_{13} & y_{12} & y_{11} \end{bmatrix} = [Y_1] + [Y_2] + [Y_3] + [Y_4]$$

$$[Y_1] = \begin{bmatrix} y_{11} - \left(\frac{y_{12}+y_{13}}{n}\right) & 0 & 0 \\ 0 & y_{22} - y_{12}\left(n + \frac{1}{n}\right) & 0 \\ 0 & 0 & y_{11} - \left(\frac{y_{12}+y_{13}}{n}\right) \end{bmatrix} \tag{5.23}$$

$$[Y_2] = \frac{y_{12}}{n}\begin{bmatrix} 1 & -n & 0 \\ -n & n^2 & 0 \\ 0 & 0 & 0 \end{bmatrix} \qquad [Y_3] = \frac{y_{13}}{n}\begin{bmatrix} 1 & 0 & -n \\ 0 & 0 & 0 \\ -n & 0 & n^2 \end{bmatrix} \qquad [Y_4] = \frac{y_{12}}{n}\begin{bmatrix} 0 & 0 & 0 \\ 0 & 1 & -n \\ 0 & -n & n^2 \end{bmatrix}$$

The generic impedance matrix [Y] can be expressed as the sum of four different matrices as shown in (5.23). Each of the four building blocks represents the admittance matrix of a simple three-port circuit, as depicted in Figure 5.6.

The sum of admittance matrices corresponds to a parallel connection. Therefore the overall equivalent circuit for the three-port element is composed of a shunt connection of the four building blocks. The extra degree of freedom given by the transformer ratio 'n' can be chosen arbitrarily so that the admittances $Y_1^1$ , $Y_1^2$ , $Y_1^3$ are physically realizable.

As an example, the shunt connection of the four blocks is shown in Figure 5.7 only for port three, since it is similar for the other two ports.

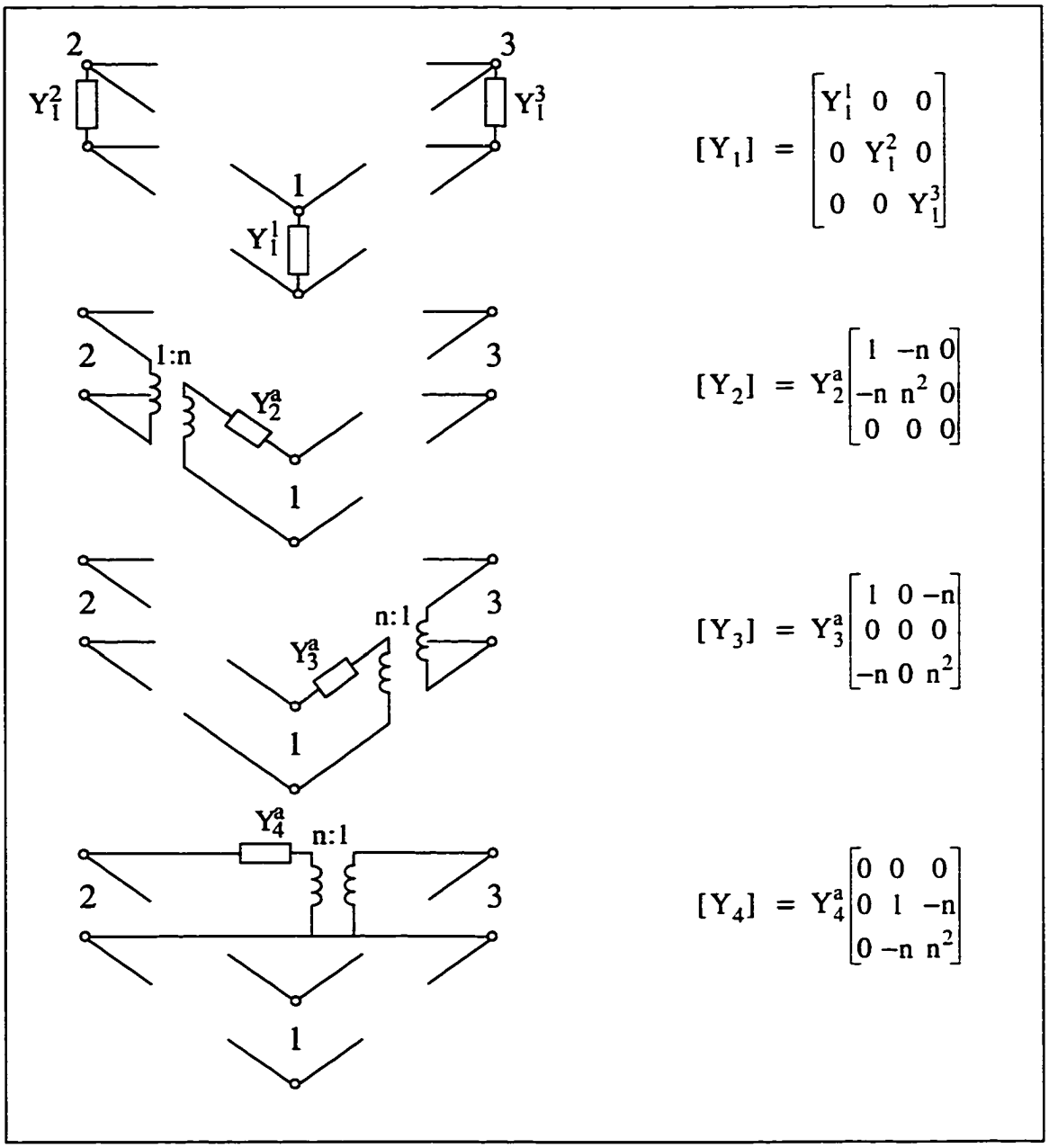


*Figure 5.6 Topologies for each of the elementary admittance matrices*

$$Y_1^1 = y_{11} - \left(\frac{y_{12}+y_{13}}{n}\right) \qquad Y_1^2 = y_{22} - y_{12}\left(n + \frac{1}{n}\right) \qquad Y_1^3 = y_{11} - \left(\frac{y_{12}+y_{13}}{n}\right)$$

$$Y_2^a = \frac{y_{12}}{n} \qquad Y_3^a = \frac{y_{13}}{n} \qquad Y_4^a = \frac{y_{12}}{n} \tag{5.24}$$

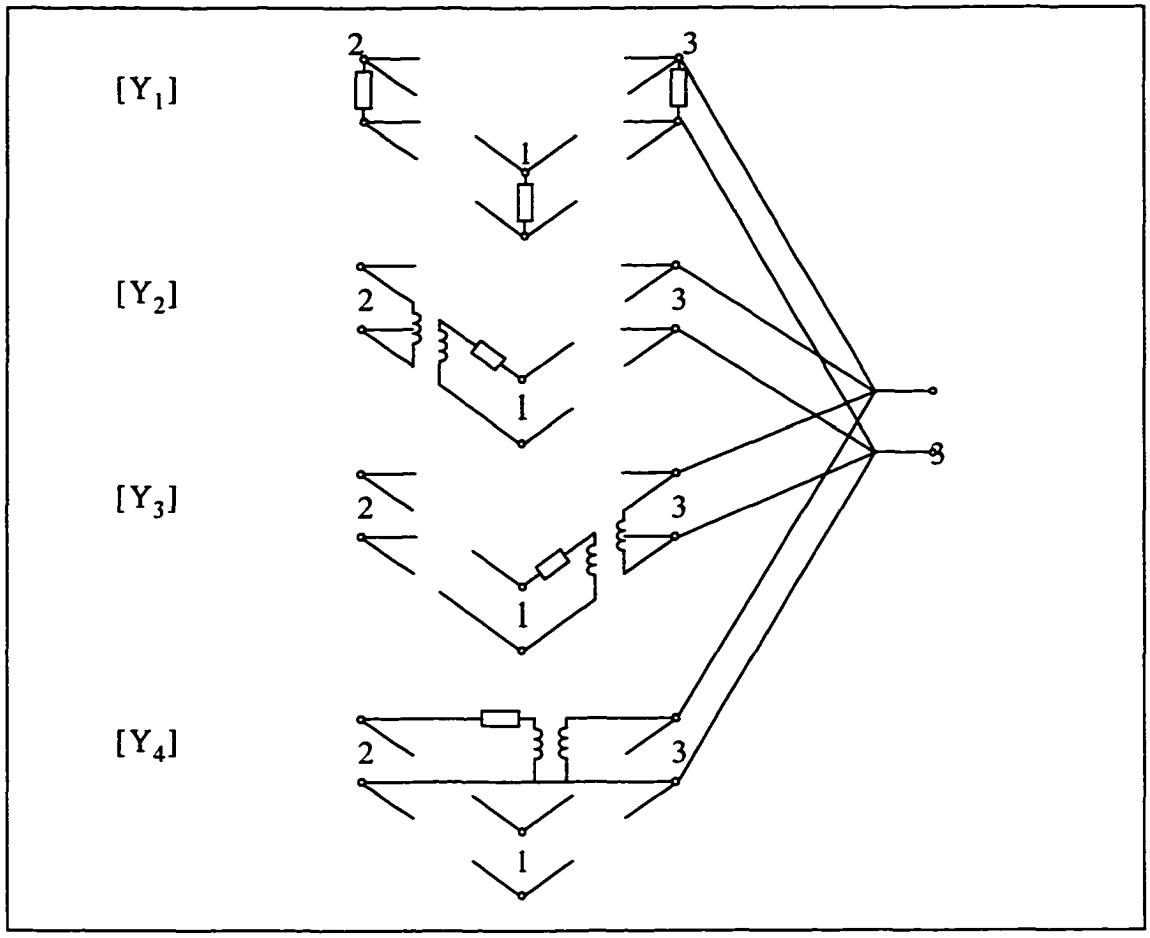


*Figure 5.7 Shunt connection of the four building blocks. Only the connection for the port three is shown.*

The whole simplified circuit obtained from the shunt connection is depicted in Figure 5.8. All the admittances in the circuit are purely reactive, in particular they are inductances whose value is a function of the elements $L_{ij}$ in (5.14). The admittance matrix [Y] obtained as the inversion of [Z] is given in equation (5.25). The substitution of equation (5.25) in the expression (5.24) gives finally the value of the equivalent circuit parameter as a function of the impedance elements $L_{ij}$.

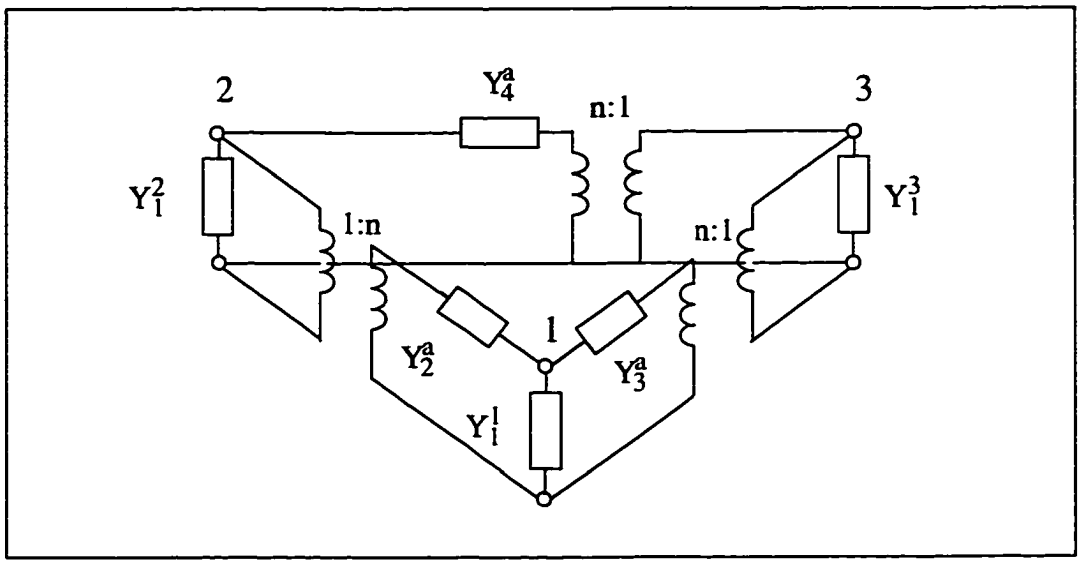


*Figure 5.8 Equivalent corner-node circuit for the knife edge case*

$$[Y] = [Z]^{-1} = \begin{bmatrix} y_{11} & y_{12} & y_{13} \\ y_{12} & y_{22} & y_{12} \\ y_{13} & y_{12} & y_{11} \end{bmatrix}$$

$$[Y] = \frac{1}{j\omega\mu}\frac{\pi}{\Delta}\begin{bmatrix} [L_{22}L_{33} - L_{12}^2] & [L_{12}(L_{13} - L_{33})] & [L_{12}^2 - L_{22}L_{13}] \\ [L_{12}(L_{13} - L_{33})] & [L_{11}L_{33} - L_{13}^2] & [L_{12}(L_{13} - L_{33})] \\ [L_{12}^2 - L_{22}L_{13}] & [L_{12}(L_{13} - L_{33})] & [L_{22}L_{33} - L_{12}^2] \end{bmatrix} \quad (5.25)$$

$$\Delta = L_{11}L_{22}L_{33} - L_{33}L_{12}^2 - L_{22}L_{13}^2 + 2L_{12}^2L_{13} - L_{11}L_{12}^2$$

## 5.4 Discretization process

The equivalent circuit topologies derived for the knife edge and ninety-degree corner are extremely powerful, since complex information has been condensed in a compact, and easily implemented model. From the knowledge of the equivalent circuit for the corner node, a hybrid TLM scheme can be implemented. Such a scheme would con-

sist of a standard TLM network comprising, in the regions of the computational domain where a metallic wedge has to be modeled, the equivalent circuits previously derived. An example of such a network is depicted in Figure 5.9. TLM nodes and equivalent circuit communicate by means of the voltage pulses incident from the TLM network upon the circuit, and scattered from the circuit back into the TLM mesh. Therefore, in order to implement the hybrid scheme, we need to determine the relation between the incident and reflected voltages at the ports as a function of the Z-matrix elements.

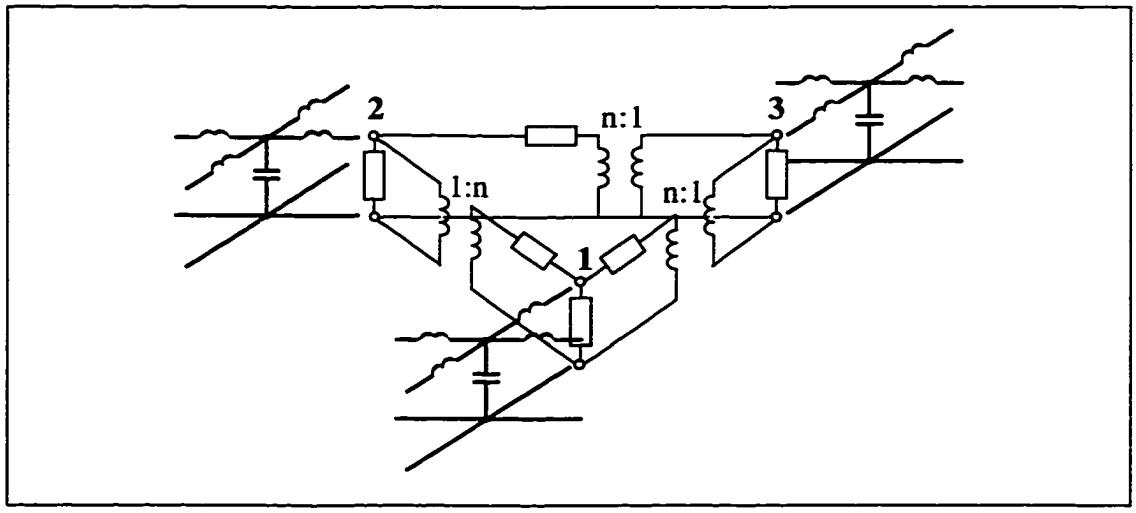


*Figure 5.9 Embedding of the equivalent corner-node circuit in the TLM mesh*

A very easy and compact way to derive such a relation is to use the matrix representation of the equivalent circuit, as in (5.14) and (5.21). The circuit is therefore modeled as a three-port (two-port for the ninety-degree corner) network, whose impedance matrix is given. This representation, conceptually equivalent to that of Figure 5.9, is shown in Figure 5.10.

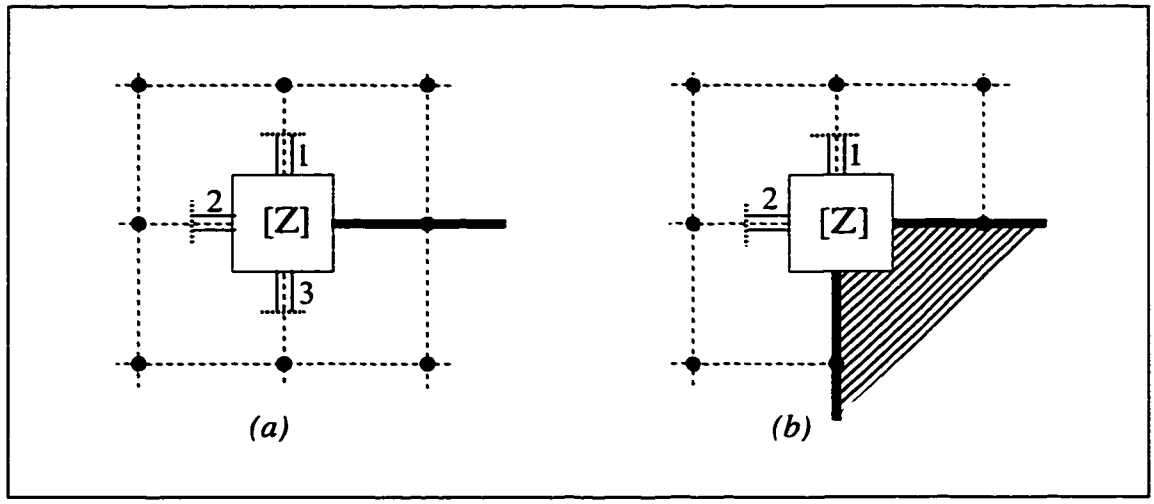


*Figure 5.10 Corner node modeled with an impedance matrix. (a) Knife edge case, three-port circuit. (b) ninety-degree wedge, two-port circuit*

Due to the quasi-static approximation, the voltages at the ports of the equivalent circuits depend only linearly on the frequency:

$$V = j\omega [L] I; \qquad \mathbf{V} = \begin{bmatrix} V_1 \\ \vdots \\ V_{n\text{-ports}} \end{bmatrix}; \qquad \mathbf{I} = \begin{bmatrix} I_1 \\ \vdots \\ I_{n\text{-ports}} \end{bmatrix} \tag{5.26}$$

The vectors V and I can be expressed in terms of the incident and reflected TLM voltages at the edge, $\mathbf{V}^i$ and $\mathbf{V}^r$, according to the relation:

$$\mathbf{V} = \mathbf{V}^i + \mathbf{V}^r \qquad \mathbf{I} = Y_0 (\mathbf{V}^i - \mathbf{V}^r) \tag{5.27}$$

where $Y_0$ is the TLM link line admittance.

The frequency dependance jω is discretized using a bilinear transformation [88]. This scheme guarantees the stability of the discretized model. The frequency distortion introduced is irrelevant for frequencies propagating with low dispersion error in the TLM mesh ($\lambda \geq 10 \cdot \Delta l$). Hence:

$$j\omega \approx j\frac{2}{\Delta t}\tan\left(\frac{\omega\Delta t}{2}\right) = \frac{2}{\Delta t}\left(\frac{1-e^{-j\omega\Delta t}}{1+e^{-j\omega\Delta t}}\right)$$
$$A_k e^{-j\omega\Delta t} = A_{k-1} \tag{5.28}$$

Substituting relations (5.27) and (5.28) in equation (5.26), a recursive formulation (5.29) characterizing the corner condition in the TLM process is obtained.

$$\mathbf{V}_k^r = \left(\frac{2}{\Delta t}Y_0[L] - [I]\right)\left(\frac{2}{\Delta t}Y_0[L] + [I]\right)^{-1}\left(\mathbf{V}_k^i + \mathbf{V}_{k-1}^r\right) - \mathbf{V}_{k-1}^i \tag{5.29}$$

In this expression $Y_0$ is the TLM link line admittance, and $\mathbf{V}_k^r$ and $\mathbf{V}_k^i$ are the vectors of the voltages incident and reflected at the terminals of the equivalent circuit at the time step $k$. The matrix [I] represents the identity matrix.

Expression (5.29) states that the voltages reflected from the circuit modeling the edge depend simply on the incoming voltages and on the incident and reflected voltages at the previous time step. This implementation of the equivalent circuit in the TLM algorithm is extremely effective and requires that only a few extra values be stored at each time-step.

## 5.5 Generalization to knife edge septa of arbitrary length

So far, we have restricted our study to metallic wedges in which the vertex coincided with a TLM node. A useful extension of the theory described above is the characterization of infinitely thin septa, the vertex of which is placed anywhere between the nodes of TLM mesh. This would allow to use a relatively coarse mesh and still accurately describe septa slightly longer or shorter than an integer number of $\Delta l$.

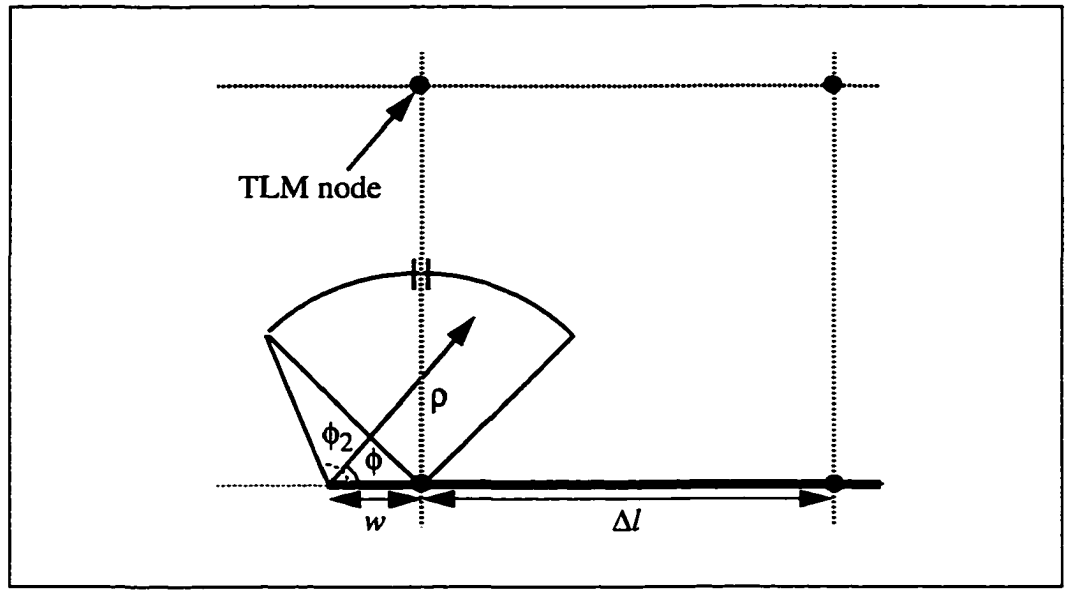


*Figure 5.11 Position of the knife edge septum of arbitrary length in the TLM mesh*

The theory exposed for the description of the knife edge discontinuity is still valid; in particular the expression for the Green's function (5.8) remains the same, once the coordinate system $(\rho,\phi)$ is centered on the corner of the septum. The field at the corner is modeled with a three-port equivalent circuit, since the metallic septum is placed on the nodes of the TLM mesh.

To determine the Z-elements describing the circuit, Green's function must be integrated over a circular sector, for both the source and the field points. See Figure 5.11 for the description of the domain of integration. As an example, the expression for $Z_{11}$ is shown in eq. (5.30).

$$Z_{11} = \frac{1}{W_1^2}\int_0^{\phi_2} d\phi \int_0^{\phi_2} d\phi' \int_{\rho_1(\phi)}^{\rho_2(\phi)} \rho d\rho \int_{\rho'_1(\phi')}^{\rho'_2(\phi')} \bar{G}(\rho,\phi;\rho',\phi')\,\rho' d\rho' \qquad (5.30)$$

The evaluation of this kind of integral is particularly cumbersome, since the integrand is a series (5.8) and its argument is not uniquely defined over the domain of integration (depending on the ratio $\rho/\rho'$); moreover, since the center of the coordinate

system is shifted with respect to the vertex of the circular sector, the domain of integration is not easily described. For these reasons, even a numerical evaluation of the integrals with an acceptable level of precision has proven to be infeasible.

Due to the difficulty of solving these integrals both analytically and numerically, an approximate solution for the values of the Z-matrix has been found empirically. Defining $w$ as the length of the septum extending beyond the TLM node (Figure 5.11), the approximate expressions for the Z elements are given by:

$$\begin{aligned} z_{11}(s) &= z_{11}(0)\,[-s^2-s+1] & z_{13}(s) &= z_{13}(0)\,[s^2-2s+1] \\ z_{12}(s) &= z_{12}(0)\,[s^2-2s+1] & z_{22}(s) &= z_{22}(0)\,[s^2-2s+1] \end{aligned} \qquad (5.31)$$

$$s = \frac{w}{\Delta l} > 0$$

In these formulas the values $z_{ij}(0)$ refer to the case previously analyzed, where the septum length was equal to an integer number of $\Delta l$ (w=0).

A similar set of expressions has been found also for the case of septa slightly shorter ($w$<0) than an integer number of $\Delta l$:

$$\begin{aligned} z_{11}(s) &= z_{11}(0)\,[-s^2-2s+1] & z_{13}(s) &= z_{13}(0)\,[s^2-s+1] \\ z_{12}(s) &= z_{12}(0)\,[s^2-s+1] & z_{22}(s) &= z_{22}(0)\,[s^2-\sqrt{2}s+1] \end{aligned} \qquad (5.32)$$

$$s = \frac{w}{\Delta l} < 0$$

These approximations give good results for values of $|s| \leq 0.35$. This restricted range does not represent a serious limitation; in fact, for most of the practical applications this condition can be easily verified with the choice of a relatively coarse mesh. On the other hand, expressions (5.31) and (5.32) allow treatment of perturbations of the septum length that are small, compared to the mesh size; these would otherwise require very fine discretizations to exactly describe the geometry.

# 5.6 Numerical results

## 5.6.1 Knife edge corner

A first validation of the method has been performed by evaluating the first resonant frequency of a 2D septum-coupled cavity (Figure 5.12). Three different equivalent circuits, obtained from pointform, linear and surface averaging of Green's function respectively, have been implemented. An accurate value (reference line) for the resonant frequency of the cavity has been extracted by Richardson extrapolation of TLM data for increasingly fine discretization (Figure 5.13).

The best results have been obtained with surface integration (5.18); they lead to a much faster convergence to the accurate values than those obtained with the basic 2D-TLM algorithm. With surface integration a better description of the energy stored within the singular region is achieved, therefore it performs better than the linear integration and the pointform evaluation of Green's function. For this reason only surface integration has been implemented in the simulations described further in this section.

It is important to note that, even with a coarse mesh ($\Delta l$=1 mm), the surface corner correction yields an improvement in the accuracy, reducing the percentage error from more than 2% to 0.6%. If an accuracy of 0.1% is required, the corner correction allows to use a cell size at least four times larger than that necessary with the standard TLM.

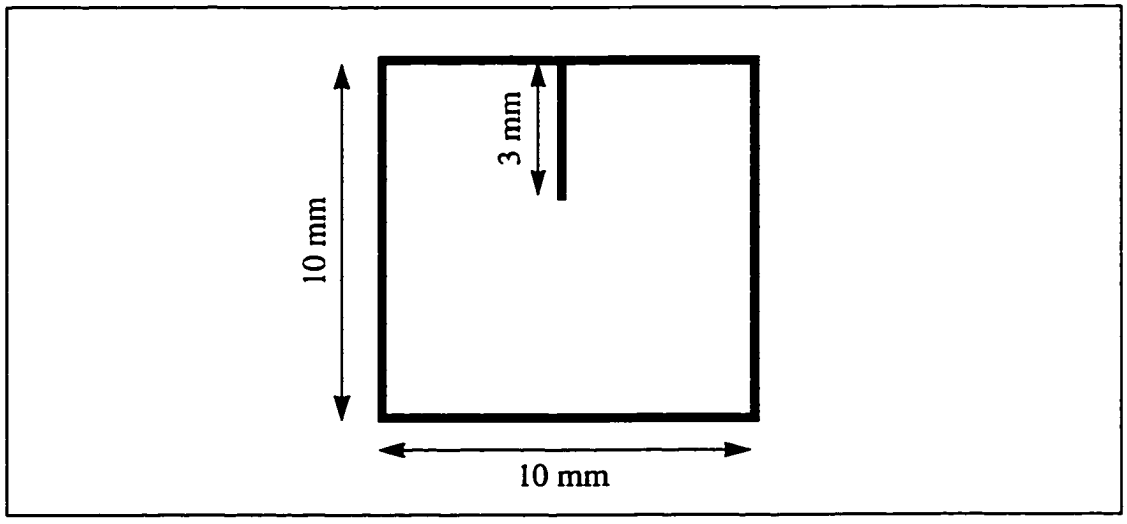


*Figure 5.12 Septum-coupled cavity*

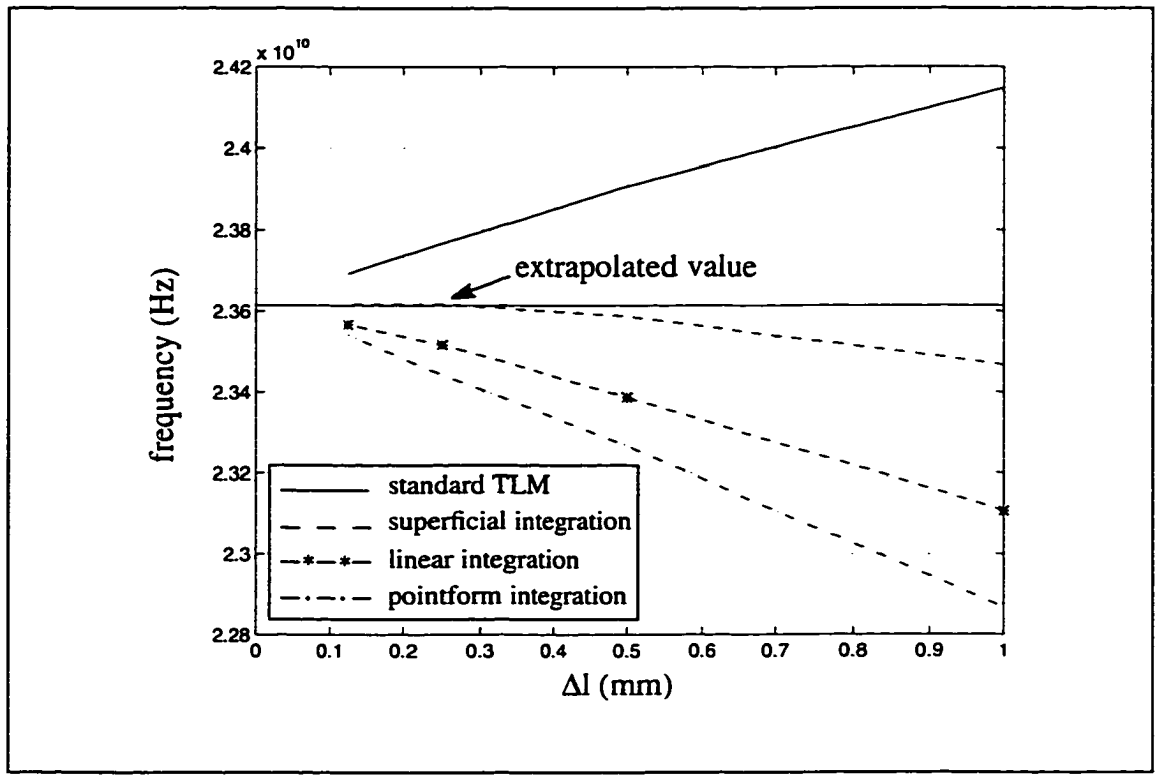


*Figure 5.13 Comparison between the first resonant frequencies obtained with the standard TLM*

The proposed method has been also applied to the analysis of discontinuities in the transverse section of a rectangular waveguide (Figure 5.14). To validate the model of a knife edge, a symmetrical inductive iris with aperture $d$=3.556 mm ($a/2$) in a WR(28) waveguide has been analyzed both with the corner modification and the regular TLM algorithm, and the results have been compared with Marcuvitz's [89] formulae. The scattering parameters obtained for different discretizations are shown in Figure 5.15-a. Note that the corner modification improves considerably the accuracy of the TLM algorithm (Figure 5.15-b) even when a very coarse mesh is used.

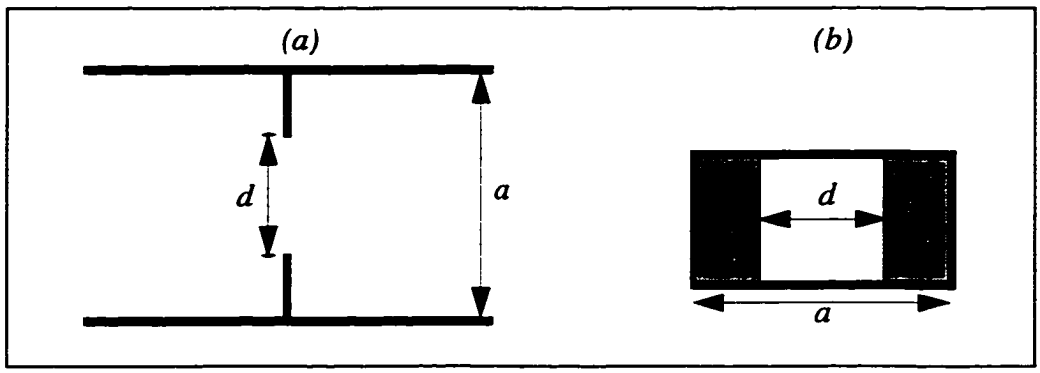


*Figure 5.14 Inductive irises in WR(28) waveguide: a) Top view b) Front view*

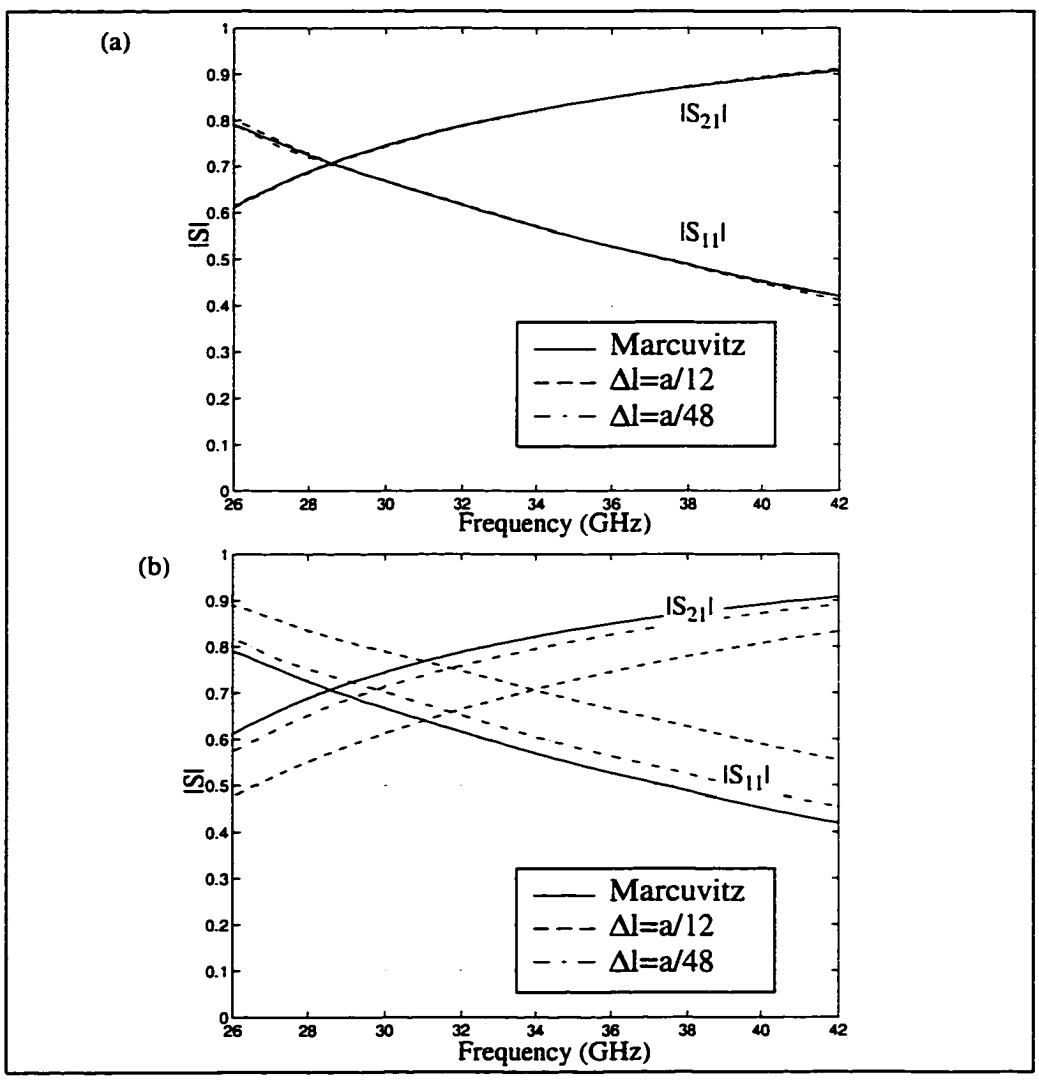


*Figure 5.15 S-parameters for the thin iris in WR(28) waveguide: a) TLM with corner correction, b) TLM without corner correction*

To further test the efficiency of the proposed method, an iris-coupled waveguide bandpass filter (Figure 5.16), with center frequency of 33.18 GHz and bandwidth of 0.94 GHz, has been analyzed. Also in this case, the corner correction results in a much faster convergence to Marcuvitz's curves as compared with the standard TLM algorithm (Figure 5.17 and Figure 5.18).

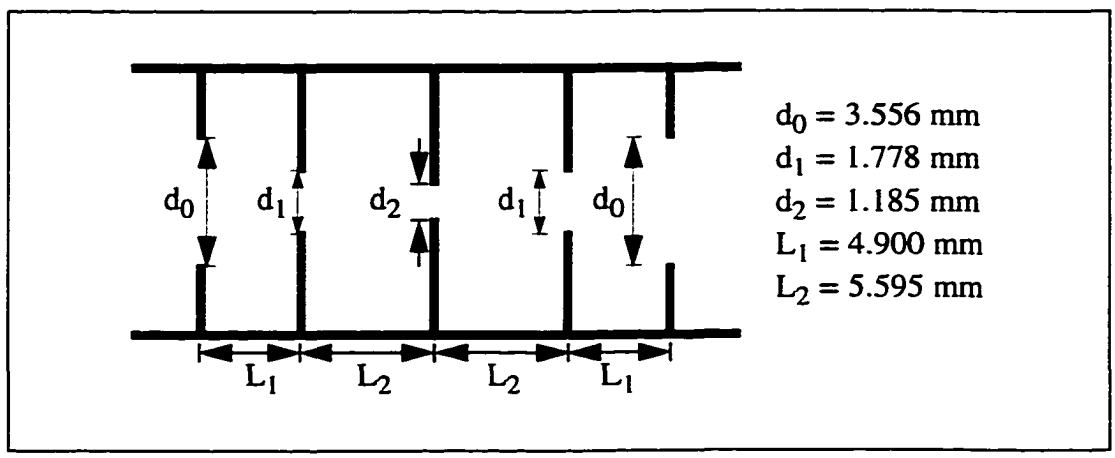


*Figure 5.16 Top view of the iris coupled bandpass filter in WR(28) waveguide*

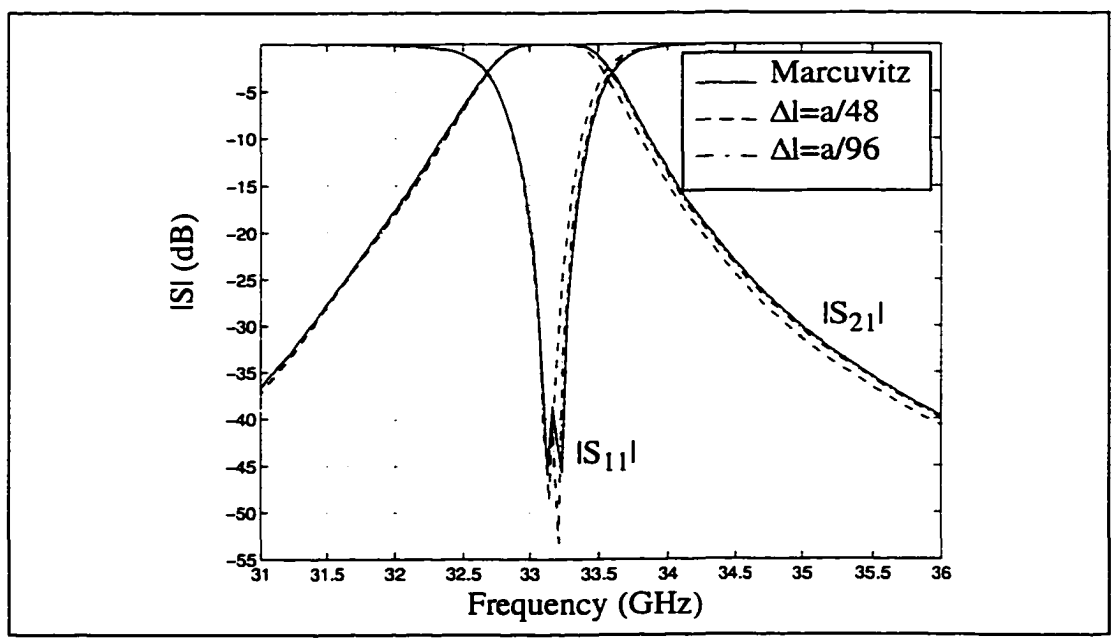


*Figure 5.17 Iris coupled bandpass filter in WR(28) waveguide: TLM with corner correction*

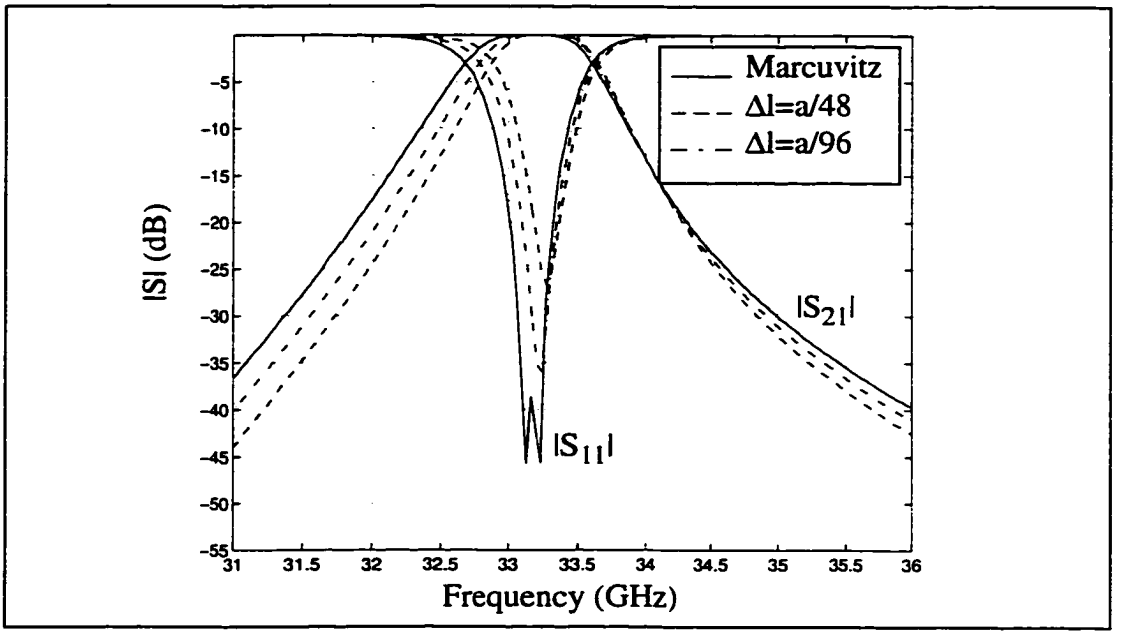


*Figure 5.18 Iris coupled bandpass filter in WR(28) waveguide: TLM without corner correction*

## 5.6.2 Ninety-degree corner

To verify the model of the 90° wedge, a symmetrical iris, of thickness $t$=1.1853 mm ($a/6$) in a WR(28) waveguide has been examined (Figure 5.19). Comparison with the uncorrected TLM algorithm and other techniques has shown that in this case the correction is less effective since, for this kind of discontinuities, the standard TLM method provides good accuracy even with relatively coarse discretizations (Figure 5.20 and Figure 5.21). This agrees with the fact that the field singularity for a ninety-degree edge is not as strong as that of a knife edge. Therefore, the resulting coarseness error is less severe. Other studies have already proved, both empirically [90] or analytically [74], the impact of various different edge geometries on the accuracy of space discrete methods, providing a validation for the results described in this section.

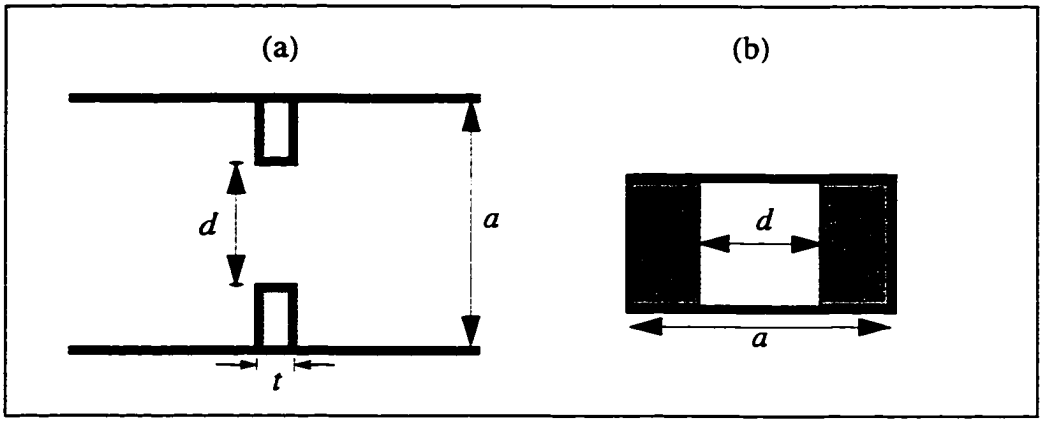


*Figure 5.19 Thick inductive irises in WR(28) waveguide: a) Top view b) Front view*

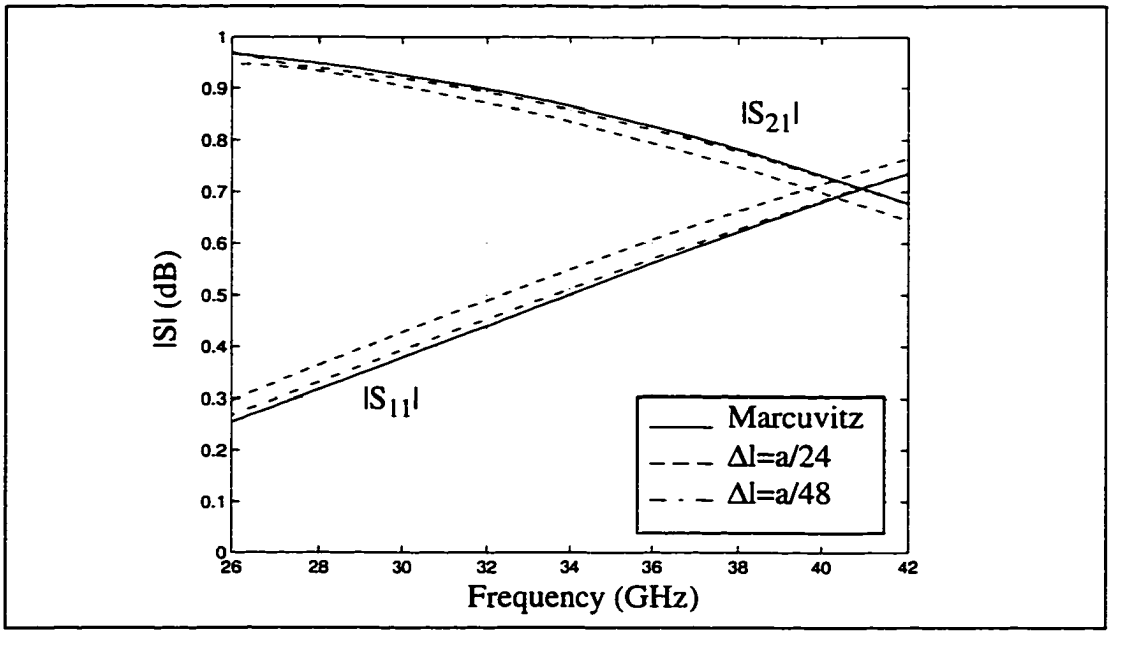


*Figure 5.20 S-parameters for the thick iris in WR(28) waveguide: TLM with corner correction*

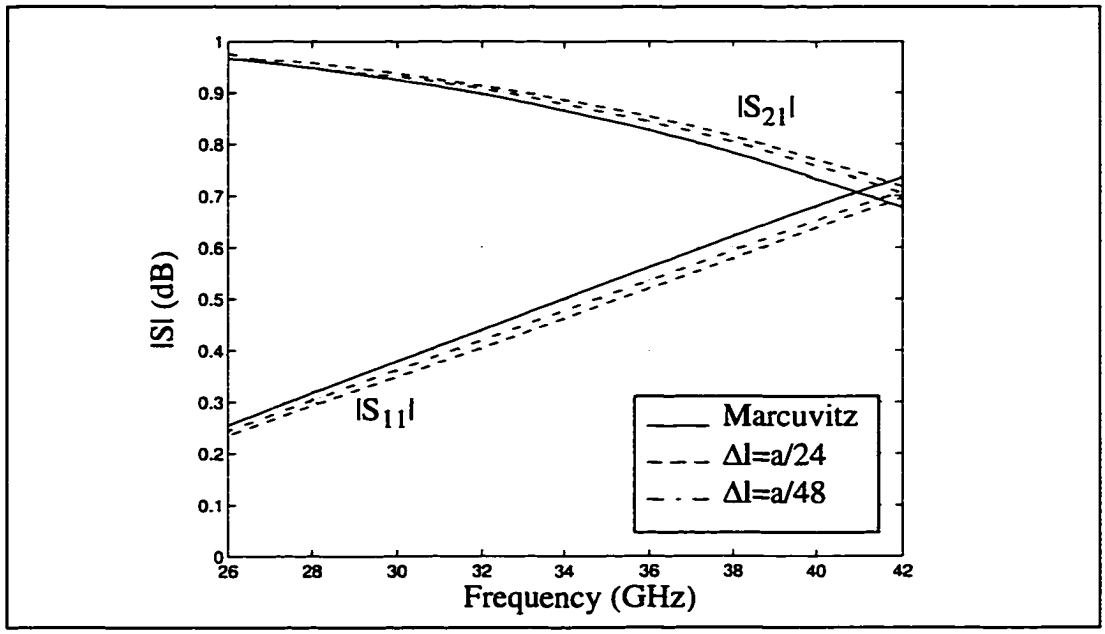


*Figure 5.21 S-parameters for the thick iris in WR(28) waveguide: TLM without corner correction,*

## 5.6.3 Infinitely thin septa of arbitrary length

Finally, the correction for infinitely thin septa of arbitrary length in the TLM mesh has been validated, both for positive and negative variations of the length with respect to an integer number of $\Delta l$. A symmetrical inductive iris with an aperture slightly different from $a/2$ has been analyzed with the corner modification (Figure 5.22), and the results have been compared with Marcuvitz's formulae. In particular, we have discretized the waveguide width with $12\Delta l$, and considered the septum length $l = a/4 \pm s \cdot \Delta l$ (for s= 0.19 and 0.23). We have chosen lengths that, with the standard TLM method, would require a very fine mesh discretization to obtain an exact description.

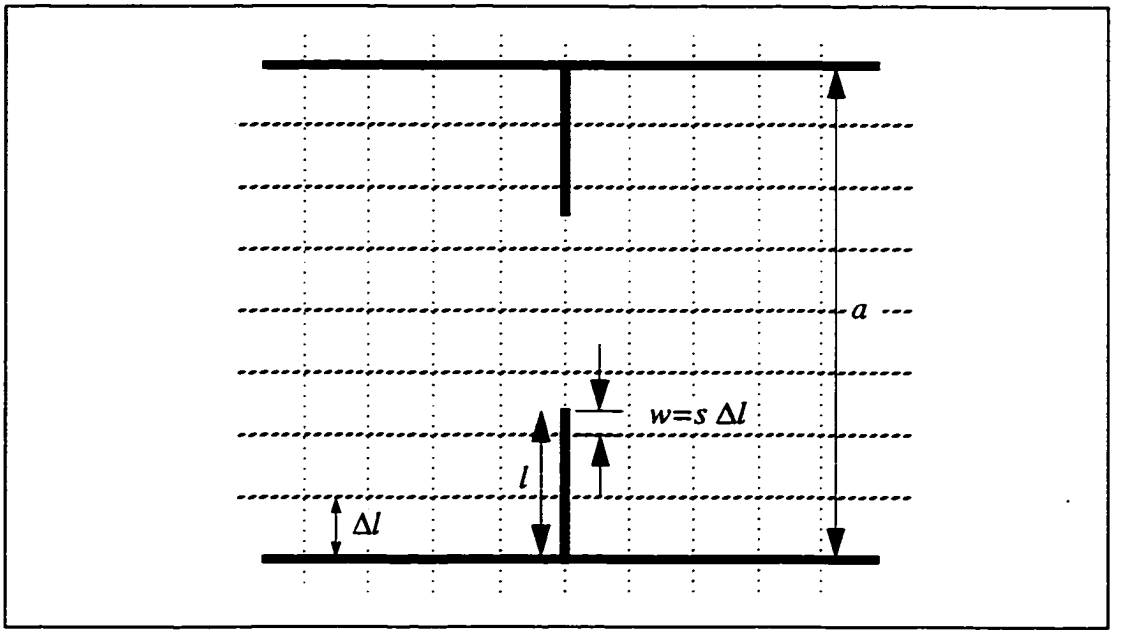


*Figure 5.22 Top view of the thin inductive iris in WR(28) waveguide with septa of arbitrary length l*

The scattering parameters obtained for the two structures are shown in Figure 5.23 and Figure 5.24. From the results we can see that the corner correction is always in good agreement with Marcuvitz's data, even if a coarse discretization is used. From these figures it is also possible to verify that the proposed technique is sensitive to small variations of the length; in fact, the curves obtained with the corner correction for a variation of 0.04 $\Delta l$ (from s = ±0.19 to s = ±0.23) are clearly distinct and in agreement with the theoretical results. To appreciate such a small difference in behavior by using the standard TLM method, we would need a 25 times finer discretization.

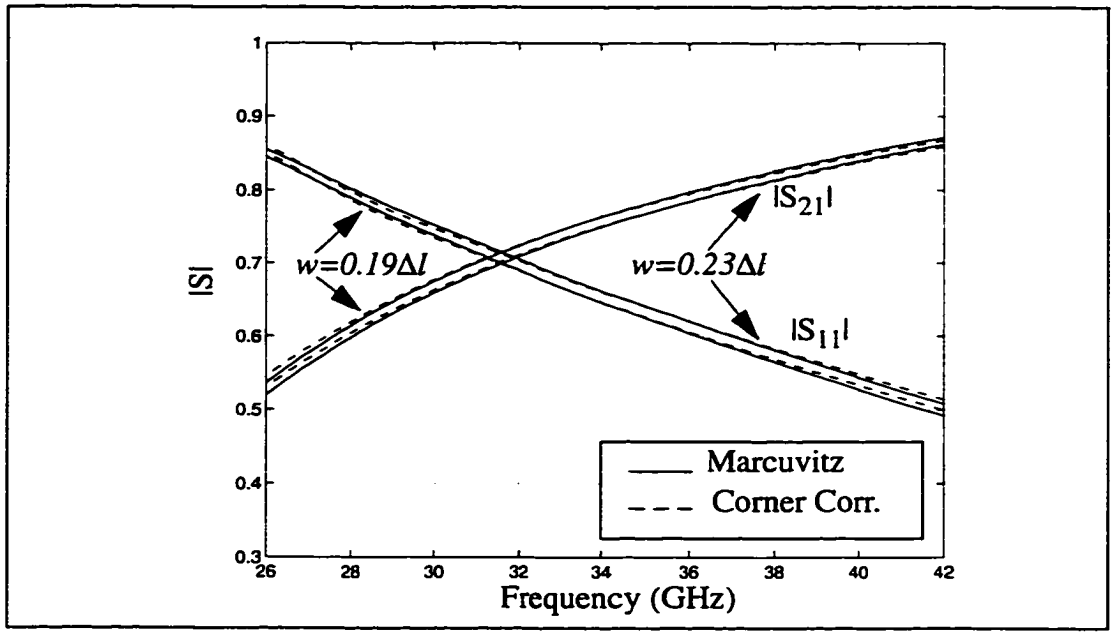


*Figure 5.23 S-parameters of a thin inductive iris in WR(28) waveguide for different lengths of the septa. Discretization: Δl=a/12. w=+ 0.19Δl, + 0.23Δl*

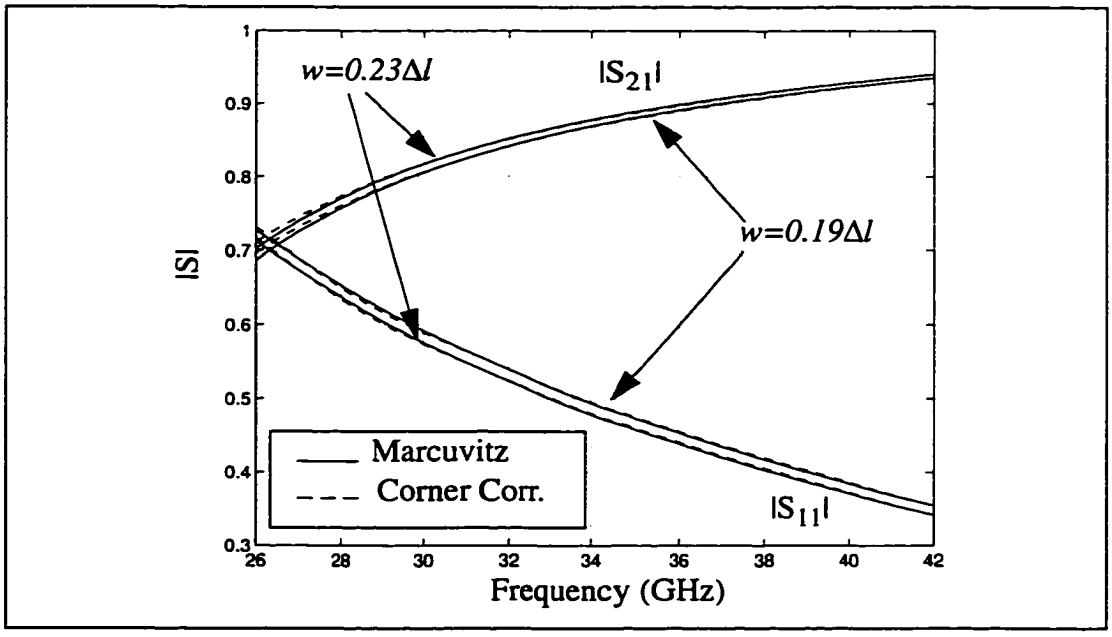


*Figure 5.24 S-parameters of a thin inductive iris in WR(28) waveguide for different lengths of the septa. Discretization: Δl=a/12. w=– 0.19Δl, – 0.23Δl*

## 5.7 Conclusions

In this chapter we have derived an equivalent circuit for knife edges and 90° wedges, based on a quasi-static formulation of the field around the edge. The equivalent circuits have been embedded into the TLM algorithm by means of a newly derived scattering procedure. The resulting hybrid algorithm is guaranteed to be unconditionally stable, since the modification of the TLM scheme is performed on the basis of a passive linear circuit.

The proposed corner correction has been compared with the regular TLM method and with data available in the literature, and has yielded a noticeable improvement in the accuracy as well as in the convergence of the results for knife edges, while in the case of 90° wedges, where less severe field singularities are present, the standard TLM algorithm has proved to be sufficiently accurate.

The better description of the singular behavior of the field around the edge allows considerable savings in computer processing time and memory requirements when compared to mesh grading, since the desired accuracy can be achieved by using a coarser lattice.

# Chapter 6

# Discussion and Conclusion

## 6.1 Need for Electromagnetic Modeling

Computer techniques have deeply changed the way electrical engineers work. Today's relevant electromagnetic problems can not be solved any longer without the aid of a computer. Electromagnetic modeling software plays an important role in diverse areas such as RF engineering, antenna design, semiconductor physics, and bio-electromagnetics. Computer aided design is a rapidly growing area, and new frontiers of application are continuously added. Electromagnetic simulations of microwave circuits, complex MMIC circuit analysis, and simultaneous thermal and electrical design necessarily require the use of numerical electromagnetic modeling software.

It is possible to foresee in the near future CAD tools capable of simulating a complete MMIC using a full-wave, three dimensional electromagnetic technique, taking into account the effects due to the housing, parasitic coupling and radiation. The use of such simulation tools would significantly reduce the length of design cycles, with a decrease in the cost of development of new products. The explosion of wireless technology is creating a demand for a surprisingly large number of new applications. Direct Broadcast Satellite (DBS), collision avoidance radar, Global Positioning System (GPS), Wireless Local Area Network (WLAN) are commercial applications where the cost for the development of new products is very high, and it could be largely reduced by using simulation tools that allow circuit and system designers to check their designs early in the design process.

For all these reasons numerical techniques for electromagnetic modeling appear to be destined to have a rapid growth in popularity among the electrical engineering community.

On the other hand, there are still several critical issues in computational electromagnetics that remain to be solved in order to establish full-wave numerical techniques as reliable and efficient design tools. Among them we can mention:

- The extent of computional effort is demanding. Memory and CPU time requirements are often very restrictive.
- Lack of user-friendly interfaces.
- Users must be knowledgeable in electromagnetics.
- The flexibility and generality of application is sometimes paid with less accuracy. General purpose electromagnetic software is extremely valuable when dealing with complex geometries and media. However, when highly accurate solutions are required, a combination of analytical and numerical methods must be applied to approximate the solution with the desired accuracy.

The ongoing research has already improved some of these drawbacks. Powerful graphics tools nowadays allow one to create customizable graphical user interfaces (GUI) by means of which the structure under investigation can be drawn and modified very efficiently and quickly. Standard formats [91-92] are emerging, thus creating the basis for transparent exchange of data between different CAD tools.

As for the need of user expertise in electromagnetics, studies have been performed, and are still in progress, to extract from the electromagnetic simulations global parameters such as voltage and current distributions, characteristic impedances, propagation constant, and equivalent circuits [93-95].

Moreover, the incredible rate at which new faster microprocessors and larger memories are introduced into the market makes full-wave numerical analysis increasingly more appealing and economical. Simulations that few years ago would have required expensive workstations, can now be run *faster* in a relatively low cost personal desktop computer.

Despite the extensive research performed, the trade-off between accuracy and flexibility remains one of the critical points in the development of full-wave general purpose CAD tools. Generality of application and flexibility require that information regarding the geometry to be simulated (initial and boundary conditions) be entered as late as possible in the algorithm data-flow. Any change in the structure would therefore require only minor changes, without affecting the main solving algorithm. The consequence is that no

*a priori* information is fed into the model, thus relying merely on a brute force solution.

The present thesis focuses on how to enhance the accuracy of the transmission line matrix method while retaining its flexibility.

Error analysis in the TLM method reveals that the coarseness error is the most serious source of inaccuracy. The finite discrete TLM network does not accurately model regions in which field singularities are present. This is the case with structures containing sharp features such as edges and metallic corners. The brute force solution attempted by the TLM algorithm is therefore not accurate. Different methods on how to introduce the *a priori* knowledge of the presence of the field singularities in the basic TLM algorithm has been investigated. In particular, in order to maintain the flexibility typical of space discrete differential methods, only *local* modifications of the algorithm have been considered.

By using a static approximation of singular fields in the vicinity of metallic edges a simple modification of the TLM scattering algorithm has been derived. The reflected and incident voltages at the current and previous time step have been exploited, thus increasing the information contained in the cell. The accuracy of the modified algorithm has improved, without affecting the original flexibility of the TLM technique.

The stability of a complex time domain algorithm is extremely difficult to predict, and any change in the update equations can lead to potential instabilities. Long term instabilities have been observed in the simulation of structures where a strong coupling between physical and non-physical solutions, usually uncoupled in a free space propagation, is present. In order to avoid such a problem, a new technique, based on circuit theory, have been explored. The equivalent circuit of a corner node has been obtained by using the quasi-static approximation of the Green's functions for an infinite conductive wedge. The derived hybrid TLM network guarantees to produce an unconditionally stable scheme. Such a solution presents also the advantage of lending itself to a very easy implementation.

## 6.2 Future Work

The approach based on the derivation of an equivalent circuit for the modeling of singular field regions has appeared to be the more efficient than that based on the static field approximation, due to its robustness and ease of implementation.

It is for this reason that future research should focus on this direction, aiming at the creation of fully 3D models of a large class of small features present in electromagnetic structures. A research effort should be devoted to the creation of a library of equivalent circuit models. New CAD tools should eventually be able to pre-process the structure under investigation, and include the equivalent model whenever a small feature contained in the library is found.

In this way the advantages of general purpose, full wave field solvers, would be combined with the accuracy and power of analytical tools.

# Appendix A

## 7.1 Impedance elements: pointform evaluation

Equation (7.1) reports the Green's function for a knife edge, as depicted in Figure 7.1. The value of the impedance elements $L_{ij}$ is proportional to equation (7.1) evaluated at the value $\phi_i$ and $\phi'_j$, where i and j indicates one of the three ports.

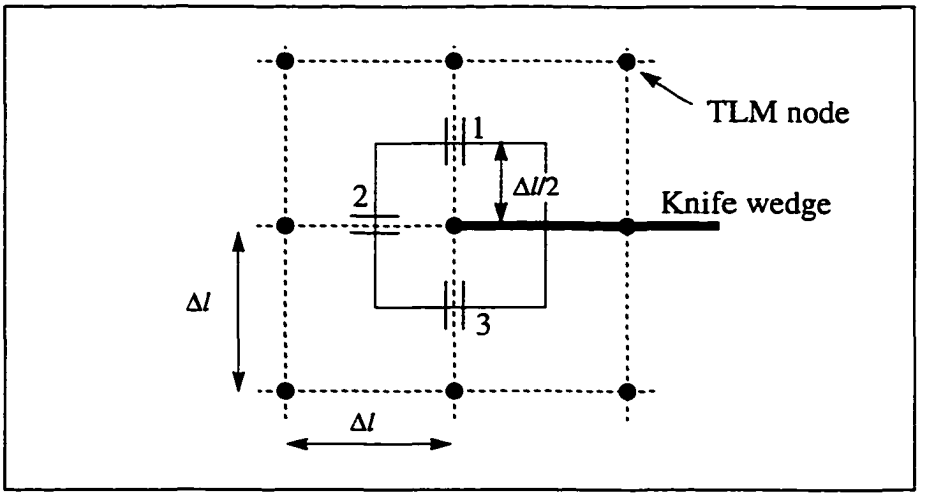


Figure 7.1 Wedge position in the TLM mesh. Knife edge case.

$$\overline{G}(\rho,\phi_i;\rho',\phi'_j) = j\frac{\omega\mu}{\pi}\cdot\pi\Delta l\begin{cases}\sum_{n=1}^{\infty}\frac{1}{n}\left(\frac{\rho}{\rho'}\right)^{\frac{n}{2}}\sin\left(\frac{n}{2}\phi_i\right)\sin\left(\frac{n}{2}\phi'_j\right) \\ \qquad\qquad \rho<\rho' \\ \sum_{n=1}^{\infty}\frac{1}{n}\left(\frac{\rho'}{\rho}\right)^{\frac{n}{2}}\sin\left(\frac{n}{2}\phi_i\right)\sin\left(\frac{n}{2}\phi'_j\right) \\ \qquad\qquad \rho>\rho'\end{cases} = j\frac{\omega\mu}{\pi}\cdot L_{ij} \quad (7.1)$$

## $L_{32} = L_{23}$

$$\frac{L_{23}}{\pi\Delta l} = \sum_{n=1}^{\infty}\frac{1}{n}\sin\frac{n\pi}{2}\sin\frac{3n\pi}{4} = \frac{1}{2}\sum_{n=1}^{\infty}\frac{1}{n}\left(\cos\frac{n\pi}{4}-\cos\frac{5n\pi}{4}\right)$$

$$\frac{L_{23}}{\pi\Delta l} = \frac{1}{2}\sum_{n=1}^{\infty}\frac{1}{n}\left(\cos\frac{n\pi}{4}-\cos\frac{5n\pi}{4}\right) = \frac{1}{2}\left[\log\left(2\sin\frac{5\pi}{8}\right)-\log\left(2\sin\frac{\pi}{8}\right)\right] \quad (7.2)$$

$$L_{23} = \frac{\pi\Delta l}{2}\log\left[\frac{\sin\frac{5\pi}{8}}{\sin\frac{\pi}{8}}\right]$$

## $L_{12} = L_{21}$

$$\frac{L_{12}}{\pi\Delta l} = \sum_{n=1}^{\infty}\frac{1}{n}\sin\frac{n\pi}{2}\sin\frac{n\pi}{4} = \frac{1}{2}\sum_{n=1}^{\infty}\frac{1}{n}\left(\cos\frac{n\pi}{4}-\cos\frac{3n\pi}{4}\right)$$

$$\frac{L_{12}}{\pi\Delta l} = \frac{1}{2}\sum_{n=1}^{\infty}\frac{1}{n}\left(\cos\frac{n\pi}{4}-\cos\frac{3n\pi}{4}\right) = \frac{1}{2}\left[\log\left(2\sin\frac{3\pi}{8}\right)-\log\left(2\sin\frac{\pi}{8}\right)\right] \quad (7.3)$$

$$L_{12} = \frac{\pi\Delta l}{2}\log\left[\frac{\sin\frac{3\pi}{8}}{\sin\frac{\pi}{8}}\right]$$

As expected, $L_{12}=L_{23}$

## $L_{13} = L_{31}$

$$\frac{L_{13}}{\pi\Delta l} = \sum_{n=1}^{\infty} \frac{1}{n} \sin\frac{n\pi}{4} \sin\frac{3n\pi}{4} = \frac{1}{2}\sum_{n=1}^{\infty} \frac{1}{n}\left(\cos\frac{n\pi}{2} - \cos n\pi\right)$$

$$\frac{L_{13}}{\pi\Delta l} = \frac{1}{2}\sum_{n=1}^{\infty} \frac{1}{n}\left(\cos\frac{n\pi}{2} - \cos n\pi\right) = \frac{1}{2}\left[\sum_{n=1,2}^{\infty} \frac{(-1)^n}{2n} - \sum_{n=1,2}^{\infty} \frac{\cos n\pi}{n}\right] \tag{7.4}$$

$$\frac{L_{13}}{\pi\Delta l} = \frac{1}{2}\left[-\frac{1}{2}\sum_{n=1,2}^{\infty} \frac{(-1)^{n+1}}{n} - \sum_{n=1,2}^{\infty} \frac{\cos n\pi}{n}\right] = \left[-\frac{1}{2}\log 2 + \log\left(2\sin\frac{\pi}{2}\right)\right]$$

$$L_{13} = \frac{\pi\Delta l}{4}\log[2]$$

## $L_{11} = L_{33}$

Consider $\rho' \neq \rho$ and $\rho'/\rho = x$.

$$\frac{L_{11}}{\pi\Delta l} = \sum_{n=1}^{\infty} \frac{x^n}{n}\left[\sin\left(\frac{n\pi}{4}\right)\right]^2 = \frac{1}{2}\sum_{n=1}^{\infty} \frac{x^n}{n}\left(1 - \cos\frac{n\pi}{2}\right)$$

$$\frac{L_{11}}{\pi\Delta l} = \frac{1}{2}\sum_{n=1}^{\infty} \frac{x^n}{n}\left(1 - \cos\frac{n\pi}{2}\right) = \frac{1}{2}\left[\sum_{n=1,3,5}^{\infty} \frac{x^n}{n} + \sum_{n=1,3,5}^{\infty} \frac{x^{2n}}{n}\right]$$

$$\frac{L_{11}}{\pi\Delta l} = \frac{1}{2}\left[\sum_{n=1,3,5}^{\infty} \frac{x^n}{n} + \sum_{n=1,3,5}^{\infty} \frac{x^{2n}}{n}\right] = \frac{1}{2}\left[\frac{1}{2}\log\left(\frac{1+x}{1-x}\right) + \frac{1}{2}\log\left(\frac{1+x^2}{1-x^2}\right)\right]$$

$$L_{11} = \frac{\pi\Delta l}{4}\log\left[\frac{1+x^2}{(1-x)^2}\right]$$

# $L_{22}$

$$\frac{L_{22}}{\pi \Delta l} = \sum_{n=1}^{\infty} \frac{x^n}{n}\left[\sin\left(\frac{n\pi}{2}\right)\right]^2 = \frac{1}{2}\sum_{n=1,2}^{\infty} \frac{x^n}{n}(1-\cos n\pi)$$

$$\frac{L_{22}}{\pi \Delta l} = \frac{1}{2}\sum_{n=1,2}^{\infty} \frac{x^n}{n}(1-\cos n\pi) = \sum_{n=1,3,5}^{\infty} \frac{x^n}{n} \tag{7.5}$$

$$\frac{L_{22}}{\pi \Delta l} = \sum_{n=1,3,5}^{\infty} \frac{x^n}{n} = \int\left(\sum_{n=1,3,5}^{\infty} \frac{x^n}{n}\right)dx = \int\left(\sum_{n=0,1,2}^{\infty} \frac{x^{2n}}{n}\right)dx = \int \frac{dx}{1-x^2}$$

$$L_{22} = \frac{\pi \Delta l}{2}\log\left[\frac{1+x}{1-x}\right]$$

# Appendix B

## 8.1 Knife edge case: linear integration

$$L_{ij} = \frac{\pi \Delta l}{W_i W_j} \int_{\phi_i - \pi/4}^{\phi_i + \pi/4} \rho' d\phi' \int_{\phi_j - \pi/4}^{\phi_j + \pi/4} \sum_n \frac{1}{n} \left(\frac{\rho}{\rho'}\right)^{\frac{n}{2}} \sin\left(\frac{n}{2}\phi\right) \sin\left(\frac{n}{2}\phi'\right) \rho d\phi \tag{8.1}$$

where

$$W_i = W_j = \frac{\pi \Delta l}{4} \qquad \rho = \rho' = \frac{\Delta l}{2} \tag{8.2}$$

$$L_{ij} = \frac{4\Delta l}{\pi} \sum_n \frac{1}{n} \int_{\phi_i - \pi/4}^{\phi_i + \pi/4} \sin\left(\frac{n}{2}\phi'\right) d\phi' \int_{\phi_j - \pi/4}^{\phi_j + \pi/4} \sin\left(\frac{n}{2}\phi\right) d\phi \tag{8.3}$$

Using the following integration rule, the final expression for Lij is derived, as reported in (8.5)

$$\int_{\phi - \pi/4}^{\phi + \pi/4} \sin\left(\frac{n}{2}\varphi\right) d\varphi = \frac{4}{n} \sin\left(\frac{n}{2}\varphi\right) \sin\left(\frac{n\pi}{8}\right) \tag{8.4}$$

$$L_{ij} = \frac{64\Delta l}{\pi} \sum_n \frac{1}{n^3} \sin\left(\frac{n}{2}\varphi_i\right) \sin\left(\frac{n}{2}\varphi_j\right) \left[\sin\left(\frac{n\pi}{8}\right)\right]^2 \tag{8.5}$$

## 8.2 Knife edge case: superficial integration

In contrast to the linear integration, the superficial integration must now also take into account the ρ dependance. It is therefore necessary to split the integration with respect to ρ in two sub-integrations, depending on whether $\rho \leq \rho'$, or $\rho' \leq \rho$. The integration in ρ and φ are separable, and the previous calculations for the linear case can be used to carry out the integration for the angular variables. The domain of integration is now a circular sector of angle π/2.

$$W_i = W_j = \left(\frac{\pi \Delta l^2}{16}\right) \tag{8.6}$$

$$L_{ij} = \frac{16^2}{\pi^2 \Delta l^4} (\pi \Delta l)\, 16 \sum_n \left\{ \left[ \frac{1}{n^3} \sin\left(\frac{n}{2}\varphi_i\right) \sin\left(\frac{n}{2}\varphi_j\right) \left[ \sin\left(\frac{n\pi}{8}\right) \right]^2 \right] \int f(\rho, \rho')\, d\rho d\rho' \right\}$$

$$\int f(\rho, \rho')\, d\rho d\rho' = \int_0^{\frac{\Delta l}{2}} \rho d\rho \left[ \int_0^{\rho} \rho' \left(\frac{\rho'}{\rho}\right)^{\frac{n}{2}} d\rho' + \int_{\rho}^{\frac{\Delta l}{2}} \rho' \left(\frac{\rho}{\rho'}\right)^{\frac{n}{2}} d\rho' \right] \tag{8.7}$$

The evaluation of the integral is performed by just applying a sequence of basic calculus rules. The final result is given by:

$$\int f(\rho, \rho')\, d\rho d\rho' = \frac{\Delta l^4}{16\,(4+n)} \tag{8.8}$$

The $L_{ij}$ elements for the case of superficial integration therefore are:

$$L_{ij} = \frac{16^2 \Delta l}{\pi} \sum_{n=1}^{\infty} \frac{1}{n^3 (4+n)} \sin\left(\frac{n}{2}\varphi_i\right) \sin\left(\frac{n}{2}\varphi_j\right) \left[ \sin\left(\frac{n\pi}{8}\right) \right]^2 \tag{8.9}$$

# Appendix C

## 9.1 Ninety-degree wedge: superficial integration

$$G(\rho,\phi;\rho',\phi') = -j\frac{\omega\mu}{\pi}\cdot\begin{cases}\displaystyle\sum_{n=1}^{\infty}\frac{1}{n}\left(\frac{\rho}{\rho'}\right)^{\frac{2n}{3}}\sin\left[\frac{2n}{3}\left(\phi-\frac{\pi}{4}\right)\right]\sin\left[\frac{2n}{3}\left(\phi'-\frac{\pi}{4}\right)\right] & \rho<\rho' \\ \displaystyle\sum_{n=1}^{\infty}\frac{1}{n}\left(\frac{\rho'}{\rho}\right)^{\frac{2n}{3}}\sin\left[\frac{2n}{3}\left(\phi-\frac{\pi}{4}\right)\right]\sin\left[\frac{2n}{3}\left(\phi'-\frac{\pi}{4}\right)\right] & \rho>\rho'\end{cases}$$

$$W_i = W_j = \left(\frac{\pi\Delta l^2}{16}\right) \tag{9.1}$$

$$L_{ij} = -\frac{\pi\Delta l}{W_i W_j}\int_{W_i}\int_{W_j}\left(G(\rho,\phi;\rho',\phi')\right) \tag{9.2}$$

$$L_{ij} = \frac{\pi\Delta l}{W_i W_j}\sum_{n}\left\{\frac{1}{n}\left[\int_{\phi_i-\pi/4}^{\phi_i+\pi/4} g(\phi')\,d\phi'\int_{\phi_j-\pi/4}^{\phi_j+\pi/4} g(\phi)\,d\phi\right]\iint f(\rho,\rho')\,d\rho\,d\rho'\right\}$$

$$g(\varphi) = \sin\left[\frac{2n}{3}(\varphi - \frac{\pi}{4})\right]$$

$$\int_{\phi-\pi/4}^{\phi+\pi/4} g(\varphi)\,d\varphi = \frac{3}{n}\sin(\frac{2n}{3}\varphi)\sin(\frac{n\pi}{6}) \tag{9.3}$$

$$\int f(\rho,\rho')\,d\rho d\rho' = \int_0^{\frac{\Delta l}{2}} \rho d\rho \left[\int_0^{\rho} \rho'(\frac{\rho'}{\rho})^{\frac{2n}{3}} d\rho' + \int_{\rho}^{\frac{\Delta l}{3}} \rho'(\frac{\rho}{\rho'})^{\frac{2n}{3}} d\rho'\right]$$

$$L_{ij} = \frac{16^2 \cdot 9}{\pi^2(\Delta l^4)}\pi\Delta l \sum_n \{\frac{1}{n^3}\sin(\frac{2n}{3}\varphi_i)\sin(\frac{2n}{3}\varphi_j)\left[\sin(\frac{n\pi}{6})\right]^2 \int f(\rho,\rho')\,d\rho d\rho'\} \tag{9.4}$$

The evaluation of the integral is performed by just applying a sequence of basic calculus rules. The final result is given by:

$$\int f(\rho,\rho')\,d\rho d\rho' = \frac{3}{4}\frac{\Delta l^4}{16(3+n)} \tag{9.5}$$

The $L_{ij}$ elements for the case of superficial integration therefore are:

$$L_{ij} = \frac{108\Delta l}{\pi}\sum_{n=1}^{\infty}\frac{1}{n^3(3+n)}\sin(\frac{2n}{3}\varphi_i)\sin(\frac{2n}{3}\varphi_j)\left[\sin(\frac{n\pi}{6})\right]^2 \tag{9.6}$$

# Bibliography


[1] S. Ramo, J. R. Whinnery, T. Van Duzer, *Fields and Waves in Communication Electronics*, 2nd Edition, Chapter 1 - 2, John Wiley & Sons, 1984.

[2] J. Tisal, "*GSM Cellular Radio Telephony*", John Wiley ESME-Sudria, France 1997

[3] Wireless Local Area Network: IEEE standard 802.11. Web Site: "*http:// stdsbbs.ieee.org/groups/802/11/index.html#Topeference*"

[4] R. Sorrentino ed. *Numerical Methods for Passive Microwave and Millimeter Wave Structures*, IEEE Press, 1989.

[5] M. N. O. Sadiku, *Numerical Techniques in Electromagnetics*, CRC Press, 1992.

[6] M. Forest, W. J. R. Hoefer, "A Novel Synthesis Technique for Conducting Scatterers Using TLM Time Reversal", *IEEE Trans. Microwave Theory and Tech*, vol. 43, no. 6, pp. 1371-1378, June. 1995.

[7] L. Cascio, G. Tardioli and W. J. R. Hoefer, "Synthesis Procedure via TLM Time Reverse Process", *Proceeding of the First International Workshop on Transmission Line Modeling (TLM)*, pp. 263-266 Victoria, Canada, 1-3 August 1995.

[8] K. S. Yee, "Numerical Solution of Initial Boundary Value Problems Involving Maxwell's Equations in Isotropic Media", *IEEE Trans. Antennas Propagation*, vol. AP-14, no. 3, pp. 302-307, May 1966.

[9] W. J. R. Hoefer, "The Transmission Line Matrix Method - Theory and Applications", *IEEE Trans. Microwave Theory and Tech.*, vol. 33, Oct. 1985, pp. 882-893

[10] M. Krumpholz, L. P.B. Katehi, "New Prospects for Time Domain Analysis", IEEE Microwave Guided Wave Letters, vol. 5, no. 11, Nov. 1995

[11] M. Krumpholz, H. G. Winfal and L. P.B. Katehi, "MRTD Modeling of Non Liner Pulse Propagation", *IEEE MTT-S International Microwave Symposium Digest*, San Francisco CA, June 1996, pp. 597-600.

[12] E. M. Tentzeris, R. L. Robertson and L. P.B. Katehi, "Space and Time Adaptive Gridding Using MRTD Technique", *IEEE MTT-S International Microwave Symposium Digest*, Denver CO, June 1997, pp. 337-340.

[13] K. L. Shlager, J. B. Schneider, "Analysis of the Dispersion Properties of the Multiresolution Time-Domain (MRTD) Scheme", *IEEE Antennas and Propagation Society International Symp.*, Montreal, July 1997, pp. 2144-2147

[14] F. J. German, "Infinitesimally Adjustable Boundaries in Symmetrical Condensed Node TLM Simulations", *Proceedings of ACES 93, 9th Annual Review of Progress in Applied Electromagnetics*, Monterey, CA, pp. 482-490, 1993.

[15] L. de Menezes, W. J. R. Hoefer, "Accuracy of TLM Solutions of Maxwell's Equations", *IEEE MTTS Symposium Digest*, 1996, pp.1019-1022.

[16] P. Mezzanotte, L. Roselli, C. Huber, H. Zscheile, W. Heinrich, "On the Accuracy of the Finite -Difference Method Using Mesh Grading", *IEEE MTTS Symposium Digest*, Orlando, 1995, pp. 781-784.

[17] D. A. Al-Mukhtar, J. E. Stich, "Transmission Line Matrix Method and Irregularly Graded Space", *Proceedings of IEE* Pt H 128, 299-305.

[18] J. L. Herring, C. Christopolous, "Multi-grid Transmission Line Modeling Method for Solving Electro-magnetic Field Problems", *Electronics Letters*, 1991, vol. 27, no. 20, pp. 1794-1795.

[19] J. Ala-Laurinaho, T. Hirvonen, A. V. Raisanen, " Numerical Modeling of a Nonuniform Grating with FDTD", Microwave and Optical Technology Letters, vol. 15, no. 3, pp. 134-137, June 1997.

[20] S. S. Zivanovic, K. S.Yee, "A Subgridding Method for the Time Domain Finite Difference Method to Solve Maxwell's Equations", *IEEE Trans. Microwave Theory and Tech*, pp. 471-479, 1991.

[21] C. J. Railton, "An Algorithm for the Treatment of Curved Metallic Laminas in the Finite Difference Time Domain Method", *IEEE Trans. Microwave Theory and Tech*, vol. 41, no. 8, pp. 1429-1438, Aug. 1993

[22] T. G. Jurgens et al., "Finite-Difference Time-Domain Modeling of curved Surfaces", *IEEE Trans. Antennas and Propagation*, vol. 40, no. 4, pp. 357-366, April. 1992

[23] I. J. Craddock, C. J. Railton, "Analysis of Curved and Angled Surfaces on a Cartesian Mesh Using a Novel Finite Difference Time Domain Method", *IEEE Trans. Microwave Theory and Tech*, vol. 43, no. 10, pp. 2460-2465, Ott. 1995

[24] J. Anderson, M. Okoniewski, S. S. Stuchly, "Practical 3-D Contour/Staircase Treatment of Metals in FDTD", *IEEE Microwave and Guided Wave Letters*, vol. 6, no. 3, pp. 146-148, March 1996.

[25] D. B. Shorthouse, C. J. Railton, "The Incorporation of Static Field Solutions into the Finite Differerence Time Domain Algorithm", *IEEE Trans. Microwave Theory and Tech*, vol. 40, no. 5, pp. 986-994, May. 1992

[26] C. J. Railton, "Use of static field solutions in the FDTD method", *Electronics Letters*, vol. 29, no. 16, pp. 1466-1468, Aug. 1993.

[27] G. Mur, "The Modeling of Singularities in the Finite-Difference Approximation of the Time-Domain Electromagnetic-Field Equations", *IEEE Trans. Microwave Theory and Tech*, vol. 29, no. 10, pp. 1073-1077, October 1981.

[28] S. Lindenmeier, P. Russer and W. Heinrich, "Hybrid Dynamic-Static Finite-Difference Approach for MMIC Design", *IEEE MTTS Symposium Digest*, San Francisco CA, 1996, pp. 197-200.

[29] K. Beilenhoff, W. Heinrich and H. L. Hartnagel, "Improved Finite-Difference Formulation in Frequency Domain for Three-Dimensional Scattering Problems", *IEEE Trans. Microwave Theory and Tech*, vol. 40, no. 3, pp. 540-545, Mar. 1992.

[30] U. Mueller, P. So, W. J. R. Hoefer, "The Compensation of Coarseness Error in 2D TLM Modeling of Microwave Structures", *IEEE MTTS Symposium Digest*, 1992, pp. 373-376.

[31] L. Herring, W. J. R. Hoefer, "Compensation of Coarseness Error in TLM Modeling of Microwave Structures with the Symmetrical Condensed Node", *IEEE MTTS Symposium Digest*, 1995, Paper TU1B-2, pp. 23-26.

[32] L. de Menezes, W. J. R. Hoefer, "Modeling Gyromagnetic Media in Symmetrical Condensed Node TLM", *12th Annual Review of Progress in Applied Computational Electromagnetics Digest*, vol. 1, pp. 294-301, Monterey Ca, March 1996.

[33] Z. Chen, "Modelling Absorbing Boundary Conditions with TLM", *Proceeding of the First International Workshop on Transmission Line Modeling (TLM)*, Victoria, Canada, 1-3 August 1995, pp. 63-72.

[34] C. Eswarappa, W. J. R. Hoefer, "Performance Study of One-Way Absorbing Boundary Equations in 3-D TLM for Dispersive Guiding Structures", *IEEE MTT-S International Microwave Symposium Digest*, Atlanta, June 1993, pp. 1439-1442.

[35] C. Eswarappa, G. I. Costache, W. J. R. Hoefer, "TLM Modeling of Dispersive Wideband Absorbing Boundaries with Time Domain Diakoptics for S-Parameter Extraction", *IEEE Trans. Microwave Theory and Tech*, vol. 38, no. 4, pp. 379-386, Apr. 1990.

[36] M. Righi, W. J. R. Hoefer, "Efficient 3D-SCN-TLM Diakoptics for Waveguide Components", *IEEE Trans. Microwave Theory and Tech*, vol. 42, no. 12, pp. 2381-2386, Dec. 1994.

[37] F. Moglie, T. Rozzi, P. Marcozzi, A. Schiavoni, "A New Termination for the Application of FDTD Techniques to Discontinuity Problems in Close Homogeneous Waveguide", *IEEE Microwave and Guided Wave Letters*, vol. 2, no. 12, pp. 475-477, December 1992.

[38] C. Eswarappa, W. J. R. Hoefer, "One-Way Equation Absorbing Boundary Condition for 3-D TLM Analysis of Planar and Quasi-Planar Structures", *IEEE Trans. Microwave Theory and Tech*, vol. 42, no. 9, pp. 1669-1674, Sept. 1994.

[39] J. P. Berenger, "A Perfectly Matched Layer for the Absorption of Electromagnetic Waves", Journal of Computational Physics, vol. 114, no. 2, pp. 185-189, Oct. 1994.

[40] N. Pena, M. M. Ney, "Absorbing-Boundary Conditions Using Perfectly Matched-Layer (PML) Technique for Three-Dimensional TLM Simulations", *IEEE Trans. Microwave Theory and Tech*, vol. 45, no. 10, pp. 1749-1756, Oct. 1997.

[41] W. J. R. Hoefer: 'The Transmission Line Matrix (TLM) Method', in *Numerical Techniques for Microwave and Millimeter Wave Passive Structures*, T. Itoh, Ed. John Wiley, New York 1989, pp. 496-591.

[42] C. Christopoulos, *The Transmission-Line Modeling Method*, IEEE Press Oxford University Press, 1995.

[43] P. B. Johns, R. L. Beurle: 'Numerical Solution of 2-Dimensional Scattering Problems using a Transmission-Line Matrix', *Proc. IEE*, vol. 118, no. 9, pp. 1203-1208, Sep. 1971.

[44] S. Akhtarzad, P. B. Johns, "Solution of 6-Component Electromagnetic Fields in Three Space Dimensions and Time by the TLM Method", *Electron. Lett.*, vol. 10, pp. 535-537, Dec. 1974.

[45] P. B. Johns: 'A Symmetrical Condensed Node for the TLM Method', *IEEE Trans. Microwave Theory and Tech*, vol. 35, no.4, pp. 370-377, Apr. 1987.

[46] W. J. R. Hoefer, "Huygens and the Computer- A Powerful Alliance in Numerical Electromagnetics", *Proceedings of the IEEE*, Vol. 79, no. 10, pp. 1459-1471, Oct. 1991

[47] *Proceeding of the First International Workshop on Transmission Line Modeling (TLM)*, Victoria, Canada, 1-3 August 1995.

[48] W. J. R. Hoefer, P. P. M. So, *The Electromagnetic Wave Field Simulator*, John Wiley & Sons, 1991.

[49] P. P. M. So, C. Eswarappa, W. J. R. Hoefer, "A Two-Dimensional TLM Microwave Field Simulator Using New Concepts and Procedures", *IEEE Trans. Microwave Theory and Tech.*, vol. 37, no. 12, pp. 1877-1884, Dec. 1989.

[50] Z. Chen, W. J. R. Hoefer, M. Ney, "A new Procedure for Interfacing the Transmission Line Matrix Method with Frequency Domain Solutions", *IEEE Trans. Microwave Theory and Tech.*, vol. 38, pp.1788-1792, Oct. 91.

[51] Akhtarzad, S. and P.B. Johns, "Solution of Maxwell's equations in Three Space Dimensions and Time by the TLM Method of Numerical Analysis". *Proceedings of IEE* 122, 1344-1348, 1975.

[52] Saguet, P., and E. Pic. "Utilisation d'un Nouveau Type de Noeud dans la Methode TLM en 3 Dimensions". *Electronics Letters* 18, pp. 478-480, 1982.

[53] M. Krumpholz, P. Russer, "A Field Theoretical Derivation of TLM", *IEEE Trans. Microwave Theory and Tech*, vol. 42, no.9, pp. 1660-1668, Sept. 1994.

[54] H. Jin, R. Vahldieck "Direct Derivation of the TLM Symmetrical Condensed Node and Hybrid Symmetrical Condensed Node from Maxwell's Equations Using Centered Differences and Averaging", *IEEE Trans. Microwave Theory and Tech*, vol. 42, no.12, pp. 2554-2561, Dec. 1994.

[55] R. A. Scaramuzza and A. J. Lowery, "Hybrid Symmetrical Condensed Node for TLM method", *Electronics Letters*, vol. 26, no. 23, pp. 370-377, 1990

[56] V. Trenkic, C. Christopoulos, and T. M. Benson, "New Symmetrical Super-condensed Node for the TLM Method", *Electronics Letters*, vol. 30, no. 4, pp. 329-330, 1994

[57] V. Trenkic, C. Christopoulos, and T. M. Benson, "Generally Graded TLM Mesh Using the Symmetrical Super-condensed Node", *Electronics Letters*, vol. 30, no. 10, pp. 795-797, 1994

[58] V. Trenkic, C. Christopoulos, and T. M. Benson, "Theory of the Symmetrical Super-Condensed Node for the TLM Method", *IEEE Trans. Microwave Theory and Tech*, vol. 43, no. 6, pp. 1342-1348, June. 1995.

[59] V. Trenkic, C. Christopoulos, and T. M. Benson, "General Symmetrical Condensed Node for the TLM Method", *IEEE Trans. Microwave Theory and Tech*, vol. 44, no. 12, pp. 1342-1348, Dec. 1996.

[60] V. Trenkic, C. Christopoulos, and T. M. Benson, "Dispersion Analysis of a TLM Mesh Using a New Scattering Matrix Formulation", *IEEE Microwave Guided Wave Letters*, vol. 5, no. 3, pp. 79-80, Mar. 1995.

[61] L. de Menezes, "Modeling of Genereal Medium Constitutive Relationships in the Transmission Line Matrix method (TLM)", Ph.D. thesis, University of Victoria, 1996.

[62] T. Itoh ed., *Numerical Techniques for Microwave and Millimeter-Wave Passive Structures*, New York, John Wiley & Sons, 1989.

[63] C. Eswarappa, W. J. R. Hoefer, "Autoregressive (AR) and Autoregressive Moving Average (ARMA) Spectral Estimation Techniques for Faster TLM Analysis of Microwave Structures", *IEEE Trans. Microwave Theory and Tech*, vol. 42, no. 12, pp. 2407-2414, Dec. 1994.

[64] J. S. Nielsen, "Spurious Modes of the TLM Condensed Node Formulation," IEEE Microwave and Guided Wave Letters, vol. 1, no. 8, Aug. 1991.

[65] M. Krumpholz, P. Russer, "On the Dispersion on TLM and FDTD", *IEEE Trans. Microwave Theory and Tech*, vol. 42, no.7, pp. 1275-1279, July. 1994.

[66] S. Lindenmeier, B. Isele, R. Weigel and P. Russer, "A Fast Spatial Domain Method for the Suppression of Excitation-Induced Spurious Modes in SCN-TLM", *IEEE MTT-S International Microwave Symposium Digest*, San Francisco CA, June 1996, pp. 351-354.

[67] J. L. Herring, "Developments in the Transmission-Line Modelling Method for Electromagnetic Compatibility Studies", Ph.D. thesis, University of Nottingham, 1993.

[68] Y. C. Shih, W. J. R. Hoefer, "Dominant and Second-Order Mode Cut Off Frequencies in Fin Lines Calculated with a Two-Dimensional TLM Program", *IEEE Trans. Microwave Theory and Tech*, vol. 28, no.12, pp. 1443-1448, Dec. 1980.

[69] R. C. Booton Jr., *Computational Methods for Electromagnetics and Microwaves*, John Wiley ed., New York 1992.

[70] H. Jin, R. Vahldieck, J. Huang, "Direct Derivation of the TLM Symmetrical Condensed Node from Maxwell's Equations Using Centered Differences and Averaging", *IEEE MTT-S International Microwave Symposium Digest*, San Diego, May 1994, pp. 23-26.

[71] N. Pena, M. Ney, "A General and Complete Two-Dimensional Hybrid Node Formulation Based on Maxwell's Integral Equations", *Proceedings of ACES 96*, 12th Annual Review of Progress in Applied Electromagnetics, Monterey, CA, pp. 254-261, March 1996.

[72] N. Pena, M. Ney, "A General Formulation of a Three-Dimensional Condensed Node with the Modeling of Electric and Magnetic Losses and Current Sources", *Proceedings of ACES 96*, 12th Annual Review of Progress in Applied Electromagnetics, Monterey, CA, pp. 262-267, March 1996.

[73] L. de Menezes, W. J. R. Hoefer, "Accuracy of TLM Solutions of Maxwell's Equations", *IEEE Trans. Microwave Theory and Tech*, vol. 44, no.12, pp. 2512-2517, Dec. 1996.

[74] L. de Menezes, W. J. R. Hoefer, "Accuracy of TLM Solutions of Maxwell's Equations", *IEEE MTTS Symposium Digest*, San Francisco, pp. 1019-1022, June 1996.

[75] P. Thoma, T. Weiland, "A Consistent Subgridding Scheme for the Finite Difference Time Domain Method", *International Journal of Numerical Modelling*, vol. 9, 359-374, 1996.

[76] J. Meixner, "The Behavior of Electromagnetic Fields at Edges", *IEEE Transactions on Antennas and Propagations*, vol. 20, no. 4, pp 442-446, July 1972.

[77] J. Van Bladel, *Singular Electromagnetic Fields and Sources*, IEEE Press, 1995.

[78] D. S. Jones, *The Theory of Electromagnetics*, Oxford, England, Pergamon, 1964

[79] A. E. Ruehli, U. Miekkala, and H. Heeb, "Stability of Discretised Partial Element Equivalent EFIE Circuit Models", *IEEE Trans. Antennas and Propagation*, vol. 43, pp. 553-559, June 1995.

[80] I. J. Craddock, C. J. Railton and J. P. McGeehan, "Derivation and Application of an Equivalent Passive Circuit for the FDTD Algorithm", *Microwave and Guided Wave Letters*, vol. 6, pp. 40-43, Jan. 1996.

[81] I. J. Craddock, C. J. Railton, "Application of a Circuit-Based Approach to ensuring the stability of modified Finite Difference Time-domain Algorithms", *12th International Zurich Symposium and Technical Exhibition on Electromagnetic Compatibility*, pp. 515-518, Feb. 1997.

[82] R. F. Harrington, *Time-Harmonic Electromagnetic Fields*, New York: McGraw Hill, 1961.

[83] C. A. Balanis, *Advanced Engineering Electromagnetics*, John Wiley & Sons, 1989.

[84] R. E. Collin, *Field Theory of Guided Waves*, 2nd ed., New York: IEEE Press, 1991.

[85] K. C. Gupta, M. D. Abouzahra, *Analysis and Design of Planar Microwave Components*, New York: IEEE Press, 1984.

[86] T. Okoshi, *Planar Circuits for Microwaves and Lightwaves*, New York: Springer-Verlag, 1985.

[87] G. C. Themes, J. W. LaPatra, *Introduction to Circuit Synthesis and Design*, McGraw Hill ed., 1972.

[88] A. V. Oppenheim, R. W. Schafer, *Digital Signal Processing*, Englewood Cliffs: Prentice-Hall, 1975

[89] N. Marcuvitz, *Waveguide Handbook*, Boston Technical Publishers, 1964

[90] W. Heinrich, et al., "Optimum Mesh Grading for Finite-Difference Method", *IEEE Trans. Microwave Theory and Tech*, vol. 44, no.9, pp. 1569-1574, Sept. 1996.

[91] ACIS Geometric Modeling Standard, Web Site: *http://www.spatial.com*

[92] MAFET-MDE Consortium, Web Site: *http://web-ext2.darpa.mil/ETO/MAFET/*

[93] Special Issue of *IEEE Trans. Microwave Theory and Tech. on Interconnects and Packaging*, vol. 42, no. 9, Sep. 94.

[94] R. Mittra, W. D. Becker, P. H. Harms, "A General Purpose Maxwell Solver for the Extraction of Equivalent Circuits of Electronic Package Components for Circuit Simulation", *IEEE Trans. on Circuits and Systems- I: Fundamental Theory and Applications.*, vol. 39, no. 11, pp. 964-973, Nov. 1992.

[95] M. Righi, W. J. R. Hoefer, B. Bader, R. Doerner, P. Russer, "Lumped Element Equivalent Circuit Parameters Extraction of Coplanar MMIC Components via TLM Simulation" *Proceedings of the 1995 MIOP Conference*, Sindelfingen, Germany, pp. 253-257.